
# External Hot Surface Axisymmetric Models for Supersonic Combustion

A Thesis submitted by

Mengmeng Zhao, M Eng

For the award of

**Doctor of Philosophy**

2016

# Abstract

An external axisymmetric configuration is introduced for supersonic combustion research in hypersonic wind tunnel flow. In this configuration, high quality data can be generated for validation of computational simulations. The external axisymmetric geometry offers the important advantages of easy optical diagnostic access to the physical fields of interest and a geometry that can be visualised as two dimensional, but is free of non two dimensional edge effects. The application of quantitative OH* measurements in the axisymmetric configuration is introduced in this work. A resistively-heated graphite model with a water cooling system was devised for the axisymmetric arrangement and was commissioned to simulate the hot surface environments typically encountered in hypersonic flight. The model was fueled with pure hydrogen and premixed hydrogen-air mixtures through the fuel delivery system that was constructed for the experimental work. Hot wall temperatures within the range of 1500 to 1800 K were achieved during the combustion testing.

Several optical techniques were used for the experimental measurements: Two Colour Ratio Pyrometry (TCRP) and Visible near Infrared (VnIR) Spectrometer methods were used for the hot surface temperature measurement; high-speed schlieren was used for the flowfield visualization and an ICCD camera fitted with a narrow-band filter at approximately 310 nm was used for two-dimensional imaging of the OH* chemiluminescence. The TCRP with the wavelength ratio of I(850nm)/I(700nm) was used for time-resolved temperature determination of the hot surface. The ICCD camera setup was used to detect and quantify the OH* chemiluminescence. The quantitative chemiluminescence measurements were achieved by using the Abel inversion and a new method which is proposed for the first time in this thesis for the calibration of absolute

number density of the radiating OH*. This is a convenient approach when adequate signal magnitudes are emitted from the hot surface radiation and OH* chemiluminescence is acquired through the ICCD device simultaneously during testing.

A set of experimental conditions at Mach 2, Mach 4 and Mach 6 flow were examined over a range of total pressure varying from 0.2 MPa to 1.9 MPa and a total temperature of approximately 570 K. No evidence of combustion was observed from the ICCD images during the hot surfaces testing at the supersonic and hypersonic conditions. The flow environments produced by the TUSQ facility and the models were evidently not sufficient for ignition. The optical diagnostic techniques developed in this study for external axisymmetric configurations were demonstrated based on combustion results acquired in the nominally quiescent test section environment (without hypersonic flow). These tests indicated that the ignition process was initiated when the background pressure was elevated to about 10 kPa. The combustion flow was reconstructed numerically using a CFD Solver - Eilmer3 with a hydrogen oxidation chemistry model and the addition of a OH* sub-scheme reaction mechanism. The measured peak level of OH* chemiluminescence was over-predicted by the numerical simulation by a factor of about 10. The results of the numerical simulations show that in the supersonic and hypersonic cases, the poor mixing also contributed to suppression of the ignition process.

# Certification of Thesis

This thesis is entirely the work of Mengmeng Zhao except where otherwise acknowledged. The work is original and has not previously been submitted for any other award, except where acknowledged.

Student and supervisors signatures of endorsement are held at USQ.

Mengmeng Zhao

Professor David Buttsworth

Principal Supervisor

Dr Ray Malpress

Associate Supervisor

Dr Rishabh Choudhury

Associate Supervisor

# Acknowledgments

There are so many people without whom it would not have been possible to conclude this project with this thesis.

I would first like to acknowledge my supervisor Prof. David Buttsworth for his support and guidance during my candidature. Thanks for sharing your knowledge, constantly providing new ideas and pointing me in the right direction. I really appreciate your patience and making time in reviewing this thesis.

Thanks to my associate supervisor Dr Ray Malpress for your constant encouragement and offering the advice throughout my Ph.D. study. You generously shared your expertise and make time to fabricate the bits and pieces for the experimental apparatus assembly.

A big thank you to my other associate supervisor Dr Rishabh Choudhury for your assistance during the experimental campaigns. Thank you so much for your help in operating the wind tunnel, planing and setting up the experimental work. The experiment would not have been achieved without your effort.

Thanks to Byrenn Birch for your laser-equipped schlieren imaging system and to all fellow students in P10 for your discussions and entertaining moments. Thanks to Adrian Blokland for the production of the 3D-printed models. Thanks to Richard Young in the HPC unit at USQ for assistance with the computational resources for the CFD work in this project and also the mechanical workshop at USQ, especially Oliver Kinder, for assistance during the experimental process. Many thanks go out to Peter Jacobs and Rowan Gollan at the University of Queensland for answering any questions regarding

the use of Eilmer3.

Most importantly, I want to thank my wife Xiaona who has been there to support me at anytime. I would not be where I am without your enduring support over the years. To my loving sons Run and Chen, I am looking forward to spending much more time with you in the future.

Mengmeng Zhao

*May 2016*

# Associated Publications

The following publication was produced during the period of candidature:

**Reviewed Conference Papers**

M.M. Zhao, R. Choudhury, R. Malpress and D.R. Buttsworth, "Absolute Concentration Measurements of OH* in an Axisymmetric Hydrogen-air Premixed Flame Adjacent to a Hot Graphite Model", In 20th Australasian Fluid Mechanics Conference, Perth, Australia, December 2016.

# Contents

# List of Figures

# List of Tables

# Notation

## Roman symbols

| | |
|---|---|
| $A$ | area; constant |
| $A_r$ | pre-exponential constant in Arrhenius equation |
| $C$ | discharge coefficient; conversion factor; constant |
| $c_p$ | specific heat at constant pressure |
| $d$ | diameter |
| $D$ | Abel conversion operator |
| $E$ | activation energy in Arrhenius |
| $E_{b,\lambda}$ | monochromatic emissive power of blackbody |
| $F$ | geometric shape factor, optical factor |
| $F(r)$ | radial distributed physical quantity |
| $Gr$ | Grashof number |
| $H$ | micro hardness |
| $h$ | convection heat transfer coefficient |
| $h\nu$ | photon energy |
| $i, j$ | element indices |
| $I(\lambda)$ | monochromatic radiation intensity of blackbody |
| $I_{turb}$ | turbulence intensity |
| $J$ | momentum flux ratio |
| $k$ | thermal conductivity; Gladstone-Dale constant |
| $k_f$ | forward rate of reaction |
| $k_b$ | backward rate of reaction |
| $L$ | length |

| | |
|---|---|
| $M$ | Mach number |
| $n$ | temperature exponent in Arrhenius equation; mole fraction; refractive index |
| $N$ | number density |
| $Nu$ | Nusselt number |
| $Pr$ | Prandtl number |
| $P(y)$ | line-of-sight integral physical quantity |
| $q$ | heat flux |
| $r$ | recovery factor; radial variable |
| $R$ | gas constant; radius |
| $Re$ | Reynolds number |
| $R_c$ | thermal interface resistance |
| $R_s$ | thermal contact resistance |
| $R_r$ | radiation resistance |
| $S(\lambda)$ | monochromatic signal |
| $St$ | Stanton number |
| $t$ | time |
| $T$ | temperature |
| $u$ | velocity |
| $V$ | voltage; volume |
| $x, y, z$ | rectangular coordinate |
| $y$ | distance |
| $y^+$ | dimensionless wall distance |

**Greek symbols**

| | |
|---|---|
| $\gamma$ | specific heat ratio, $c_p/c_v$ |
| $\delta$ | boundary layer thickness |
| $\Delta r$ | data spacing |
| $\Delta t$ | exposure time |
| $\epsilon$ | emissivity |
| $\varepsilon$ | optic efficiency |
| $\eta$ | optic transmission coefficient |
| $\lambda$ | wavelength |

| | |
|---|---|
| $\mu$ | viscosity |
| $\mu_{lam}$ | laminar viscosity |
| $\mu_{turb}$ | turbulent viscosity |
| $\xi$ | pixel efficiency |
| $\sigma$ | surface roughness |
| $\sigma_s$ | Stefan-Boltzmann constant |
| $\tau_i$ | ignition time |
| $\tau_r$ | reaction time |
| $\rho$ | density |
| $\phi$ | equivalence ratio |
| $\Omega$ | solid angle |

**Subscript**

| | |
|---|---|
| $Abel$ | Abel inversion |
| $aw$ | adiabatic wall |
| $b$ | background |
| $e$ | exit |
| $g$ | graphite |
| $s$ | surface |
| $t$ | test section |
| $th$ | theoretical |
| $w$ | wall |
| $_0$ | stagnation |
| $\infty$ | freestream quantity, infinity |

**Superscript**

| | |
|---|---|
| $*$ | at throat, excited state |
| $\cdot$ | per unit time |
| $-$ | average |

# Acronyms & Abbreviations

| | |
|---|---|
| 2D | Two dimensional |
| 3D | Three dimensional |
| ADU | Analogue to Digital Units |
| CFD | Computational Fluid Dynamics |
| HPC | High-performance Computing |
| ICCD | Intensified Charge Coupled Device |
| LIF | Laser Induced Fluorescence |
| MC nozzle | Mass Control nozzle |
| PIV | Particle Image Velocimetry |
| PR | Position Reference |
| RANS | Reynolds-averaged Navier-Stokes |
| REST | Rectangular-to-Elliptical Shape Transition |
| SNR | Signal Noise Ratio |
| TCRP | Two Colour Ratio Pyrometry |
| TDLAS | Tunable Diode Laser Absorption Spectroscopy |
| TUSQ | The University of Southern Queensland Wind Tunnel |
| UDF | User Defined Function |
| USQ | University of Southern Queensland |
| VnIR | Visible near InfraRed |

# Chapter 1

# Introduction

## 1.1 Motivation: Scramjet Design

A scramjet is an air-breathing engine that has the potential to provide sustained propulsion at hypersonic speeds, and this possibility was first explored by Rene Lorin in 1913 (Heiser and Pratt, 1994). The scramjet, or supersonic combustion ramjet, is a variant of the ramjet air-breathing engine. In a scramjet engine, the combustion of the fuel-air mixture takes place at supersonic speeds, in contrast to a ramjet engine, where the combustion occurs at subsonic speeds.

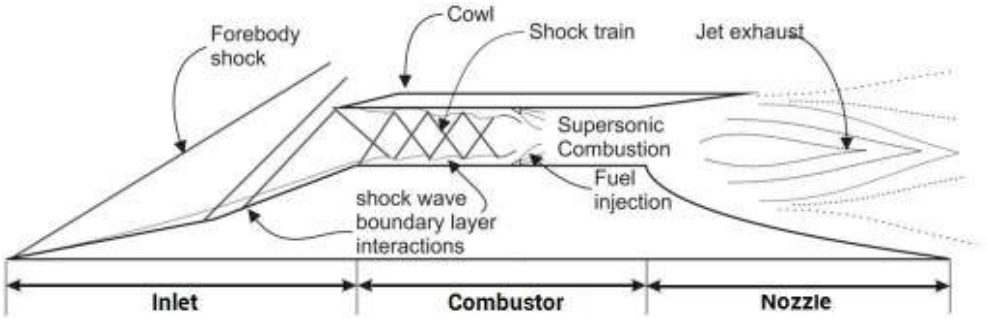


Figure 1.1: Schmatic of a generic scramjet engine

A illustration of the scramjet working principle is shown in Figure 1.1, and the engine consists of three main functional regions: 1. the compression system (or inlet/diffuser); 2. the combustion system (or combustor/burner); and 3. the expansion system (or nozzle/exhaust). In the hypersonic regime, the forward motion of the vehicle compresses

and slows down the oncoming airflow through an intake channel into the combustor. The fuel is injected into the high pressure and temperature flow in the combustor, which leads to a further rise in temperature and pressure due to fuel combustion. The thrust is generated when the heated, high-pressure combustion products expand through the nozzle. This expansion process effectively propels the vehicle forward.

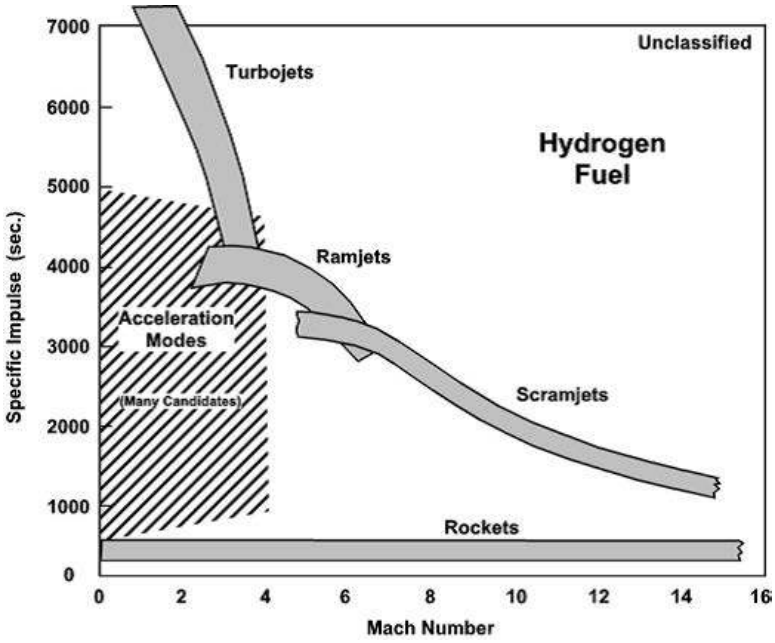


Figure 1.2: Relative efficiency of hydrogen-fueled propulsion systems for Mach 0-15 (Anderson et al., 2000).

A comprehensive investigation of supersonic combustion was conducted at the NASA Lewis Research Center in the late 1950s, although the initial idea of adding heat into a supersonic air stream emerged in the late 1940s (Weber and MacKay, 1958). The superior performance of the hydrogen-fueled scramjet (compared to that of the ramjet engine) was identified for flight speeds exceeding Mach 7. Results from further studies on the efficiency of various propulsion systems using hydrogen fuel for Mach numbers up to 15 are illustrated in Figure 1.2. It is noticeable that scramjet propulsion has higher efficiency in comparison to current rocket technology in the hypersonic regime. Whilst the scramjet engine concept is a promising propulsion model for vehicles accelerating to hypersonic speeds, it is still under development due to its complexity that requires a tightly integrated design strategy employing multi-disciplinary and inter-disciplinary research.

A promising fuel delivery method using porthole injection from locations upstream of the combustion chamber was discussed by Goyne et al. (1999) for the purpose of reducing the overall skin friction drag and heat loading on the scramjet. The intake injection may allow a reduction of the length of the combustion chamber by increasing the fuel mixing distance and thus improve the scramjet overall efficiency, but on the other hand, it introduces the possibility of premature combustion in the intake regions. Investigation into this interesting concept has been undertaken by several researchers with an intake wall temperature at ambient or heated up to 800 K. The results from shock tunnel testing show no evidence of premature combustion on the intake regions (Kovachevich et al., 2004; Kovachevich et al., 2006; Gardner et al., 2002).

The exposed surfaces of a scramjet engine that produces sustained hypersonic propulsion will be very hot due to the aerodynamic heating effect. The high wall temperature of the intake (1500 K or higher) for high Mach number flight can significantly decrease the ignition time and thus increase the possibility of premature combustion, particularly for low flow speed regions such as within a boundary layer where the residence time is increased. Computational simulation of supersonic combustion in scramjets is a popular analysis approach, but extensive validation is required in order to confidently apply such simulations to scramjet design, including intake injection configurations. Therefore, it is important to have reliable experimental data, suitable for validation of computational simulations of supersonic combustion at realistic elevated surface temperatures.

## 1.2 Research Objectives and Scope

The development and demonstration of new methods, techniques and analyses for supersonic combustion research based on an axisymmetric model with a hot graphite surface is the overarching objective of the present work. More specific objectives of this study are identified as follows.

**1. Development of an axisymmetric model with the capability to simulate in-flight elevated wall temperatures and configured with a fuel delivery**

**upstream of the hot surface.**

Several researchers have investigated intake fuel injection based on planar models (Kovachevich et al., 2004; Kovachevich et al., 2006; Gardner et al., 2002; Arai et al., 2003). Because of the edge effects, it is difficult to simulate nominally planar models in hypersonic flow using two dimensional numerical simulations. Typically, three dimensional computational simulations would need to be applied to complement the nominally planar physical model.

An external axisymmetric configuration is adopted for the first time in an effort to generate high quality data from optical diagnostics that will be suitable for validation of future computational simulations of supersonic combustions. The selection of an axisymmetric configuration with annular slot injection for experimental investigation not only eliminates the problems of the edge effects that exists in nominally two dimensional planar models, but also provides convenient access for optical diagnostics applied to boundary/mixing layer and combustion phenomena. Additionally, the intake injection research has been previously limited to low surface temperatures that are not necessarily representative of surface temperatures in hypersonic flight. The capability of the graphite model to simulate surfaces temperature as high as 1800 K allows exploration of ignition and combustion in hypersonic wind tunnels.

**2. Experimental exploration of the ignition/combustion processes using the hot surface model in the TUSQ facility.**

A range of supersonic and hypersonic experiments with different jet flow conditions will be examined using two different configurations for the hot surface model: (1) injection from an annulus in the conical nose of the model, referred to as the 'nose-cone' configuration; and (2) injection adjacent to the graphite in the region of a backward facing step, referred to as the 'step-cone' configuration. Static pressure measurements, surface temperature monitoring and the flow field visualization was achieved using instruments which were available in the TUSQ facility. However, the hardware and techniques required to explore ignition/combustion processes had not previously existed at USQ. So the fuel delivery system and operating procedures needed to be developed and also the combustion diagnostics for measuring the OH* chemiluminescence needed to be

developed and applied in the axisymmetric configuration. The OH* chemiluminescent emissions have been used as a indicator for supersonic combustion phenomena, but not in the axisymmetric configuration (Laurence et al., 2011; Brieschenk et al., 2012).

Although the current range of achievable stagnation temperatures and pressures in TUSQ is not representative of hypersonic flight conditions, the significance of the type of experimentation in this study is found in the generation of relatively long-duration turbulent conditions in the compressible flow regime, from which high quality mixing and potentially combustion data can be generated. The purpose of data acquired from such experiments is to provide validation data for models used in computational simulations.

**3. CFD simulation of OH* chemiluminescence in the axisymmetric hot graphite configuration using Eilmer3**

The software Eilmer3 will be developed to include a capability to predict the OH* chemiluminescent emission in the hydrogen/air combustion simulations. The simulation of hydrogen/air chemistry mechanism including the OH* kinetics scheme will be applied to computational reconstruction of the combustion experiments for the first time.

## 1.3 Research approach

To achieve the research objectives, the project has been approached both experimentally and numerically.

**Experimental approach**

The TUSQ facility with a combination of different contoured nozzles (Mach 2, Mach 4 and Mach 6) offers an opportunity to simulate high speed flow for hypersonic aerodynamic research. However, the cold hypersonic flow produced by TUSQ poses a challenge for studying the premature combustion phenomena adjacent to hot surfaces. Hot surfaces can theoretically be designed for operation in short-duration wind tunnels based on the resistive heating technique (Zander et al., 2012). However, the low stagnation

temperature of the TUSQ flows means that temperatures sufficient to sustain combustion are only generated in the near-wall boundary layer regions. Therefore, the TUSQ results cannot directly simulate in-flight hypersonic combustion conditions. But by using a hot model that generates a high temperature environment near the surface which is conducive for heat induced combustion, it is possible to provide benchmarking data acquired through the experimental campaigns in TUSQ facility for CFD validation of supersonic combustion simulations.

The hot wall model can be fueled with both pure hydrogen and premixed hydrogen-air mixtures under a wide range of TUSQ operating conditions and fuel injection conditions to study heat induced combustion adjacent to the hot surface. A 3-D printed cold wall model duplicating the dimensions of hot wall model was used to investigate the static pressure distribution that can significantly affect the ignition delay time. The methods of Two Color Ratio Pyrometry (TCRP) and Visible near Infrared (VnIR) Spectroscopy were used to record the temperature evolution during hot model testing both with, and without the external supersonic flow. The high-speed schlieren imaging technique was applied using a LED light source for cold wall model testing, and with laser diodes with filtering for hot wall model testing.

Combustion was investigated using an ICCD camera with a narrow-band filter centered at 310 nm with 10 nm FWHM for detecting the OH* chemiluminescence. The 2-D imaged line-of-sight-integrated chemiluminescent emissions were transformed to radial distributions through an Abel inversion method. A new method for calibration of the absolute number density of the radiating radical OH* has been proposed based on the intensity ratio of the simultaneously measured OH* chemiluminescence and the radiation emitted from the hot graphite surface.

**Numerical approach**

Computational Fluid Dynamics (CFD) simulations were performed for selected experimental test cases using the CFD code called Eilmer3 developed at The University of Queensland (Jacobs et al., 2014). These simulations complement the experiments by providing additional insights into the flow field including the fuel-air mixing process that are not yet captured experimentally. The simulated results were first compared to

the static pressure data from the cold wall model experiments, and then the chemical reactions were enabled in order to compare and analyse the results from the combustion experiments. The reaction kinetics scheme of hydrogen oxidation along with the OH* sub-scheme for combustion simulations were identified from the literature. The computational results for the OH* radical concentrations can be related to the quantitative measurements of OH* chemiluminescence.

## 1.4 Thesis Overview

The thesis is comprised of six chapters, including this introductory chapter, and two appendices for risk management of the hydrogen experiments and program codes scripted for this thesis.

**Chapter 2** reviews relevant scramjet research. A brief review of hydrogen/air chemistry is provided, including reaction kinetics schemes for hydrogen oxidation along with the OH* sub-scheme. This is followed by a description of chemiluminescence measurements which have received renewed attention in recent years.

**Chapter 3** outlines the TUSQ facility and its operation along with different measurement techniques and hardware used in the experimental investigation of this study, including the fuel delivery system and the physical model development. A detailed description of the fuel supply system is provided along with the operating principles and validation of temperature measurement techniques.

**Chapter 4** describes the experimental results obtained in a set of tests performed in the Mach 2, Mach 4 and Mach 6 flows. Static pressure measurements on cold-wall models provide important an benchmark for the heat induced combustion tests. The Abel inversion is implemented in the post processing of the OH* chemiluminescence experimental data. A method of absolute number density of radiating excited-state radicals is proposed based on the Abel inverted results.

**Chapter 5** gives a description of the numerical approach for computational reconstruction of the heat induced combustion tests. The analysis of the CFD simulation results

as well as a comparison with the experimental data is presented in this chapter.

**Chapter 6** concludes the thesis by summarising the main findings of the present study and makes recommendations for future work.

# Chapter 2

# Literature Review

This chapter provides a review of the current state of research in configurations used for validation of CFD modeling of supersonic combustion and includes an emphasis on the intake fuel injection technique applied in scramjets. A summary describing the hydrogen/air combustion chemical mechanism with the OH* sub-scheme that is used for CFD simulation in this study is also presented. A review of chemiluminescence measurements is also provided.

## 2.1 Supersonic Combustion for Scramjets

### 2.1.1 Scramjet

Scramjets are hypersonic airbreathing engines that utilize the unique technology of supersonic combustion. Research on scramjet engines started in the 1960s with ground testing and later research was approached both experimentally and numerically (Heiser and Pratt, 1994), while the first flight tests of scramjet demonstration engines have only taken place in recent years (Smart et al., 2006; Holland et al., 2001; Roudakov et al., 1998). The unique feature of a scramjet relative to a ramjet is the air flow remains supersonic throughout the entire engine cycle. Scramjet engines use the forward motion of the vehicle at hypersonic speeds to force air ingestion, compressing and decelerating

the air before combustion generates the pressure rise needed for thrust production.

The two main issues that are introduced by subsonic combustion in a ramjet at flight speeds in excess of Mach 5 are: 1. significantly enhanced shock losses in the inlet due to reducing the airflow to subsonic speed and 2. significantly increased static pressure and temperature that increases the heat load to the engine structure and may lead to material/structural issues. Furthermore, the high temperature causes chemical dissociation in the combustor and nozzle expansion stage that limits energy transfer from the chemical energy in the fuel into thermal energy in the combustion products and places a practical upper limit on ramjet operation somewhere between Mach 6 and 8.

The scramjet concept extends airbreathing engine operation beyond the ramjet engine cycle limit up to as high as Mach 15 by using supersonic combustion. Reduced static pressure and temperature can therefore be achieved with supersonic combustion, and this reduces the combustor wall heat load and the heat loss in the combustor and nozzle expansion stages (Heiser and Pratt, 1994). Although the scramjet engine concept provides a good model for hypersonic vehicle propulsion, the high velocity flow inside the scramjet combustion chamber introduces additional skin friction drag and great challenges for air/fuel mixing and the combustion progress within desirable length scales. The very short residence time (milliseconds) of fuel and air within the engine requires fuel to be burnt rapidly or alternatively to extend the length of the combustor (Curran, Heiser and Pratt, 1996). Previous research has shown that combustion chamber skin friction is the main source of scramjet inefficiency (Goyne et al., 1999). A long combustion chamber causes not only excessive frictional drag, but also increases the weight of the scramjet engine and thus the efficiency of the integrated engine cycle decreases.

### 2.1.2 Intake Fuel Injection

One possible approach that may overcome some of these difficulties is to inject the fuel from a location on the intake after the leading-edge shock-wave as shown in Figure 2.1. In this method, the fuel is injected during the compression stage allowing for increased mixing distances prior to the combustor. The task of the scramjet intake is to channel

as much air as possible and compress it to the desired combustion chamber entrance conditions while generating as low a drag and total pressure loss as possible. However, the fuel may be ignited under some conditions before reaching the combustion chamber, and therefore this will cause the engine to operate at a reduced efficiency or even result in a malfunction (Kovachevich et al., 2004). This premature combustion can be induced by aerodynamic heating which becomes significant when a vehicle is in hypersonic flight (Anderson, 2000): the wall temperature can reach values in excess of 2000 K. Typical temperatures at various locations throughout an inlet flow field that is in chemical equilibrium are shown in Figure 2.2. Avoiding premature combustion of the fuel is essential.

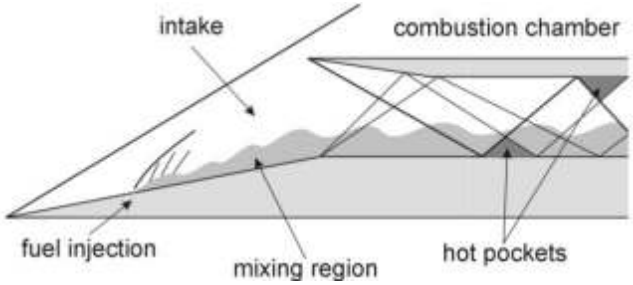


Figure 2.1: Schematic illustration of a scramjet with intake fuel injection (Buttsworth and Jacobs, 2009).

The intake fuel injection method used in supersonic combustion has been extensively studied in the past decades especially by researchers at the University of Queensland, Australia. Studies of shock-induced-combustion with inlet fuel injection show a phenomenon known as 'radical farming' (Odam and Paull, 2007). The radical farming theory was developed to explain the observation that the location of the combustion-induced pressure rise was coincident with the second impingement of the reflected shock that originates from the combustor entrance leading edge.

Paull (1999) conducted an experimental investigation of intake injection and concluded that this method showed promise, possibly allowing for a decrease in the length of the combustion chamber. Later, auto-ignition and combustion of intake-injected fuel without an igniter inside the combustion chamber was demonstrated experimentally using a cold wall model (Gardner et al., 2002). They found no evidence of premature fuel combustion on the intake and deduced that the fuel would not be ignited with

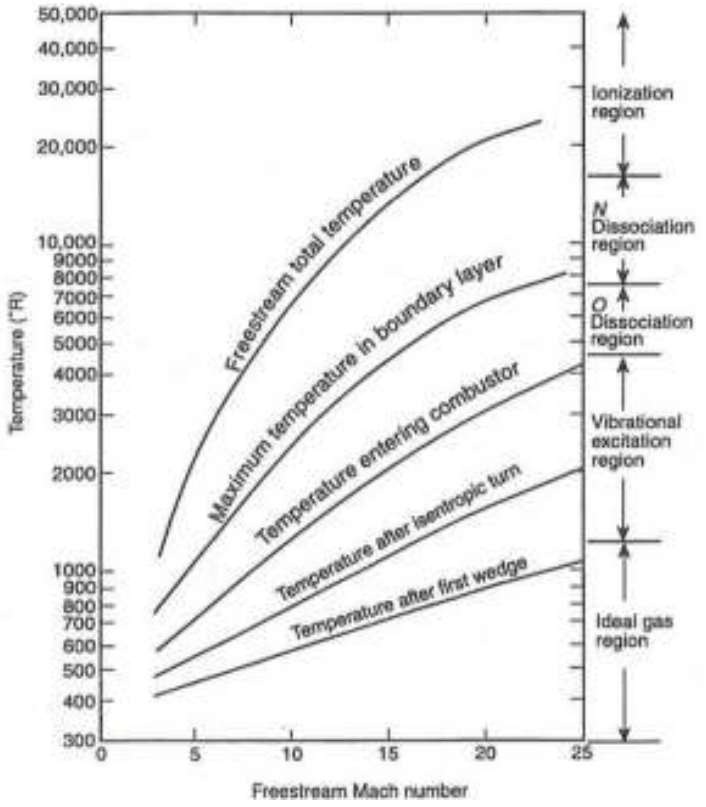


Figure 2.2: Temperatures at various locations in a typical inlet (Van Wie et al., 1990).

a hot wall (800 K) by using CFD comparison of boundary layer conditions for a cold wall condition (300 K) at the locations of injectors and the entrance to the combustion chamber. Experimental study of intake hydrogen injection with the inlet surface at ambient temperature has also been performed by several researchers Arai et al. (2003) and Hunt et al. (2009), with the conclusion that combustion did not occur upstream of the combustor chamber.

A more recent investigation of inlet injection in a scramjet model with a three-dimensional inlet and an elliptical combustion chamber was undertaken by Turner and Smart (2010). Experiments were conducted using a shock tunnel facility representing a Mach 8.1 flight condition at an altitude of 32 km. Results from this cold-wall model indicated that inlet injection produced robust supersonic combustion at good efficiency over a large fuelling range up to an equivalence ratio of 0.92. In addition, no evidence of premature combustion was observed in the inlet region. Separate experiments in which intake hydrogen injection testing with a inlet ramp heated up to 700 K, resulted in no evidence of ignition or combustion occurring on the inlet (Kovachevich et al., 2004; Kovachevich

et al., 2006).

CFD simulations have been performed to investigate hydrogen injection on the intake by several researchers. Comparisons between two-dimensional simulations and surface pressure measurements for cases with and without fuel injection into a free stream flow have been presented (Mudford et al., 2003). Star (2005) modelled a hydrogen-fuelled scramjet with steady-state reactive flow using three-dimensional computational simulations. The results provided some supporting evidence for a radical farming hypothesis, but the predictions for both fuel-off and fuel-on conditions were observed to be sensitive to the choice of the wall temperature boundary conditions. The numerical simulation results of Chan et al. (2010) showed that intake injection could make the scramjet appreciably smaller and lighter, and thus require much less cooling even for a Mach 11 flight condition. A numerical study of a 2D model conducted by Buttsworth and Jacobs (2009) investigated and identified premature ignition regimes which perhaps could be avoided by using an inlet-injection method.

### 2.1.3 Scramjet Model and Injection Geometries

Historically, configurations used for scramjet research in Australia have tended to be rectangular-like cross sections (Gardner et al., 2002; Kovachevich et al., 2006; Odam and Paull, 2002; Neely et al., 2003). More recently, more realistic configurations like the REST inlet and combustor arrangements have been tested (Turner and Smart, 2010). The autoignition and flameholding capability of a cavity flameholder in a REST inlet scramjet model was examined by Denman et al. (2016) in a Mach 7.3 flow. The experimental results show that effects from the combustion of ethylene and hydrogen were observed downstream of the cavity flameholder, but methane did not ignite. With recent improvements in computational power, simulations are able to be performed in 3D configurations (Turner and Smart, 2010; Brindle et al., 2005; Schloegel and Boyce, 2009), but computational resources still impose significant limitations. Axisymmetric scramjet models have also been used for the investigation of thrust production by Bakos and Morgan (1992) and a Busemann-like axisymmetric scramjet with inlet fuel injection has been studied by Hunt et al. (2009), with an emphasis on the application of the radical farming concept to supersonic combustion.

Porthole injection into supersonic flow has been widely investigated and was used as a fuel delivering strategy to facilitate mixing and combustion for scramjet applications (Ben-Yakar and Hanson, 1998; Gruber et al., 1995). The distinct flow structures of a fuel jet injected into a supersonic flow are depicted in Figure 2.3. The most prominent of these features is the bow shock that forms upstream of the fuel jet due to the displacement of the freestream caused by the injected jet. A separation region is introduced from the interaction of the bow shock and the boundary layer. Two recirculation regions are also formed behind the bow shock and downstream of the jet. In these regions the fuel from the jet can mix with the flow and auto ignition is prone to occur due to the increased residence times and high temperatures. Large scale structures which are generated at the interface of jet and freestream caused by the velocity differential are a dominant factor in the mixing process.

Previous experiments have shown that the flow structures of slot injection are similar to those of porthole injection at the centreline axis of the jet (Gruber et al., 1995). Slot injection has comparable mixing in far field to that of arrays of transverse porthole jets but relatively poor initial mixing (Schetz, Thomas and Billig, 1990). The features of poor initial mixing of slot injection may be advantageous in suppressing the possible premature combustion within the two recirculation regions formed near the injector where the increased residence time and high temperatures are conducive to auto ignition.

The trajectory of a jet, which critically determines the fuel distribution within the mixing flow, is known to be strongly correlated with the jet-to-free-stream momentum flux ratio (Billig and Schetz, 1966)

$$J = \frac{(\rho u^2)_e}{(\rho u^2)_\infty} = \frac{(\gamma p M^2)_e}{(\gamma p M^2)_\infty} \tag{2.1}$$

where the subscript $e$ refers to the jet flow conditions and $\infty$ corresponds to free-stream flow conditions upstream of the bow shock.

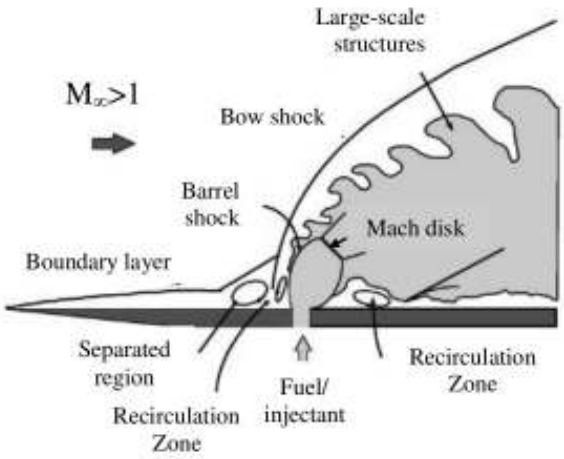


Figure 2.3: Schematic of an under expanded transverse injection into a supersonic cross flow (Gruber et al., 1995).

### 2.1.4 Validation of CFD for Supersonic Combustion

The development of numerical methods and computing facilities has led to the intensive use of Computational fluid dynamics (CFD) as a tool for scramjet research in the design and analysis of airbreathing engine flow paths and supersonic combustion. Although differences still exist between the numerical simulations and reality, it is possible to predict many of the flow properties and thus to avoid some costly experimentation.

In order to increase the computational efficiency, the Reynolds-averaged Navier-Stokes (RANS) equations are typically used for scramjet engineering CFD code applications. For RANS computations, variables such as the Reynolds stress tensor and the turbulent heat and mass flux vectors must be modeled. Validation these models is necessary because they are established empirically; multiple coefficients are typically employed that relate to the statistical quantities of the turbulence. For the numerical simulation of supersonic combustion, chemical kinetics models are also needed and sometimes even more complex models for the interaction between the turbulence and chemistry may be required (Cutler et al., 2004). Quality experimental data on the flow field, well described inflow/boundary conditions and the accurately measured turbulence statistical quantities, are essential in the model development and for CFD validation. Such data can establish the degree of validity for CFD application in scramjet design. Gaffney

et al. (2005) offer guidelines for designing and conducting a CFD validation experiment, and emphasized that communication between CFD developer and the experimentalist and diagnosticians is needed to design the experiments based on the validation goals.

Few experimental arrangements particularly designed for CFD validation of supersonic combustion simulations have been reported. The measurement of mean flow velocity, pressure and temperature in a non-combusting jet into a Mach 2 flow was achieved by Mcdaniel et al. (1991). Temporally and spatially-resolved measurements of velocity in a supersonic hydrogen-air combustor were reported by Goyne et al. (2001). Efforts by researchers at the NASA Langley Research Center have focused on acquisition of data for developing and validating CFD models for turbulence in supersonic combusting flows (Cutler et al., 2004; Cutler et al., 2006; Bivolaru et al., 2006; Drummond et al., 2007; Cutler et al., 2007). These NASA LaRC investigations targeted compressible supersonic mixing and combustion using an axisymmetric coaxial nozzle burner, which provided excellent optical access for nonintrusive diagnostics and a simple flow field, and allowed data to be concentrated in a few spatial locations, increasing measurement precision in the turbulence statistics.

## 2.2 Hydrogen-air Combustion Chemistry Mechanism

### 2.2.1 Hydrogen-air Kinetics

Combustion of hydrogen in air is a complex process which involves a system of elementary reactions that can be classified into three categories of initiation, chain-branching and heat release steps, as shown in Figure 2.4. The hydrogen-air combustion system has been extensively studied over the past decades and the key elemental reactions have been identified (Kuo, 1986).

The initiation reaction provides initial concentrations of H to propagate the chain-branching reactions. A pool of the intermediate radicals (H, O and OH ) is built up by chain-branching reactions. The intermediate radicals can not be accumulated to significant concentrations as they are highly unstable and are quickly consumed. This

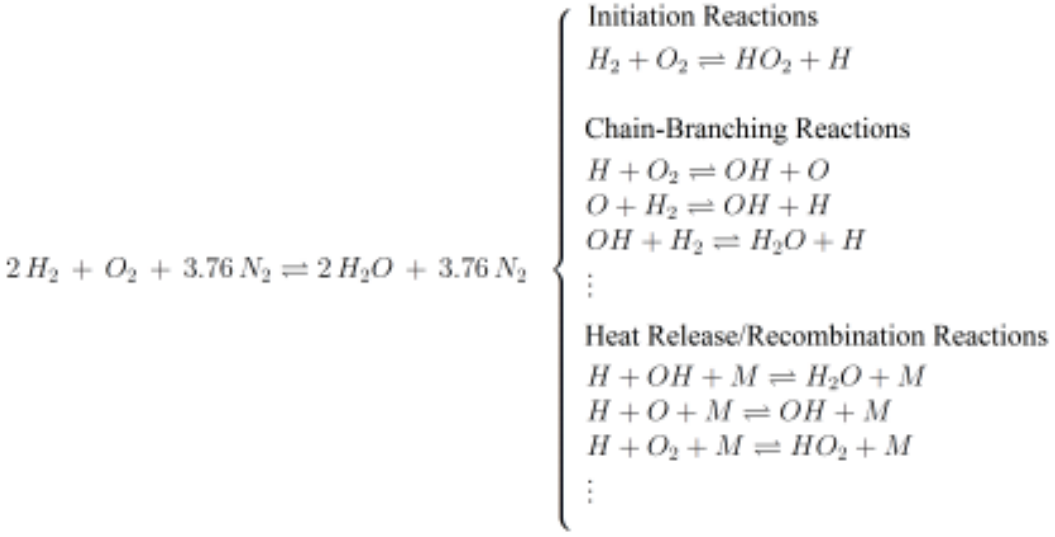


Figure 2.4: Hydrogen-air reaction system (Kuo, 1986).

process is characterized by a slow rise in temperature and pressure due to the weakly exothermic binary reactions involved. Once the radical population reaches a certain threshold, the three-body reaction rates start to dominate the binary reaction rates and consequently the rapid heat release occurs. The end of the ignition delay period is dictated by the concentration of H radicals reaching its maximum values and the rapid heat release is followed by a significant increase in pressure (Rogers, Schexnayder and Charles, 1981). The heat release stage of the combustion process is dominated by pressure-dependent tertiary reactions, which have a less significant dependence on temperature than that of binary reactions that control the ignition process.

Molecular nitrogen $N_2$ is often considered inert for combustion simulations due to the fact it begins to dissociate at very high temperatures, around 4000 K at atmospheric pressure (Anderson, 2000). In particular cases for temperature above 1700 K, the Zeldovich mechanism is responsible for thermal nitric oxide, NO, formation (Billig and Schetz, 1966). Detailed reaction schemes are necessary to accurately model the chemical kinetic processes associated with different combustion regimes. The disadvantages of including many different species and elemental reactions for detailed finite-rate chemistry modeling is that it makes the simulations of reacting flows computationally very expensive. Calculation times for simulations of reacting flows scale with the square of the number of species. Several reaction schemes have been developed to model hydrogen

combustion in air over the past decades (Jachimowski, 1988; Jachimowski, 1992; Evans and Schexnayder, 1980; Maas and Warnatz, 1988; Oldenborg, Chinitz, Friedman, Jaffe, Jachimowski, Rabinowitz and Schott, 1990; Bittker and Scullin, 1972). A chemical kinetic mechanism (Reactions (1)-(18) documented in Table 2.1) developed by Bittker and Scullin (1972) with the consideration of inert $N_2$ was chosen for CFD investigations in the present study. This hydrogen oxidation chemical kinetics scheme offers the flexibility to accurately treat many different reaction conditions in a flowing or static system.

### 2.2.2 OH* Kinetics

In $H_2/O_2$ combustion, the observed self-luminescent emission of UV radiation at a wavelength of around 306 nm is attributed to the OH ($A^2\Sigma^+ X^2\Pi$) transition from its electronically excited state (typically denoted OH* in the flame chemiluminescence literature) to its ground state. The absolute concentrations of these electronically excited species are around five orders of magnitude lower than their ground state counterpart species (Kathrotia et al., 2010; Bozkurt, Fikri and Schulz, 2012). Therefore, OH* is considered to have a negligible influence on the overall hydrogen oxidation reaction progress and these species are usually not included in conventional combustion kinetics models.

The OH* chemiluminescence has long been extensively studied (Carrington, 1959; Kathrotia et al., 2010) and the primary pathways for its formation from energy rich intermediates and its depletion due to collisional quenching and de-excitation are commonly presented as a set of elementary reactions,

$$H + O + M \rightleftharpoons OH^* \qquad (R1)$$

$$OH^* \rightarrow OH + hv \qquad (R2)$$

$$OH^* + M \rightarrow OH + M \qquad (R3)$$

where M is a third body species. There are several other reactions that have been suggested for the formation of OH*

$$H + OH + OH \rightleftharpoons OH^* + H_2O \quad (R4)$$

$$H + O_2 + OH \rightleftharpoons OH^* + O \quad (R5)$$

$$H_2 + HO_2 \rightleftharpoons OH^* + H_2O \quad (R6)$$

The OH* formation reaction rates are the most difficult to determine and remain controversial. Kathrotia et al. (2010) presented a comprehensive literature review on OH* in hydrogen oxidation. Some researchers have observed that OH* is mainly formed by reaction $R1$ where H combines with O involving a third collision partner in a recombination reaction (Smith et al., 2005; Hidaka et al., 1982; Hall and Petersen, 2006; Gutman et al., 1968; Kathrotia et al., 2010). The recommended rate coefficient of reaction $R1$ differs by as much as two orders of magnitude between these studies. These investigations also revealed that the OH* is predominantly formed by reaction $R1$ at temperatures below 2800 K whereas the production of OH* thermally is mainly via the reverse reaction in $R3$ at very high temperatures above 2800 K.

The rate coefficients of the radiative decay reaction $R2$ is given by several researchers (Hidaka et al., 1982; Paul et al., 1995; Smith et al., 2002) and the major collision partner and recommended rate coefficients for $R3$ are reported in Tamura et al. (1998). The OH* sub-mechanism with the Reactions (19) to (26) are added to the base hydrogen-oxidation mechanism in Table 2.1, where the rate coefficients of Reaction (19) and (20) are obtained from Kathrotia et al. (2010) and Smith et al. (2002) respectively, while coefficients for Reactions (21) to (26) are taken from the recommendations of Tamura et al. (1998).

The reaction rate coefficient $k_f$ is given in the form of temperature dependent Arrhenius expression,

$$k_f = A_r T^n exp(-E/RT) \quad (2.2)$$

where $A_r$ is the pre-exponential frequency factor, $n$ is the temperature exponent, $E$ is the activation energy and $R$ is the universal gas constant. The activation energy

can be imagined as an energy threshold required to start a chemical reaction. The reverse reaction rate coefficient $k_b$ can be computed from the assumption of equilibrium condition for a chemically reacting mixture (Turns et al., 1996).

Table 2.1: Reaction kinetics scheme of hydrogen oxidation along with the OH* sub-scheme.

| Reaction # | Reactions | $A$ | $n$ | $E$ |
|---|---|---|---|---|
| H2/O2 kinetics scheme | | | | |
| (1) | $H_2 + OH \rightleftharpoons H_2O + H$ | $2.10\times10^{13}$ | 0 | 21.35 |
| (2) | $H + O_2 \rightleftharpoons OH + O$ | $1.25\times10^{14}$ | 0 | 68.23 |
| (3) | $O + H_2 \rightleftharpoons OH + H$ | $2.95\times10^{13}$ | 1 | 41.02 |
| (4) | $H + O_2 + M(1) \rightleftharpoons HO_2 + M(1)$ | $1.59\times10^{15}$ | 0 | -4.19 |
| (5) | $H + H + M(2) \rightleftharpoons H_2 + M(2)$ | $1.0\times10^{18}$ | -1 | 0 |
| (6) | $H_2 + HO_2 \rightleftharpoons H_2O_2 + H$ | $9.6\times10^{12}$ | 0 | 100.46 |
| (7) | $H_2O_2 + M(3) \rightleftharpoons OH + OH + M(3)$ | $1.17\times10^{17}$ | 0 | 190.45 |
| (8) | $HO_2 + H \rightleftharpoons OH + OH$ | $7.0\times10^{13}$ | 0 | 0 |
| (9) | $H + OH + M(4) \rightleftharpoons H_2O + M(4)$ | $7.5\times10^{23}$ | -2.6 | 0 |
| (10) | $O + O + M \rightleftharpoons O_2 + M$ | $1.38\times10^{18}$ | -1 | 1.42 |
| (11) | $O + H_2O \rightleftharpoons OH + OH$ | $5.75\times10^{13}$ | 0 | 75.34 |
| (12) | $H_2 + O_2 \rightleftharpoons OH + OH$ | $1.0\times10^{13}$ | 41.6 | 179.99 |
| (13) | $HO_2 + OH \rightleftharpoons H_2O + O_2$ | $6.3\times10^{12}$ | 0 | 0 |
| (14) | $HO_2 + O \rightleftharpoons O_2 + OH$ | $6.0\times10^{12}$ | 0 | 0 |
| (15) | $HO_2 + HO_2 \rightleftharpoons H2O_2 + O_2$ | $1.8\times10^{12}$ | 0 | 0 |
| (16) | $OH + H_2O_2 \rightleftharpoons H_2O + HO_2$ | $1.0\times10^{13}$ | 0 | 7.53 |
| (17) | $O + H_2O_2 \rightleftharpoons OH + HO_2$ | $8.0\times10^{13}$ | 0 | 4.19 |
| (18) | $H + H_2O_2 \rightleftharpoons H_2O + OH$ | $3.18\times10^{14}$ | 0 | 37.67 |
| OH* sub-scheme | | | | |
| (19) | $H + O + M(5) \rightleftharpoons OH^* + M(5)$ | $1.5\times10^{13}$ | 0 | 25 |
| (20) | $OH^* \rightarrow OH + hv$ | $1.45\times10^{6}$ | 0 | 0 |
| (21) | $OH^* + O_2 \rightarrow OH + O_2$ | $2.1\times10^{12}$ | 0.5 | -2 |
| (22) | $OH^* + H_2O \rightarrow OH + H_2O$ | $5.93\times10^{12}$ | 0.5 | -3.6 |
| (23) | $OH^* + H_2 \rightarrow OH + H_2$ | $2.95\times10^{12}$ | 0.5 | -1.9 |
| (24) | $OH^* + N_2 \rightarrow OH + N_2$ | $1.08\times10^{11}$ | 0.5 | -5.2 |
| (25) | $OH^* + OH \rightarrow OH + OH$ | $6.01\times10^{12}$ | 0.5 | -3.2 |
| (26) | $OH^* + H \rightarrow OH + H$ | $1.31\times10^{13}$ | 0.5 | -0.7 |

Reaction rate coefficient $k_f = AT^n exp(-E/RT)$ with units of kJ, mol, cm, s and K.

M(1) = 5.0[H2] + 32.5[H2O] + 2.0[O2] + 2.0[N2]

M(2) = 5.0[H2] + 15.0[H2O] + 2.0[O2] + 2.0[N2]

M(3) = 6.6[H2O2] + 2.3[H2] + 6.0[H2O] + 0.78[O2]

M(4) = 4.0[H2]+ 20.0[H2O] + 1.6[O2] + 1.6[N2]

M(5) = [H2] + 6.5[H2O] + 0.4[O2] + 0.4[N2]

### 2.2.3 Ignition and Reaction Times

Provided there is sufficient time for a combustion reaction to occur, it will reach a state of equilibrium. The rate of chemical reactions can become critical for regimes of supersonic combustion because the residence time of the reactants in the combustion chamber is of a similar magnitude as the time required for the reactions to initiate and complete. Having insufficient time to complete the combustion process can lead to a non-equilibrium state in reacting mixture flow and, in consequence, can limit the chemical energy release.

The ignition time is normally defined as a temperature rise of 5% of the total equilibrium temperature rise of the system, and the reaction time is taken to be the delay between the end of ignition and the time required to achieve 95% of the final equilibrium temperature rise. Colket and Spadaccini (2001) proposed a correlation of temperature, pressure and $O_2$ concentration for hydrogen ignition time,

$$\tau_i = 1.6 \times 10^{-14} exp(\frac{19700}{RT})(\frac{n_{o_2} p}{R_{O_2} T})^{-1} \tag{2.3}$$

where $n_{o_2}$ is the mole fraction of $O_2$ in mixture, $R$ and $R_{O_2}$ are the universal and oxygen gas constant. A more commonly used correlation for ignition and reaction delay times was proposed by Pergament (1963) based on the analysis of an 8-reaction, 6-species reaction mechanism, as shown in Eq. 2.4 and 2.5 (in SI units)

$$\tau_i = \frac{8 \times 10^{-9}}{p/1.013 \times 10^5} \, e^{\frac{9600}{T}} \tag{2.4}$$

$$\tau_r = \frac{105 \times 10^{-6}}{(p/1.013 \times 10^5)^{1.7}} \, e^{\frac{-1.12\,T}{1000}} \tag{2.5}$$

which are reported to be valid at conditions

$$\begin{cases} 0.2 \leq p \leq 5\,atm \\ 1000 \leq T \leq 2000\,K \\ 0.4 \leq \phi \leq 2.0 \end{cases}$$

where $\phi$ is the equivalence ratio. Rogers et al. (1981) have demonstrated a good agreement of ignition time from Eq. 2.4 by comparison to the results from a more extensive hydrogen-air reaction scheme involving 60 reactions and 20 species.

Based on the expected range of temperature and pressure for the heat induced combustion test presented in this thesis, the computed ignition and reaction time using Eq. 2.4 and 2.5 are plotted in Figure 2.5. The ignition time is more sensitive to temperature compared to the reaction time, whereas the reaction time is more sensitive to pressure compared to the ignition time.

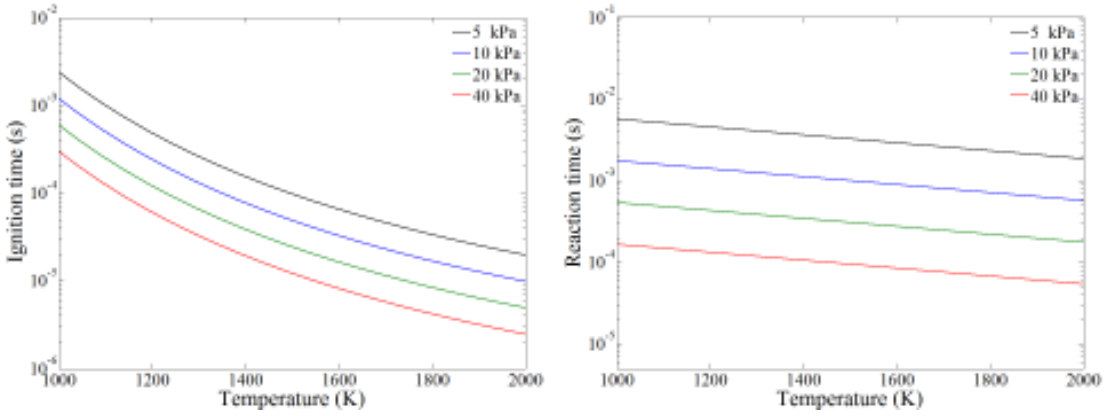


(a) Ignition time

(b) Reaction time

Figure 2.5: Ignition time and reaction time using Eq. 2.4 and 2.5 based on the expected pressure and temperature range during the experimental tests.

## 2.3 OH* Chemiluminescence Measurement

Chemiluminescence measurement does not require complex apparatus as the detected radiation is brought about by inherent chemical reactions within the oxidation system. It provides a convenient diagnostic for flame and combustion phenomena analysis due to its simplicity and non-intrusive nature. The advantage of this method over the commonly used LIF method as a combustion diagnostic technique is avoiding the need for expensive and maintenance-prone laser instruments and apparatus complexity.

Chemiluminescence refers to the spontaneous light emission from chemically excited

species by an electronic exchange process. Chemiluminescence is a frequently used diagnostic in combustion research for detecting the location of flame fronts (Kojima, Ikeda and Nakajima, 2005) and the heat release (Najm et al., 1998; Smith et al., 2005; Hall and Petersen, 2006; Sadanandan et al., 2009). This emission diagnostic is not restricted to point measurements but spatially resolved images can also be transformed into field distributions of absolute flame species concentrations by using an Abel inversion technique, if the flow field is axisymmetric and an absolute calibration of the system sensitivity is performed.

While there have been numerous experimental investigations and applications of chemiluminescence in flames, most previous research involving the radical's chemiluminescence is limited to qualitative or relative measurements. The qualitative measurement of OH* chemiluminescence has been applied to supersonic combustion research (Laurence et al., 2011; Brieschenk et al., 2012). The technique of laser induced fluorescence (LIF) calibrated with a Raman and Rayleigh scattering is normally used for ground state species concentrations measurement (Berg et al., 2000; Luque and Crosley, 1996; Bohm et al., 2005). The absolute concentration of excited species has been achieved using chemiluminescence measurements with a Raman and Rayleigh scattering calibration by several researchers (Smith et al., 2002; Walsh et al., 1998; Nau et al., 2012), and Smith et al. (2002) appears to be the only published measurements of absolute OH* concentrations in hydrogen/air flames. De Leo et al. (2007) measured the radiating OH* and CH* population in the methane and oxygen-enriched air flames by calibrating the integrated spectrum to a known irradiance light source.

## 2.4 Summary

Nominally 2D planar experimental configurations, which are suitable for application of optical diagnostic techniques such as PLIF and ICCD emissions imaging bring the advantage of some simplicity in interpreting results of the experiments. However, rectangular-like ducts with either port-hole or slot injection actually introduce three dimensional or edge effects due to the finite aspect ratios. Therefore computational simulation of these configurations is complicated and normally 3D computational sim-

ulations would need to be applied to complement the research with physical models that are only nominally planar. The obvious benefit from 2D CFD simulations is the significantly reduced computational resource requirements, especially for hypersonic reacting flows which involve many different reactants. In contrast, internal circular cross section scramjet ducts are conducive for computational simulation (2D axisymmetric), but are not suitable for optical diagnostics access into the physical fields of interest.

An external axisymmetric configuration was adopted for the present supersonic combustion research in an effort to generate high quality data from optical diagnostics that is suitable for validation of computational simulations. Hot walls at temperatures approximating realistic values associated with aerodynamic heating at high Mach number have not generally been used so this feature is also introduced into the axisymmetric model configuration. The selection of an axisymmetric configuration with an annular slot injector not only eliminates the problems of the edge effects that exists in 2D planar models but also provides convenient access for optical diagnostics. Most importantly, the geometrical configuration used in the present study enables the use of 2D axisymmetric simulations for computational reconstruction of the combustion experiment. A comparison of the different configurations for supersonic combustion research regarding non-intrusive diagnostic access and the applicable CFD simulation is presented in Table 2.2.

Table 2.2: Features of different geometrical configurations for supersonic combustion study.

| **Configurations** | **Non-intrusive diagnostic** | **CFD** |
|---|---|---|
| Ducted 2D planar model | Suitable | 3D |
| Internal axisymmetric model | Difficult | 2D |
| External axisymmetric model | Suitable | 2D |

# Chapter 3

# Experimental Apparatus

This chapter presents the TUSQ hardware used in the experimental investigation including the hypersonic facility, the fuel delivery system, the hot graphite model and the instrumentation. The flow conditions produced by the Mach 2 and the Mach 4 nozzle were investigated using pitot pressure measurements. The thermal analysis of the hot surface model provides important information on which the operating strategy for the heating relies. The fuel supply system was demonstrated and the injected jet flow conditions have been identified through the combined results from experimental data and CFD simulations. Temperature measurement techniques include Planck curve fitting to the data from a Visible near Infrared (VnIR) spectrometer and a Two Color Ratio pyrometry (TCRP) method with three different wavelength options at 600 700 and 850 nm. The performance of the different temperature measurements was demonstrated by heating test cycle measurements and the TCRP using I(850nm)/I(700nm) was demonstrated as the most accurate for time-resolved temperature measurement of the heated surface.

## 3.1 Wind Tunnel Facility

The free-piston wind tunnel of University of Southern Queensland (TUSQ) was designed and commissioned to perform supersonic and hypersonic experiments. Illustra-

Table 3.1: Principal dimensions of the TUSQ facility.

| Component | Physical Characteristic |
|---|---|
| Air reservoir | 0.350 $m^3$ |
| Primary valve | $\phi$=0.0276 m ($1\frac{1}{4}''$ ball valve) |
| Piston | 0.0383 kg (Nylatron) |
| Barrel | 16.0 m, $\phi$=0.130 m, 0.212 $m^3$ |
| Test section | 0.830 m, $\phi$=0.60 m, 0.235 $m^3$ |
| Dump tanks | 11.321 $m^3$ |

tive configurations and photographs of the TUSQ facility are presented in Figure 3.1. The details of this facility and its variety of operation modes have been reported by Buttsworth (2010).

TUSQ is a short duration hypersonic facility producing useful test flows with a duration of around 200 ms which therefore enables diverse experiments in hypersonic, heat transfers and scramjet inlet tesing to be performed (Buttsworth and Smart, 2010; Kraetzig et al., 2014; Widodo and Buttsworth, 2013; Grainger et al., 2014). TUSQ uses direct compression of the test gas through a free piston as shown in Figure 3.2. The technical specifications of principal components are presented in Table 3.1.

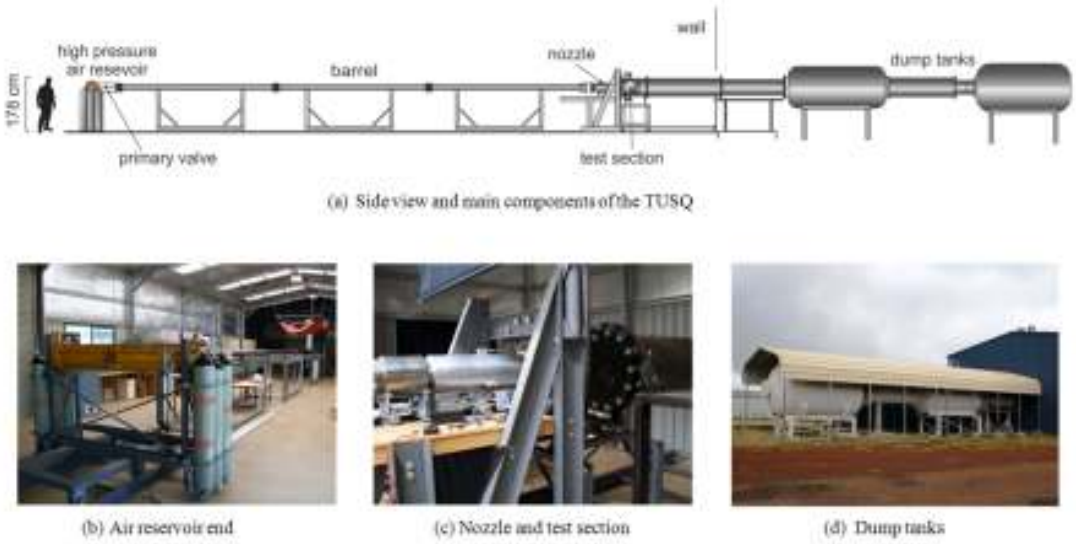


Figure 3.1: Illustration of the TUSQ facility.

Operation of the facility is initiated by opening the primary valve separating the higher

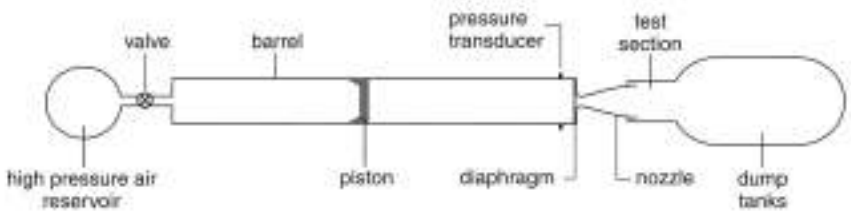


Figure 3.2: Schematic illustration of TUSQ's main components.

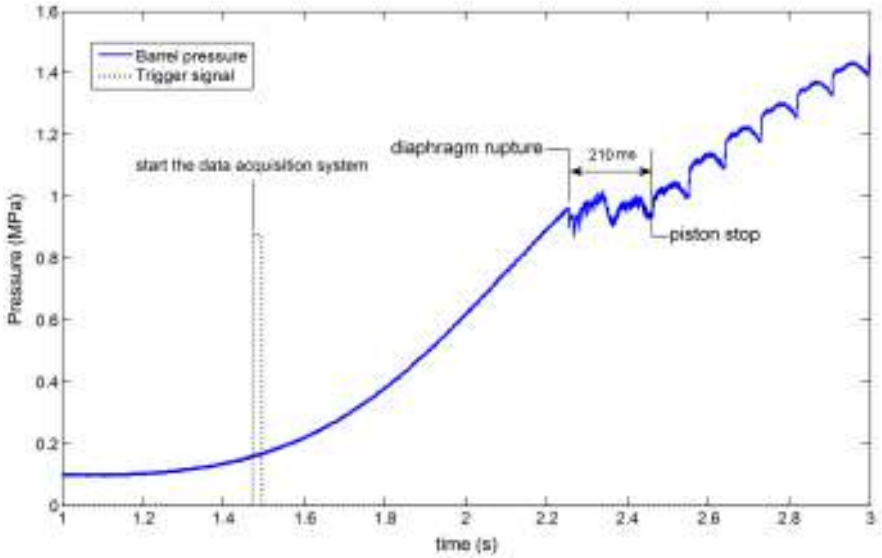


Figure 3.3: An example of the measured barrel pressure history and trigger management for timing the data acquisition system.

pressure driver air from the barrel. The high pressure air drives a piston down the barrel where the test air is retained by a light diaphragm at the entrance to the nozzle. The compression process is approximately isentropic since initially, the air and the barrel are at room temperature and the compression occurs over a period of about 1 second. When the diaphragm ruptures, the test gas accelerates through the nozzle and flows over the model mounted within the test section. The flow rate from the high pressure air reservoir via the primary valve into the barrel is arranged so that it compensates for the discharge of the test air through the nozzle and thus, the nozzle stagnation pressure can be maintained approximately constant.

Prior to a run, the nozzle, test section, and dump volume are evacuated to an absolute pressure below 1 kPa. The test section has optical assess through four port windows and

a test section model support base with tapped holes for model mounting. The pressure in the barrel during the compression process is monitored by a micro-controller which receives a signals from a piezoelectric transducer located at 130 mm upstream of the end of the barrel. An example of barrel pressure history during TUSQ facility operation is displayed in Figure 3.3 which also illustrates the hypersonic flow time that can be inferred from the pressure trace. The start action of measurement instruments and data acquisition system is based on the triggering signal generated by a pulse generator when the barrel pressure exceeds the set values, and this pulse is indicated in Figure 3.3. Thus all recorded data can be synchronized by referring this trigger signal.

The thickness of the mylar diaphragm is chosen according to the desired nozzle reservoir pressure at which the test run is started. The approximate burst pressures of mylar diaphragms of different thickness are presented in Table 3.2. The required reservoir pressure can be obtained by combinations of these different thickness diaphragms in series.

Table 3.2: Mylar diaphragm thickness and corresponding burst pressure.

| **Diaphragm thickness** ($\mu$m) | **Burst pressure** (kPa) |
|---|---|
| 25 | 200 |
| 100 | 860 |
| 175 | 1600 |

## 3.2 High-speed Flow Conditions

Quantification of the flow conditions produced in wind tunnels is important in order to relate wind tunnel results to flight conditions or to perform meaningful computational simulations on the test configuration. Three contoured nozzles: Mach 2, Mach 4 and Mach 6, are employed for this work to produce the high-speed flow. The key geometric features of these nozzles are presented in Table 3.3. A variety of flow conditions can be obtained using these different nozzles operated with different diaphragm thickness.

Table 3.3: Principal dimensions of the nozzles.

| **Component** | **Physical Characteristic** |
|---|---|
| Mach 6 Nozzle<br>2 pieces in aluminum and steel | L = 1.057 m, $d_{throat}$ = 28.8 mm<br>$d_{exit}$ = 217.5 mm |
| Mach 4 Nozzle<br>2 pieces in aluminum | L = 0.403 m, $d_{throat}$ = 28.8 mm<br>$d_{exit}$ = 95.9 mm |
| Mach 2 Nozzle<br>1 piece in steel | L = 0.0945 m, $d_{throat}$ = 30.3 mm<br>$d_{exit}$ = 40.8 mm |

### 3.2.1 Pitot Pressure Survey

The thermal characteristics of the TUSQ compression process and the Mach number profiles of the hypersonic flow generated by the Mach 6 nozzle have been investigated by Widodo (2012). The newly fabricated Mach 4 nozzle and the previously fabricated Mach 2 had not previously been subjected to pitot pressure surveys. Therefore, it was necessary to investigate the flow properties of these two nozzles. For a given Mach number and ratio of specific heats, the pitot pressure scales with flow total pressure under steady conditions, and thus the nozzle pitot pressure was surveyed by using a rake on which four pitot probes with diameter of 2 mm were mounted. The pitot rake was positioned downstream of the Mach 2 and Mach 6 nozzle exits as shown in Figure 3.4. Four Kulite pressure transducers (XTL-190M-3.5BAR) were connected to the probe bodies.

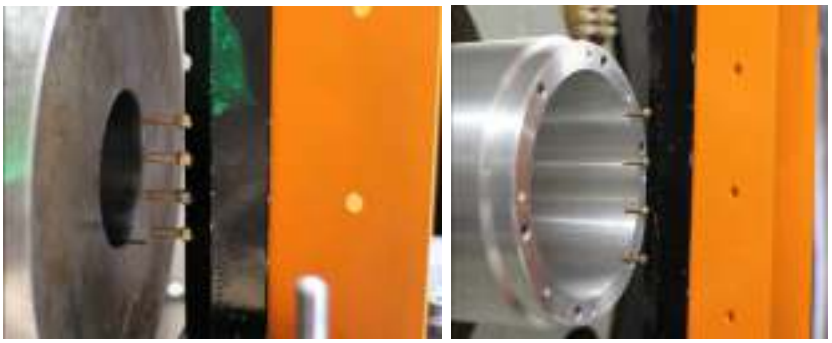

(a) Mach 2 nozzle (b) Mach 4 nozzle

Figure 3.4: Photographs of the pitot pressure survey apparatus.

The probes should be separated laterally far enough to avoid disturbances from each other during the testing. To confirm such a separation has been achieved in the present work, a correlation for sphere-cone bodies that assumes a hyperbolic shock shape was been used. The correlation is give by (Anderson, 2000),

$$x = R + \delta - R_c cot^2\beta \left[ \left( 1 + \frac{y^2 tan^\beta}{R_c^2} \right)^{\frac{1}{2}} - 1 \right] \tag{3.1}$$

where the values of $\delta$ and $R_c$ are correlated from experimental data as

$$\delta = 0.143R \cdot exp\left[3.24/M_\infty^2\right] \tag{3.2}$$

$$R_c = 1.143R \cdot exp\left[0.54/(M_\infty - 1)^{1.2}\right] \tag{3.3}$$

The nomenclature in Eq. 3.1 is illustrated in Figure 3.5, and the calculated shock-wave shapes of a sphere-cone (actually a sphere-cylinder) with a diameter of 2 mm is shown in Figure 3.6. The separation distance between the nearest probes installed on the rake were 10 mm and 20 mm for the Mach 2 and Mach 4 nozzle testing respectively.

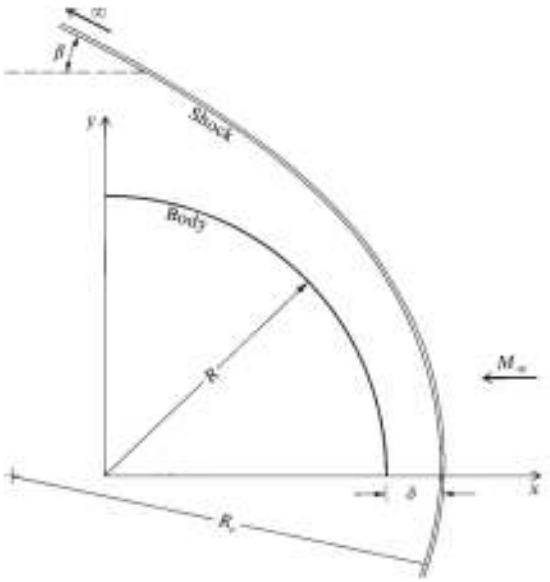


Figure 3.5: Nomenclature for shock-wave shape correlations (Anderson, 2000).

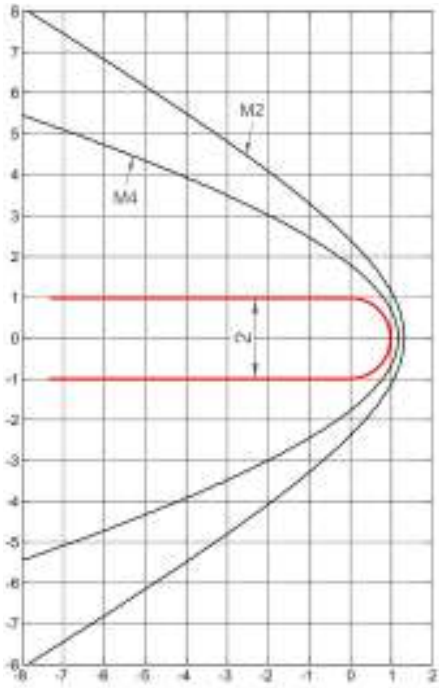


Figure 3.6: Shock-wave shapes of a sphere-cone at Mach 2 and Mach 4 flow (scale: mm).

The position of pitot probes relative to the nozzle exit are illustrated in Figure 3.7, in which frames extracted from the schlieren imaging acquired during flow are presented. The estimated core flow regions are also depicted graphically in these images. The time-resolved pitot pressure measurements from the Mach 2 and Mach 4 experiments as well as the pitot pressure normalized with barrel pressure are presented in Figure 3.8 and 3.9 respectively. Note different diaphragm thickness of 25 $\mu$m and 100 $\mu$m were selected for the Mach 2 and Mach 4 nozzle tests, respectively.

During the nominally steady test flow period, fluctuations in the barrel pressure and thus the pitot pressure measurements arise due to the unsteady waves associated with the diaphragm-opening and piston oscillations. Therefore, it is appropriate to normalize the pitot pressure measurements using the barrel pressure in order to deduce the Mach number, see Figure 3.8b and Figure 3.9b.

In the case of the Mach 2 nozzle testing, the sketch of core flow region in Figure 3.7a indicates that probe P4 was outside of the core flow; probes P2 and P3 were sitting in the core flow while probe P1 was at the edge of core flow boundary. The low values of normalized pitot pressure of P4 is a consequence of being located within the Prandtl-

meyer expansion zone centered near the nozzle lip. Due to the uncertainty of whether P1 is actually within, or outside of the core flow region, only pitot pressures from P2 and P3 were used for Mach number deduction. The averaged value of 0.695 from the normalized pitot pressure results during the testing indicates a Mach number 2.05 flow was generated by the Mach 2 nozzle with an approximate uncertainty of ±0.05.

For the Mach 4 nozzle, the pitot pressure measurement from P1 was excluded from the Mach number deduction because it was located near the edge of core flow region, as illustrated in Figure 3.7b. The averaged value of 0.146 from normalized pitot pressure results during testing indicates a Mach number of 3.94 was produced by the Mach 4 nozzle with an approximate uncertainty of ±0.02.

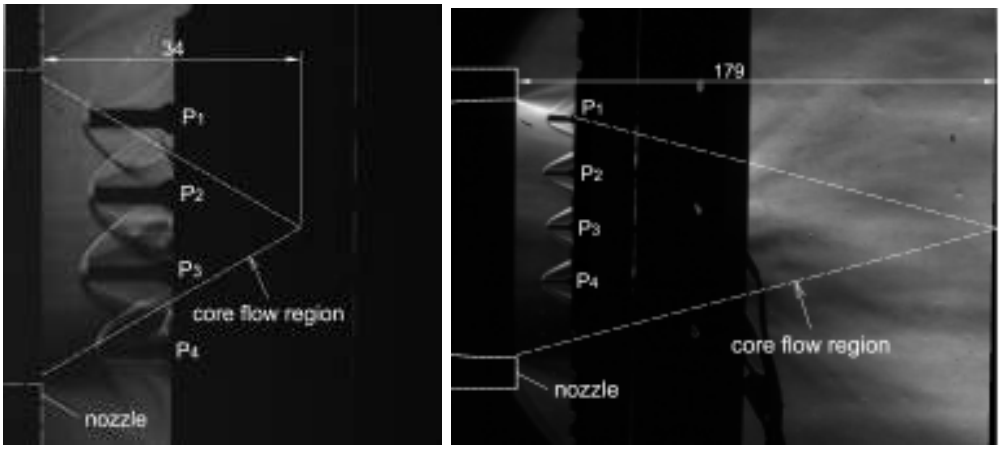


(a) Mach 2 nozzle (b) Mach 4 nozzle

Figure 3.7: Schlieren images from pitot pressure surveying tests. P1 to P4 correspond to the four pitot pressure probes.

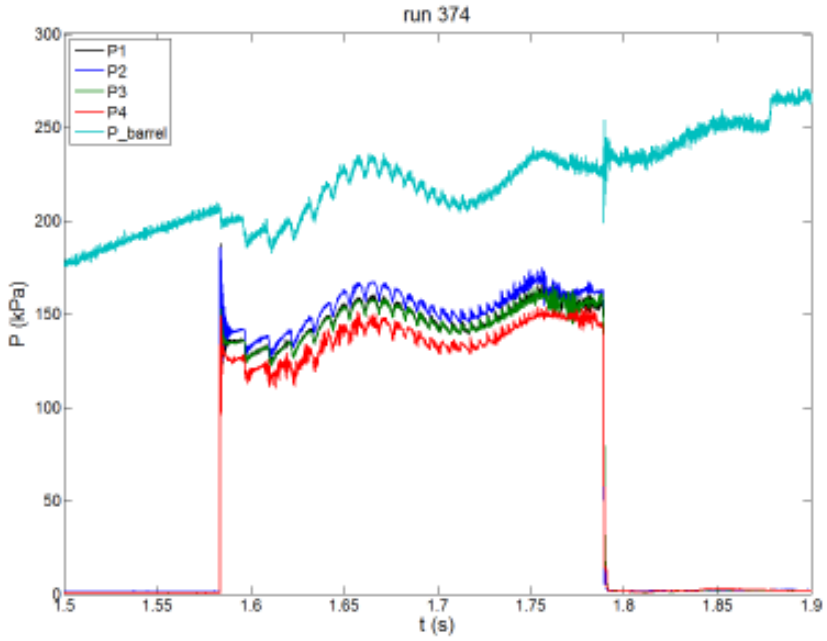


(a) Pitot pressure

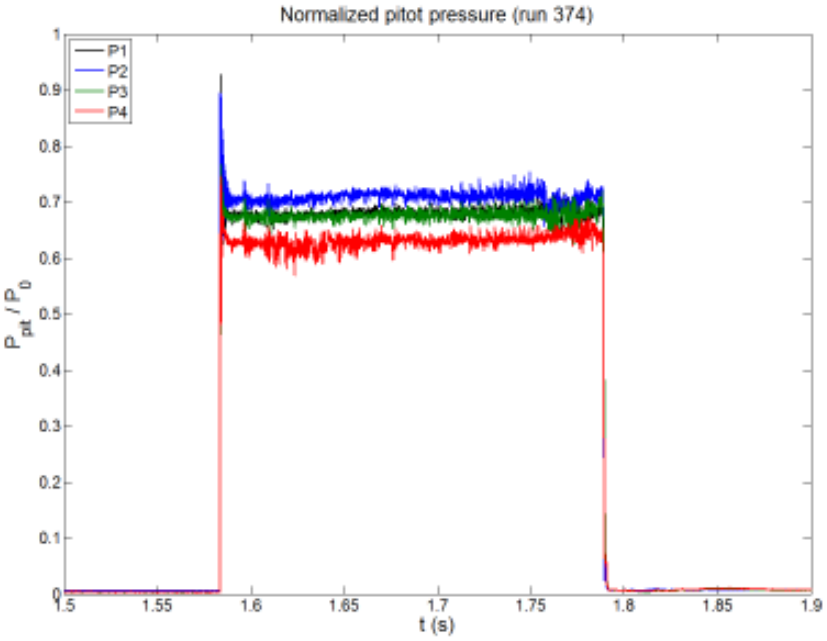


(b) Pitot pressure normalized with stagnation pressure

Figure 3.8: Time resolved pitot pressure measurement of the Mach 2 nozzle.

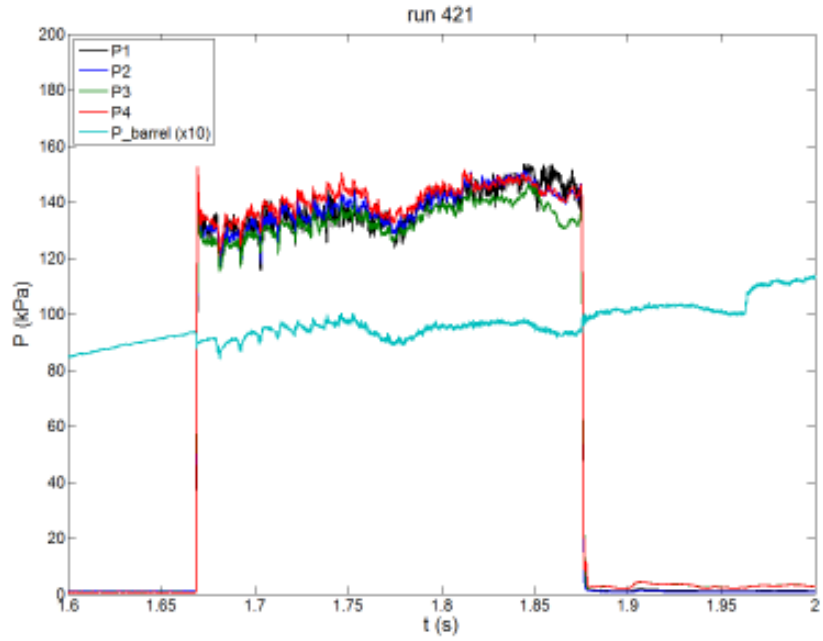


(a) Pitot pressure

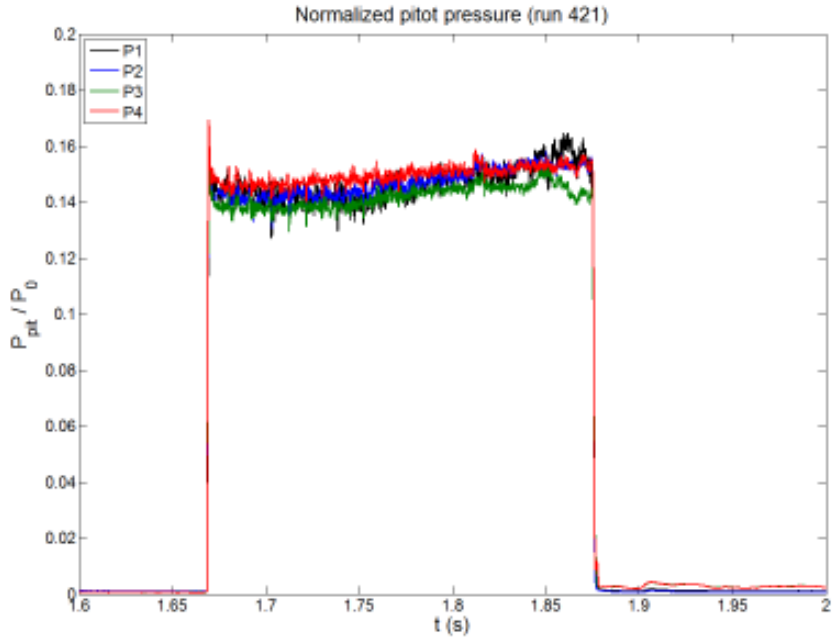


(b) Pitot pressure normalized with stagnation pressure

Figure 3.9: Time resolved pitot pressure measurement of the Mach 4 nozzle.

### 3.2.2 Summary of Test Flow Conditions

Results from the investigation of the thermal characteristics of TUSQ (Widodo, 2012) are shown in Figure 3.10. The compression ratio for TUSQ in the work of Widodo (2012) is the same as that ratio in the present work. The measured flow stagnation temperature during the initial 20 ms is approximately the same as that deduced with the assumption of isentropic compression from initial conditions up to the measured stagnation pressure during testing. A moderate temperature decrease of about 40 K occurs during the first 150 ms of test flow. After this time, a rapid drop of about 100 K occurs due to the arrival of vortical flow in the vicinity of piston (East and Qasrawi, 1978). The pitot pressure survey presented by Widodo (2012) demonstrates the Mach 6 nozzle has a uniform Mach 5.84 flow with a less than ±5% spatial variation over an 80.8 mm radius at the nozzle exit. A schematic illustration of the core flow produced by the Mach 6 nozzle is illustrated in Figure 3.11.

The conditions of the air flow for the experimental investigation in this work are summarized in Table 3.4. A constant compression ratio of the test air in barrel was used for all experiments in order to achieve nominally identity stagnation temperature across all conditions. Due to experimental variations arising during TUSQ operating, the burst pressure of identical thickness diaphragm may vary from the listed values in Table 3.2 and the stagnation pressure and temperature of nozzle exit flow will also vary as a consequence. Therefore, the flow properties of each test will be identified and reported individually along with the experimental results.

Table 3.4: Nominal flow conditions of TUSQ facility operating with Mach 2, 4 and 6 nozzles.

| **Conditions** | **Mach 6 nozzle** | **Mach 4 nozzle** | **Mach 2 nozzle** |
|---|---|---|---|
| $T_0$ (K) | 572±14 | | |
| Mach number | 5.84±0.03 | 3.94±0.02 | 2.05±0.05 |

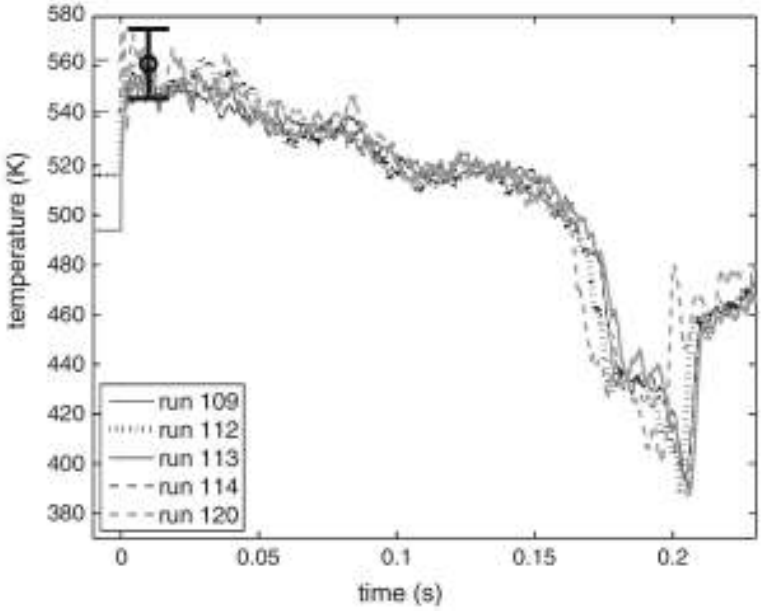


Figure 3.10: Flow stagnation temperatures in TUSQ achieved with the Mach 6 nozzle. The data points and error bars positioned at t=10 ms represents the averaged stagnation temperatures deduced from the assumption of isentropic compression during the period from 0 to 20 ms (Widodo, 2012).

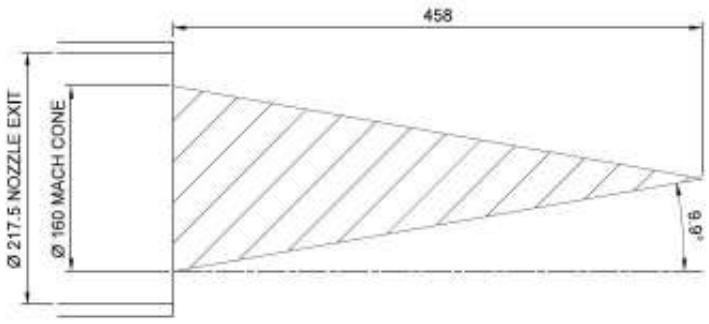


Figure 3.11: Core flow region of Mach 6 nozzle.

### 3.2.3 Variable Diaphragm Burst Pressure: Radiative Heating

During the operation of the Mach 4 nozzle with the hot surface model, an unexpectedly low and variable stagnation pressure of test flow was obtained. Radiation heating on diaphragm transmitted by a high reflectivity internal aluminium surface was suspected as the cause of the uncertain lower burst pressure. The reflection process from model

to diaphragm is illustrated in Figure 3.12. To minimize the reflections, black paint was applied to the internal surface of Mach 4 nozzle, see Figure 3.13, in order to absorb the radiation propagating upstream.

The evaluation of diaphragm temperature with and without black paint on the Mach 4 nozzle during the heating cycle was performed using a K-type thermocouple (dia. 0.3 mm) glued on to the diaphragm, see Figure 3.14. The test results presented in Figure 3.15 demonstrate that the black paint on the nozzle has virtually eliminated the radiation heating affect on the diaphragm, making the diaphragm burst pressure consistent when the hot surface model is used.

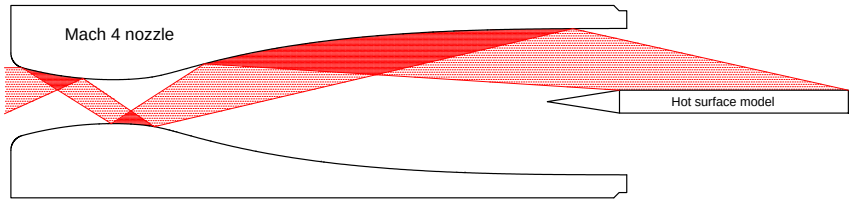


Figure 3.12: Schematic illustration of reflected radiation delivered from the hot surface model to the nozzle entrance.

Figure 3.13: Mach 4 nozzle with internal surface painted black.

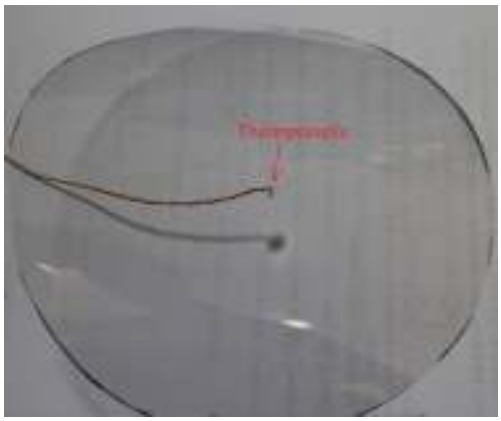

Figure 3.14: Diaphragm with attached thermocouple for temperature evaluation.

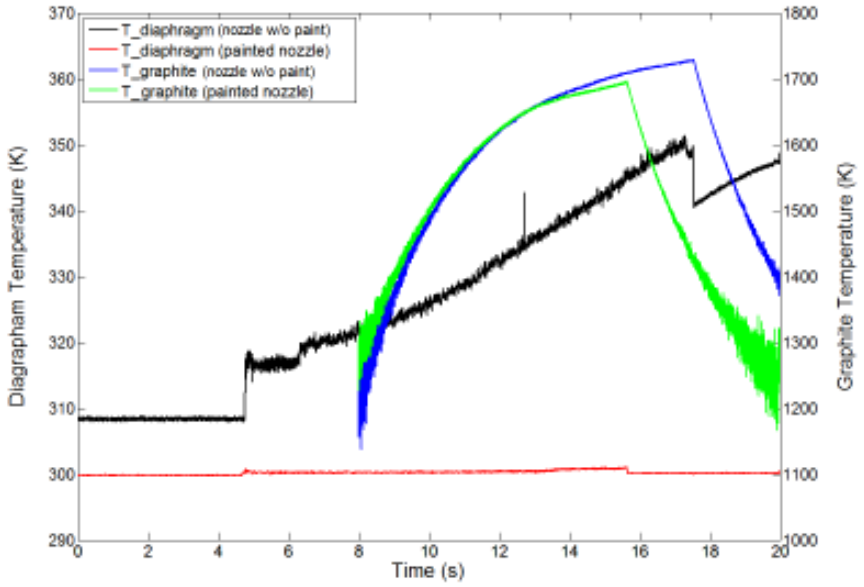


Figure 3.15: Temperature measurement illustrating the effect of reflected radiation transmitting from the hot surface model to the nozzle entrance.

## 3.3 Model Development

Although the important flow parameters such as Mach number, Reynolds number and total enthalpy can be produced in many short duration hypersonic wind tunnels, simulation of the almost adiabatic surface temperature due to hypersonic aerodynamic heating is a formidable task because the model remains more or less at ambient temperature during the short testing times that are frequently in the order of a few milliseconds (Bleilebens and Olivier, 2006). TUSQ produces relatively long duration test flows of around 200 ms but the flow has a low enthalpy, so achieving realistic flight wall temperatures is not possible through aerodynamic heating. To overcome this shortcoming, a preheatable model was designed and constructed. The model can be used for fundamental ignition and combustion studies in the TUSQ flow environments, but it may also find future application in fundamental studies in shock tunnels or other facilities where hypersonic flight enthalpies are correctly duplicated. A hot wall condition can be achieved by running an electrical current through the model before the high-speed flow experiment starts, as first proposed by Zander et al. (2012).

There are three key points that need to be considered carefully for the experimental system design. 1. The model support structure needs to facilitate a large amount of electrical power to be driven through the model during the preheating process. 2. The model need to be electrically insulated from the TUSQ facility. 3. The components of model need to tolerate the harsh thermal stress induced by heating the model to temperature as high as 1600 K and to survive flow-induced mechanical stress so that minimal refurbishment is necessary between runs. The thermal analysis of the preheated model was carried out to provide an optimized design and strategy for preheating operations.

### 3.3.1 Hot Surface Model Design

The methodology of preheating has been used for impulse facilities research. Hunt (2001) achieved wall temperatures of approximately 1200 K electrically heated using a thin graphite film on the model surface, while Zander et al. (2012) reached even as high as 2500 K also using an electrical preheating of carbon-carbon material. The concept of resistive heating involves running a current through the model, which generates a large and rapid delivery of energy into the model, causing the temperature to rise. The heating operation can be performed immediately before the wind tunnel is fired and in this manner, the model can be heated to the desired temperature at the time of flow arrival. A graphite tube was used as the hot surface model for testing as shown in Figure 3.16. The current used for the heating operation was obtained by using a controllable power supply (Miller Dynasty 700), see Figure 3.17.


Figure 3.16: Dimensions and photograph of the type of graphite tubes.


Figure 3.17: Miller Dynasty 700 power supply.

With the aim of the investigation being the combustion of hydrogen adjacent to a hot surface in hypersonic flows, the necessary experimental system was comprised three functional components: hydrogen injection system, water cooling system and electric current delivery system. The assembled experimental rig is illustrated in Figure 3.18, in which the flow route of hydrogen, cooling water and electrical current are depicted by using different colored arrows. The sting assembly needed to be capable of supporting the 1600 K graphite model while delivering up to 350 A of current through the graphite model at the same time. Copper was chosen for the supporting metal components because it has some distinct merits such as a high melting temperature, a large thermal capacity and a high thermal conductivity to transfer the heat energy away from the contacting surface which minimizes the temperature at the points of contacts with the graphite. The copper's property of low electrical resistance allows a high efficiency of energy transfer to the hot model. The water cooling system was designed to remove heat from the copper so that the integrity of soldered joints was maintained during the

model heating operation.

The hot wall model consists of a cylindrical graphite tube, a 'nose-cone' or 'step-cone' configuration for injection, both with a 9° half angle and other model support components. The nose-cone consists of two parts that provide an annular injector gap that is adjustable by screwing the tip-cone into the back-cone. The sectional view of nose-cone with main dimensions is shown in Figure 3.19. The step-cone was made from aluminum and was assembled with a copper pin-screw component which can screwed into the back-cone. The sectional view of step-cone with main dimensions is illustrated in Figure 3.20.

Two copper tubes with different diameters are soldered onto the back-cone and form the cooling water flow path; the outer tube can slide against the support mechanism. A compressed spring functions to compress the graphite tube, maintaining a low electrical contact resistance while allowing for thermal expansion of the components. The assembled model was mounted on the base plate within the test section and electrically isolated from it utilizing fiberglass, as shown in Figure 3.21. The properties of materials used to construct the model and associated systems are presented in Table 3.5.

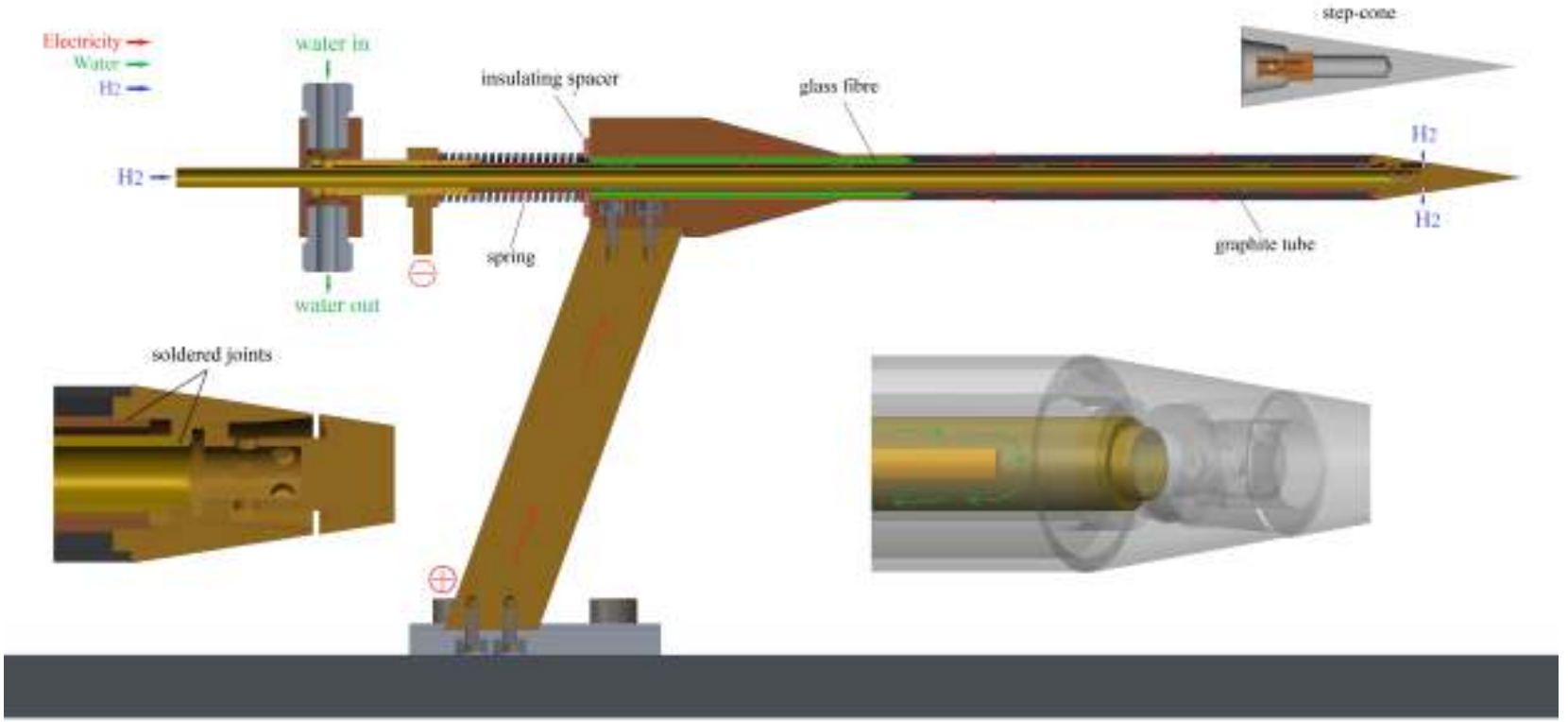


Figure 3.18: CAD views of hot surface model with nose-cone assembly.

Table 3.5: Properties of materials used for model construction.

| | **Copper** | **Graphite** | **Fiberglass** |
|---|---|---|---|
| Emissivity $\epsilon$ | 0.6 | 0.9 | - |
| Density $\rho$ $(kg/m^3)$ | 8933 | 1820 | 220 |
| Thermal conductivity $k$ $(W/mK)$ | 392 | 70 | 0.05 |
| Specific heat $c_p$ $(J/kgK)$ | 385 | 2160 | 837 |
| Melting point $(K)$ | 1356 | 3773 | 950 |
| Micro hardness $H$ $(J/kgK)$ | $1.089 \times 10^9$ | $1.089 \times 10^9$ | $5.0 \times 10^9$ |
| Surface roughness $\sigma$ $(\mu m)$ | 1.2 | 0.8 | 2.0 |

The properties of copper and fiberglass are from Kreith et al. (2010).

The properties of graphite are from `http://www.toyotanso.com/Products/Special_graphite/data.html`

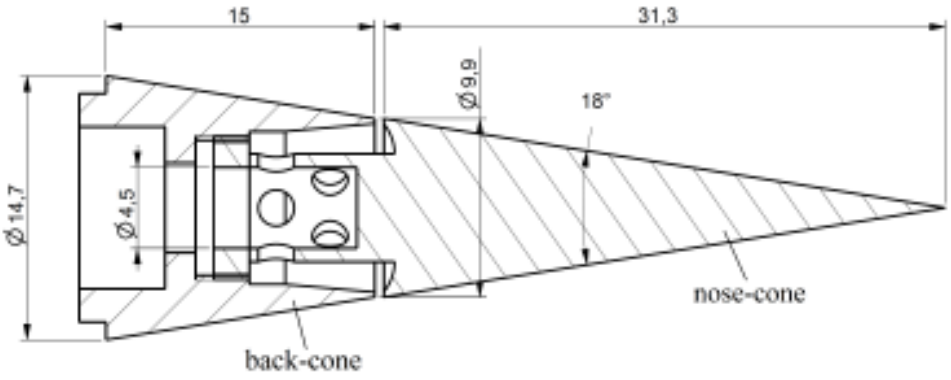


Figure 3.19: Sectional views of nose-cone with key dimensions.

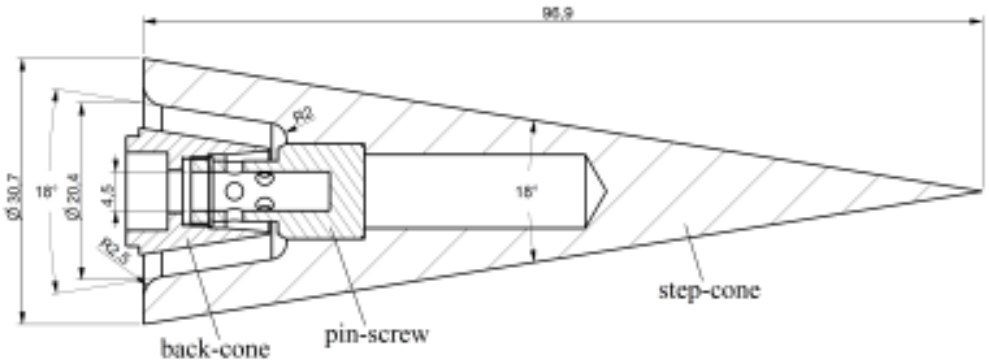


Figure 3.20: Sectional views of step-cone with key dimensions.

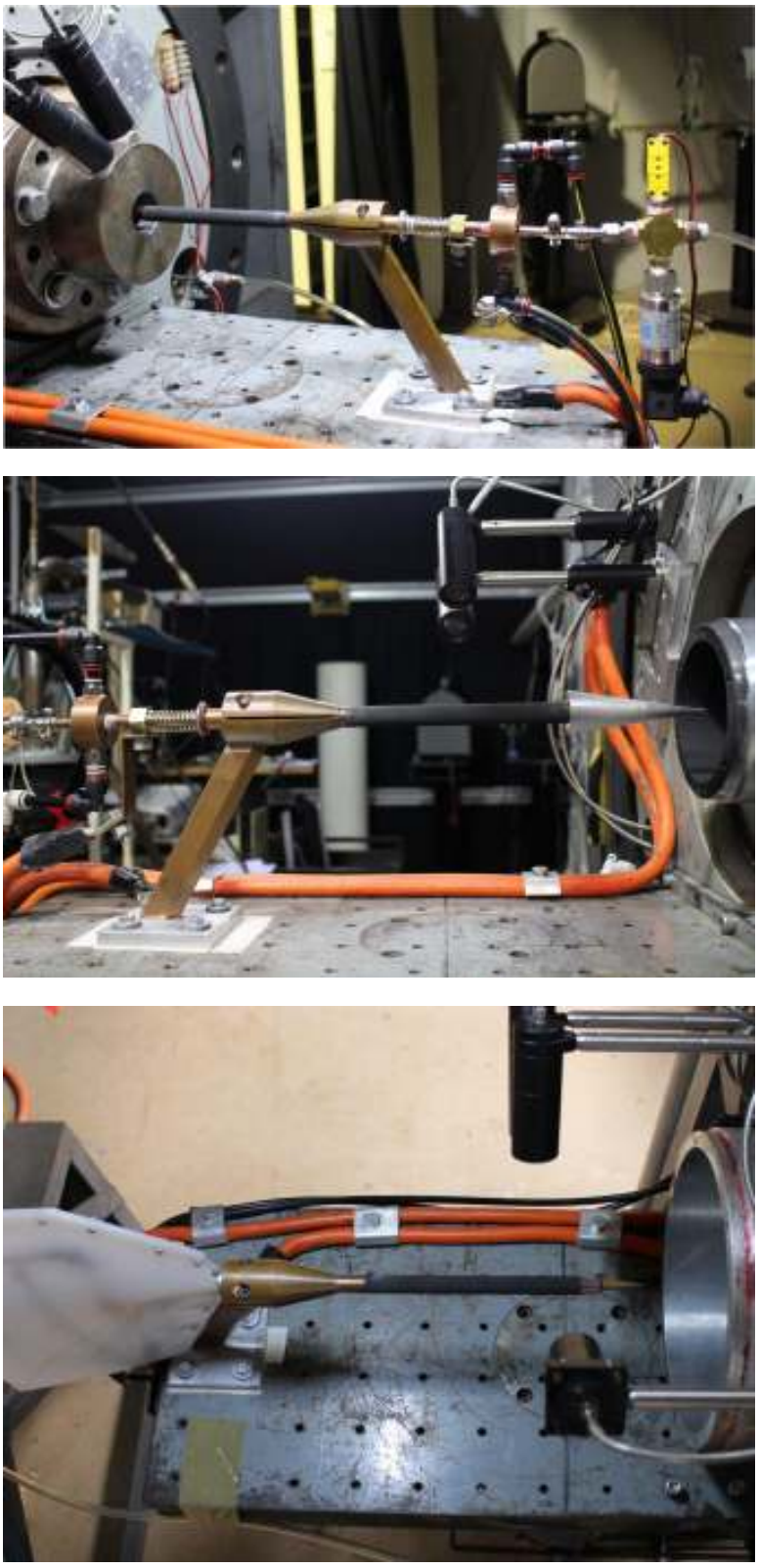

Figure 3.21: Photographs of model installation for heat-induced combustion testing. From top to bottom: Mach 2, Mach 4 and Mach 6 nozzle arrangements.

### 3.3.2 Thermal Analysis

The high temperatures ($T > 1000\,K$) introduced by electrically heating models is a challenge for metallic components to survive during the experimental campaign. Because the silver brazing alloy (ProSilver 45 T) has a lower melting point of 913 K relative to the copper parts (nominally 1358 K ), particular attention needs to be paid to the soldered joints during the design process. The locations of the soldered points is illustrated in Figure 3.18. The failure of the soldered joints can lead to cooling water leaking and therefore can cause sever damage.

Thermal analysis is necessary to simulate the thermal performance of model and associated systems, in order to reduce the risks and to avoid the damage and costs that might be caused by model failure. An optimized strategy for preheating operations will be determined so that the model and associated system can endure the harsh working conditions during the heating process. Two methods of thermal analysis of the heated model were undertaken in this study: (1) using a one-dimensional model and (2) performing a three-dimensional numerical simulation coupling solid and fluid using the commercial software Ansys. Note that although the physical model is nominally axisymmetric, because the water flow is not, a three-dimensional analysis was necessary.

#### 3.3.2.1 One-dimensional Model

In this section, the one-dimensional thermal analysis model is presented for transient temperature assessment in the model heating process.

Figure 3.22 illustrates the arrangement used for the one-dimensional thermal analysis model and the schematic diagram shows the heat transfer between the model's components. The thermal analysis is simplified by assuming that the temperature is uniform within each component during the heating process and neglecting the contact thermal resistance. The transient temperature heat capacity of components are expressed in Eq. 3.4 to 3.8 in terms of the power supplied to graphite sample ($P$) and the heat transfer ($q$). Note that subscript $r$ and $c$ indicate the heat transfer caused by radiation and conduction respectively. The thermal properties of the hot wall model components

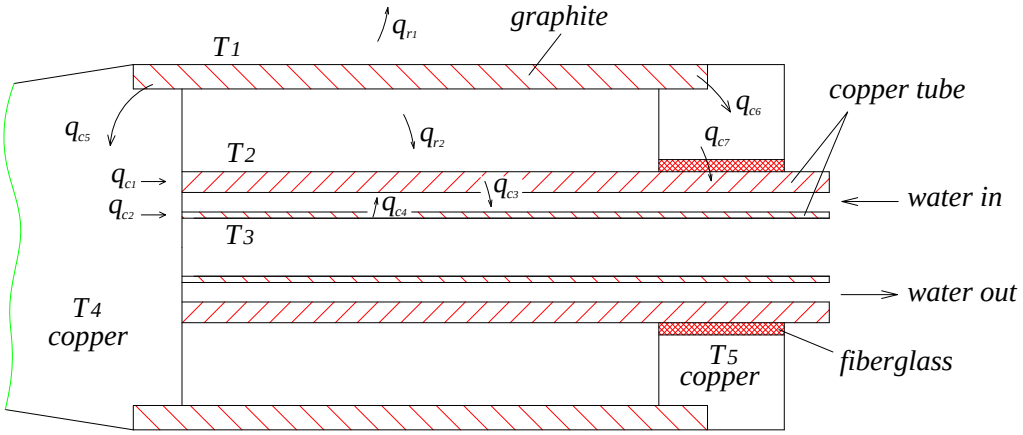


Figure 3.22: Schematic illustration of one-dimensional thermal analysis model.

are presented in Table 3.5. The cooling water is supplied by normal running water in the TUSQ laboratory and the flow speed was determined by a measured out-flow rate of $8.15 \times 10^{-3}$kg/s.

$$\frac{\mathrm{d}T_1}{\mathrm{d}t} = \frac{P - q_{r1} - q_{r2} - q_{c5} - q_{c6}}{m_g c_g} \tag{3.4}$$

$$\frac{\mathrm{d}T_2}{\mathrm{d}t} = \frac{q_{r2} + q_{c1} + q_{c7} - q_{c3}}{m_{co} c_c} \tag{3.5}$$

$$\frac{\mathrm{d}T_3}{\mathrm{d}t} = \frac{q_{c2} - q_{c4}}{m_{ci} c_c} \tag{3.6}$$

$$\frac{\mathrm{d}T_4}{\mathrm{d}t} = \frac{q_{c5} - q_{c1} - q_{c2}}{m_{cb} c_c} \tag{3.7}$$

$$\frac{\mathrm{d}T_5}{\mathrm{d}t} = \frac{q_{c6} - q_{c7}}{m_{ce} c_c} \tag{3.8}$$

The solution of these five differential equations and the coupling relationships for $q_r$ and $q_c$ was achieved using the ODE45 solver in Matlab. For the details of heat transfers $q_r$ and $q_c$ and the technical solution procedure, readers can refer to the Matlab commented scripts in Appendix B.1. The merits of the one-dimensional thermal analysis is its high calculation efficiency. The solution time was of the order of seconds in contrast to the Ansys simulations that typically took tens of hours.

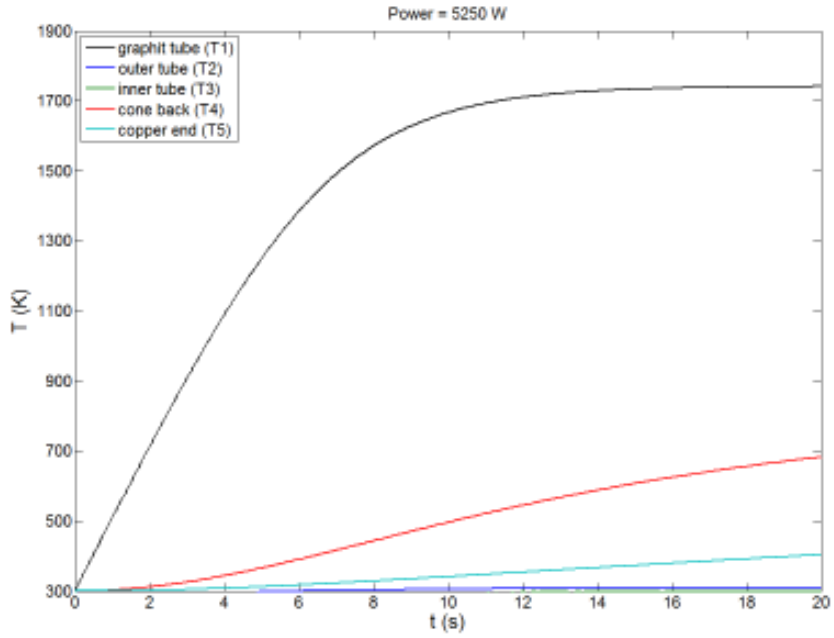


Figure 3.23: Calculated temperature history of hot wall model components.

The calculated transient temperature history for a power of 5250 W delivered to the hot surface model is shown in Figure 3.23. The initial temperature was set at 300 K. The results suggest that the temperature of graphite sample increases quickly during the initial 8 seconds reaching 1500 K and then the temperature increase slows down and reaches a maximum temperature of about 1700 K at 20 seconds. It is noticeable that the temperature of other components increases at a moderate rate during the whole heating cycle. Taking into consideration of the low melting point of the soldering material, the present analysis indicates the current should be cut off at about 10 seconds. Although it does not include the detailed information of temperature distribution within the components, the one-dimensional thermal analysis model offers a fast prediction of electrical power required to achieve the target temperature of the hot surface model.

#### 3.3.2.2 Coupled Thermal-fluid Numerical Simulation in Ansys

Because the one-dimensional model cannot provide detailed information on temperature distribution within components, a coupled thermal-fluid 3-D numerical simulation was carried out using the commercial software Ansys. The temperature results from the Ansys simulations provide more detailed information and therefore assist in determining

whether the heating strategy is reliable for the hot surface model.

A new set of System Coupling components is offered since the introduction of Ansys version 15.0 that facilitates comprehensive multidisciplinary simulations (ANSYS Guide, 2013). This new function allow users to accurately and efficiently analyze the transient structural temperatures of solids coupled with fluid cooling.


Figure 3.24: Diagram illustrating the connection of a system via coupling of fluid and thermal simulations.

The schematic overview diagram shown in Figure 3.24 describes the implementation procedure of the approach that couples the CFD code FLUENT and the structural mechanics assessment FEM program. The execution of fluid and solid coupling computation established between the CFD model and the FEM analysis model allows interchanging heat at the wall between the fluid and the solid by a defined two-way data transfer interface. For each time step, a steady-state CFD simulation and thermal analysis via FEM are performed to accommodate the changed boundary conditions.

The simulated case is based on the hot surface experimental setup which has been described in the preceding section as shown in Figure 3.18. The low pressure (0.7 kPa approximately) environment in the evacuated test section suggests the heat transfer caused by natural convection could be small relative to that caused by radiation and conduction during the preheating. A quantitative comparison of natural-convection and radiation of the heated graphite is achieved through an empirical correlation for a horizontal cylinder (Kreith et al., 2010),

$$Nu = 0.53(G_r P_r)^{\frac{1}{4}} \tag{3.9}$$

$$Gr = \frac{9.8d^3\rho^2(T - T_\infty)}{T_\infty \mu^2} \tag{3.10}$$

$$\dot{q}_{conv} = \frac{N_u\, k}{d}(T_g - T_\infty) \tag{3.11}$$

and the Stefan-Boltzmann law,

$$\dot{q}_{rad} = \epsilon\sigma_s(T_g^4 - T_\infty^4) \tag{3.12}$$

where $P_r = 0.71$ is assumed a constant, $Gr$ is Grashof number, the viscosity $\mu$ and thermal conductivity $k$ of air are calculated by Sutherland's law (White and Corfield, 2006), $d$ is graphite sample diameter, $\epsilon = 0.9$ is the emissivity of graphite and $\sigma_s = 5.67 \times 10^{-8}\,\mathrm{Wm^{-2}K^{-4}}$ is the Stefan-Boltzmann constant.

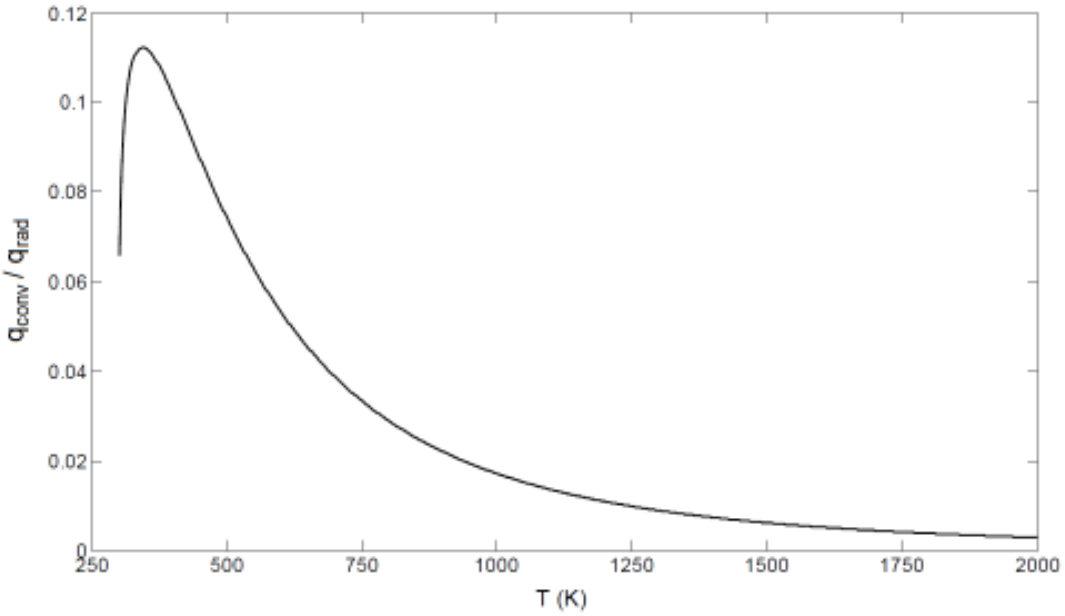


Figure 3.25: The ratio of heat transfer caused by natural-convection and radiation of heated graphite tube.

Figure 3.25 presents the ratio derived from Eq. 3.11 and 3.12, and demonstrates the heat transfer caused by natural-convection only accounts for a relatively small fraction of heat loss, peaking at about 11.2% at a temperature of around 350 K and falling to a value less than 1% for temperatures in excess of 1250 K. Therefore, the radiation and

conduction heat transfer were both included in the thermal analysis of the graphite and associated copper in the Ansys, but natural convection was neglected.

Because the model is assembled with different materials, the interface thermal contact resistance between the components can affect the conducted heat flow significantly and consequently the contact temperatures. Thus, quantification of the interface thermal resistance is important to achieve a good thermal simulation.

Heat transfer between the contacting interfaces takes place by three different paths: (1) conduction through the micro contacts; (2) conduction through the interstitial fluid in the gap; and, (3) thermal radiation across the gap if the interstitial substance is transparent to radiation (Bahrami, Culham and Yovanovich, 2003). The interface resistance is a complex issue that is primarily a function of surface roughness, the properties of the contacting materials, the pressure holding the two surfaces in contact, the interface fluid, and the interface temperature. The heat transmitted by the interstitial fluid was neglected due to the evacuated low pressure environment as discussed previously. Therefore, the thermal interface resistance $R_c$ is expressed as

$$R_c = \left( \frac{1}{R_s} + \frac{1}{R_r} \right)^{-1} \tag{3.13}$$

where $R_s$ and $R_r$ are the paralleled thermal resistance corresponding to solid contact and radiation. The solid contacting resistance is recognized as being caused by the real area of micro-contact spots which is only a small fraction of the nominal contact area, typically a few percent (Greenwood and Williamson, 1966). Here $R_s$ was estimated using the conductance correlation introduced by Yovanovich (1981).

$$R_s = \frac{\sigma/m}{1.25 k_s (P/H)^{0.95}} \tag{3.14}$$

where $\sigma = \sqrt{\sigma_1^2 + \sigma_2^2}$ is the effective RMS surface roughness of the contacting asperities, $m = \sqrt{m_1^2 + m_2^2}$ is the effective mean absolute asperity surface slopes of the interface, $k_s = 2k_1k_2/(k_1 + k_2)$ is the harmonic mean thermal conductivity, $P$ is the apparent pressure and $H$ is the micro hardness of the softer material. Subscripts 1 and 2 re-

fer to contacting materials. The mean absolute asperity slope is approximated by the correlation equation $m = 0.125(\sigma \times 10^6)^{0.402}$ (Antonetti, Whittle and Simons, 1993). The softness of graphite physical characteristic in reality can promote the formation of micro-contacts resulting in the decreased thermal resistance. Four types of contacting interface exist within the hot model testing rig and the corresponding contacting thermal resistances are listed in Table 3.6.

Table 3.6: Contacting thermal resistance.

| **interface** | **Copper - graphite** | **Copper - copper** | **Copper - fiberglass** | **Copper - aluminium** |
|---|---|---|---|---|
| $R_s\,(m^2K/W)$ | $0.9 \times 10^{-5}$ | $2.0 \times 10^{-5}$ | 0.05 | $1.5 \times 10^{-5}$ |

Thermal radiation across the gap remains small as long as the surface temperature are below 700 K and in most applications can be neglected (Bahrami, Culham and Yovanovich, 2004). Considering the details of the heating process of the hot surface model, the temperature of the contacting solid surface should not exceed this condition, except at the graphite-copper contact. The graphite-copper contacting thermal resistance $R_r$ is evaluated over the target temperature range of the hot surface model, and is expressed as

$$R_r = \frac{T_g - T_c}{F_{gc}\sigma_s(T_g^4 - T_c^4)} \tag{3.15}$$

where $F_{gc}$ is the shape factor that can be calculated by

$$F_{gc} = \frac{1}{\frac{1}{\epsilon_g} + \frac{1}{\epsilon_c} - 1} \tag{3.16}$$

Eq. 3.15 suggests that the graphite-copper interface radiant thermal resistance $R_r$ is a function of temperatures and contacting solid surface emissivity. Figure 3.26 shows $R_r$ varies within the range of 0.0054 to 0.0141 when graphite and copper temperatures are considered to be within the ranges of 800 to 2000 K and 800 to 1300 K, respectively. The values of radiant thermal resistance is much bigger than that of contacting thermal resistance by three orders of magnitude within the specified temperature range.

Therefore the radiation heat transfer within the contact is negligible for the current thermal analysis.

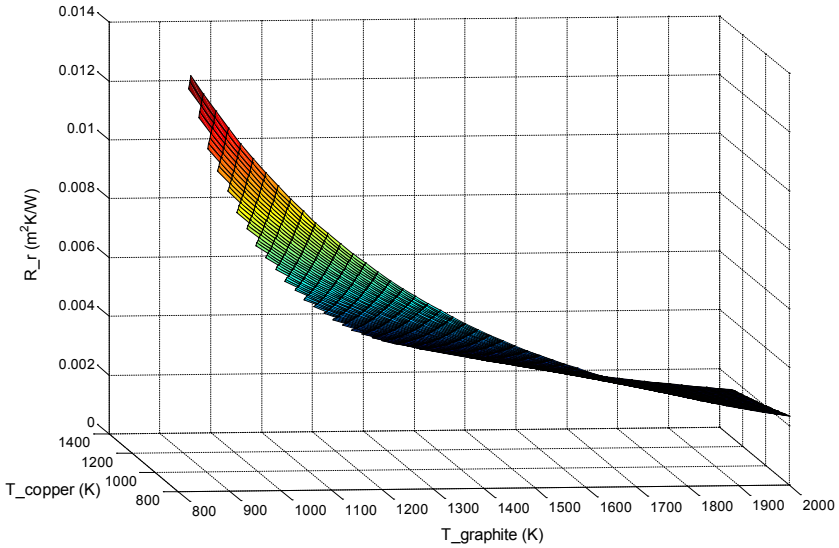


Figure 3.26: The estimated radiant thermal resistance $R_r$ within the temperature range of the contacting surface: graphite 800∼2000 K and copper 800∼1300 K.

The commercial CFD package Fluent was used with the $k-\varepsilon$ turbulence model and scaled wall function for fluid simulation. Standard water properties were taken from the Fluent material properties database. The initial thermal and fluid flow conditions are listed in Table 3.7. The electric power of 5250 W applied to the hot surface model is the same as that of the one-dimensional model analysis in Section 3.3.2.1. The transient numerical simulation was performed for a duration of 20 s of physical time, with a time-step of 0.1 s.

Table 3.7: Thermal and fluid boundary conditions for coupled numerical simulations.

| **Solid** | | **Fluid** | |
|---|---|---|---|
| **Power (W)** | **Initial T (K)** | **Inlet u (m/s)** | **Inlet T (K)** |
| 5250 | 295 | 7.72 | 295 |

In order to simplify the mesh generation process, some miscellaneous features such as threads, chamfer, holes for assembly etc. were removed from the real model geometry. Two types of mesh were generated as shown in Figure 3.27a: tetrahedral for irregu-

lar shaped bodies and hexahedral for regular shaped bodies. The computed results of temperature distribution at a simulation time of 20 seconds are presented in Figure 3.27b. The temperature of the graphite tube reached a maximum of 1790 K, but it is distributed nonuniformly along the cylinder axis, see Figure 3.28. The temperature at both ends of the hot graphite surface decreases dramatically due to the heat conduction and reaches 95% of its highest values at a location of 15 mm from the leading edge and 10 mm from the trailing edge.

The comparison of highest temperature of graphite simulated using Ansys, the 1-D model analysis results and measured temperature during a preheating test is shown in Figure 3.29. Temperature measurements were obtained using the two color ratio pyrometry method described in Section 3.5.1. The monitoring point for the temperature measurement was the axial center of the graphite tube and the detailed principle and validation of this method is discussed in Section 3.5.1. Note that the observation of sudden drop of measured graphite surface temperature at about 13 s is caused by the shut off of the power supply.

Figure 3.30 illustrates the CFD results of the temperature distribution, heat transfer coefficient and heat flux within the fluid at a simulation time of 20 seconds. The maximum values of heat transfer coefficient occurred at the turning corner of the flow path near the left hand end, shown in Figure 3.30b, where the impingement of turning water enhanced the cooling effect. Consequently, a large amount of heat was taken away by cooling water in this region, see Figure 3.30c.

The coupled CFD and FEM numerical simulation offers some insight to the temperature evolution and distribution within the apparatus during the preheating process. To improve clarity in judging the risk of the preheating operation, the simulated temperature distributions of model apparatus are illustrated in Figure 3.27c to 3.27h. Based on these results, the overall conclusion is that the hot surface model can be operated safely without compromising the mechanical integrity of the system through overheating using the current configuration while targeting a surface temperature of around 1700 K which is suitable for the planned heat-induced combustion investigations.

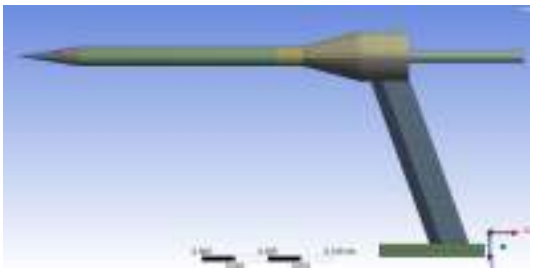

(a) Mesh generated for FEM simualtions

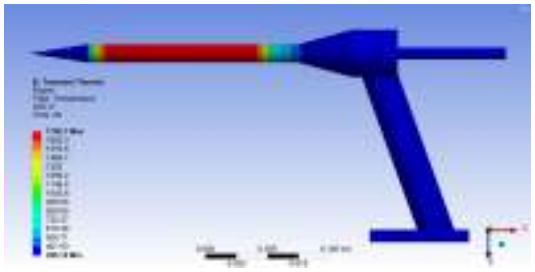

(b) Overall temperature distributions

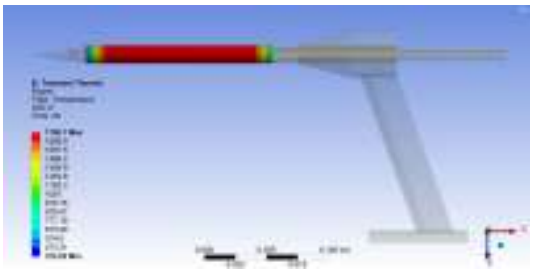

(c) Graphite

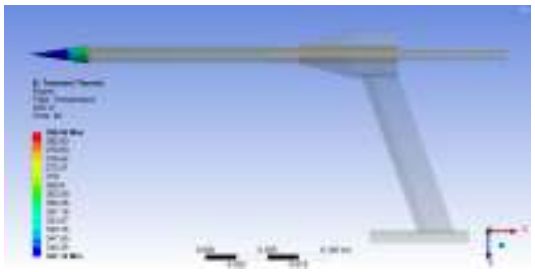

(d) Nose cone

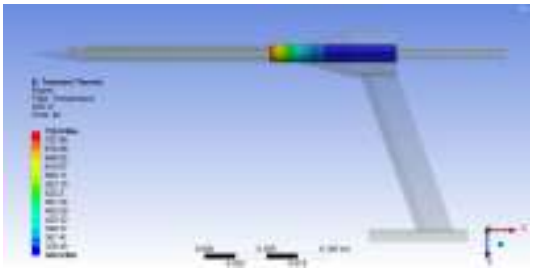

(e) Back copper

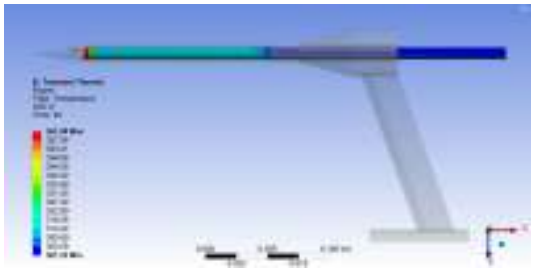

(f) Outer-tube

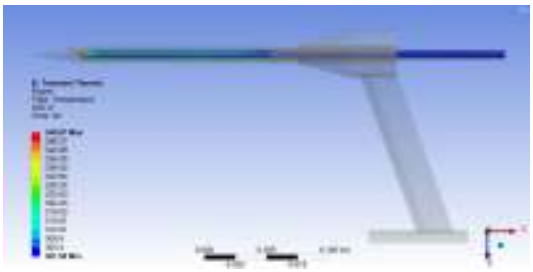

(g) Inner-tube

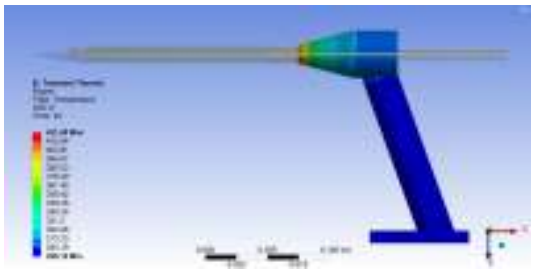

(h) Support rigs

Figure 3.27: Mesh generated for solid element simulations and temperature distributions at simulation time of 20 seconds.

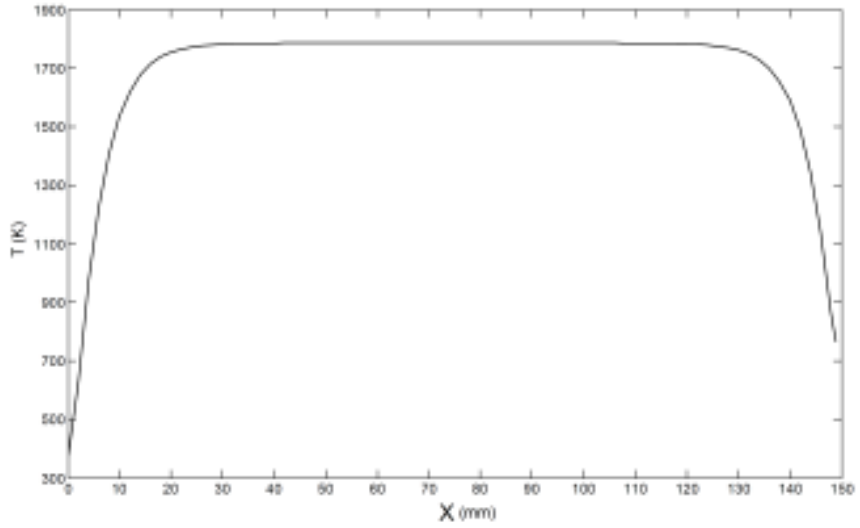


Figure 3.28: Axial temperature distributions along the graphite tube. x = 0 refers to the leading edge of the graphite tube.

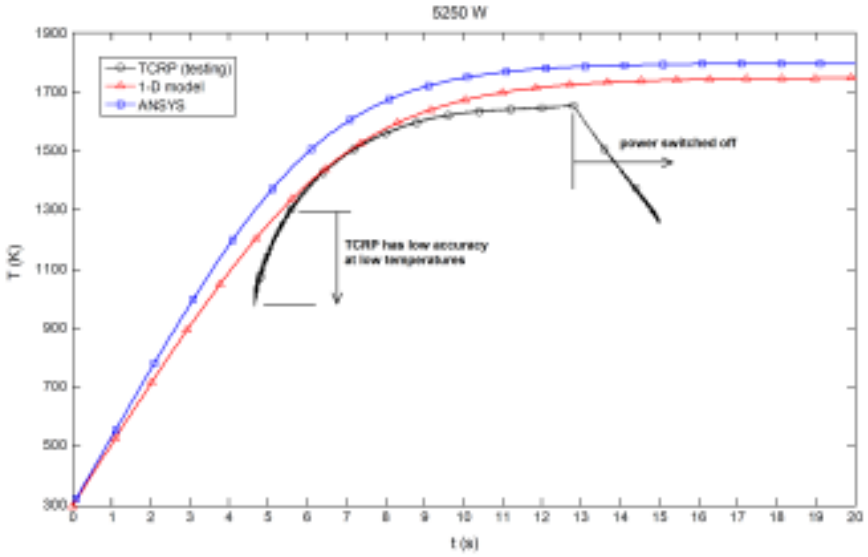


Figure 3.29: Time-resolved graphite temperature variation: comparison of 1-D analysis model, numerical simulation and TCRP measurement.

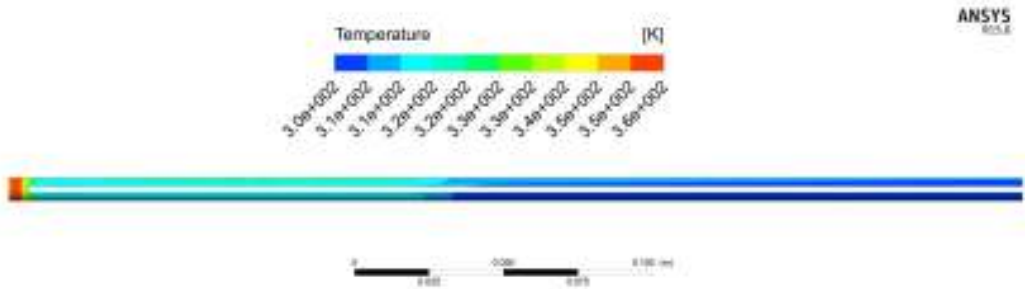


(a) Temperatrue distribution within the fluid and the outer-tube interfacing wall

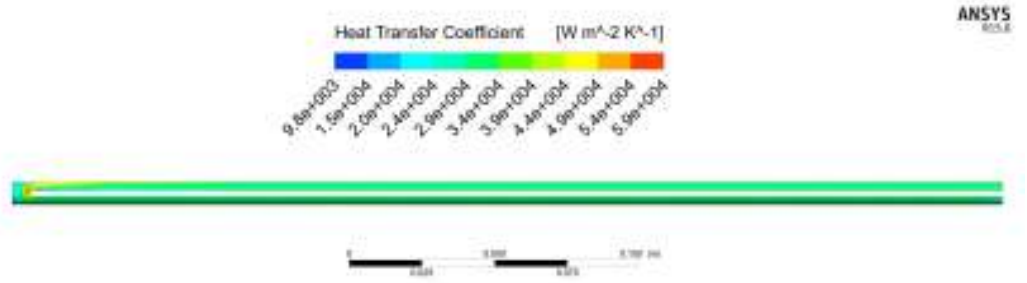


(b) Heat transfer coefficient within the fluid and the outer-tube interfacing wall

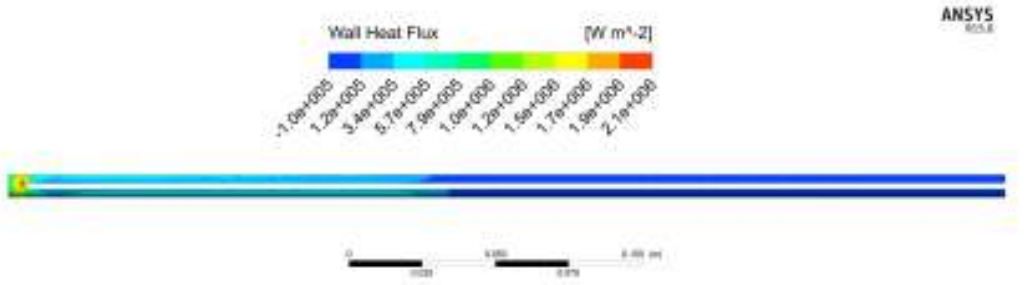


(c) Heat flux within the fluid and the outer-tube interfacing wall

Figure 3.30: CFD results for the fluid component at a simulation time of 20 s.

### 3.3.3 Static Pressure Measurement Model

Nose-cone and step-cone models for static wall pressure surveys were constructed using a 3D Printing technology as shown in Figure 3.31 and 3.32. These two printed models duplicate the key dimensions of the hot surface model as well as the internal geometry of the hydrogen-delivering flow path structures. Pressure measurement orifices (dia.=0.8 mm) with equal axial spacing were connected to pressure sensors via pneumatic tubes and were included in the 3D printed model. The positions of 9 pressure

orifices with a spacing distance of 15 mm for the nose-cone model and those of 8 pressure orifices with the spacing distance of 12 mm for the step-cone model are depicted in Figure 3.33 and 3.34, respectively. The installed pressure measurement models within the test section are shown in Figure 3.35.

The nose-cone model was designed with a removable tip and main body so that it could be adapted for validating the fuel delivery system by replacing the tip with a pressure measurement nipple.

Figure 3.31: CAD view of the 3D printed nose-cone model.

Figure 3.32: CAD view of the 3D printed step-cone model.

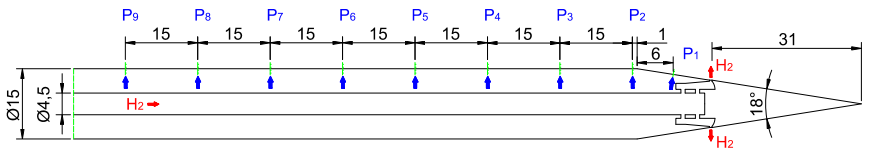


Figure 3.33: Positions of 9 pressure transducers in the nose-cone model.

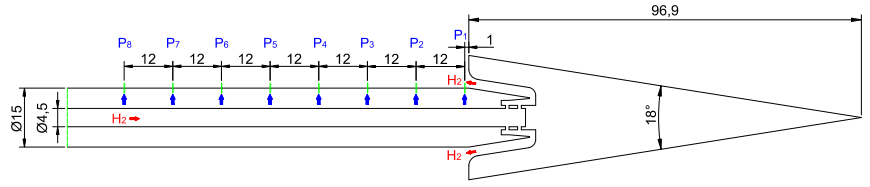


Figure 3.34: Positions of 8 pressure transducers in the step-cone model.

(a) Nose-cone installation with Mach 6 nozzle (b) Step-cone installation with Mach 4 nozzle

Figure 3.35: Photographs of the installed static pressure measurement models within the test section.

## 3.4 Fuel System

A dedicated fuel supply system was designed and constructed for the heat-induced combustion experiments with the aim of maintaining a steady injected fuel flow during the hypersonic testing time. The fuel supply system can be operated in two different modes: pure hydrogen delivery and premixed hydrogen-air delivery. The jet penetration affects fuel and air mixing and is itself significantly influenced by the local flow conditions when the nose-cone model is used. Therefore, to accurately specify the jet flow, it is important to define the flow conditions under which the testing is taking place. The identification of injected flow conditions is described through the combination of analysis and measurements presented in this section.

### 3.4.1 Fuel Supply System Design

One possible scenario for one-dimensional adiabatic flow with friction in a constant-area duct downstream of a nozzle as shown in Figure 3.36 is that the flow is chocked at the nozzle throat followed by supersonic flow downstream (Oosthuizen and Carscallen, 1997). The characteristics of the flow in the constant-area duct is determined by the length of duct with certain friction coefficient $c_f$ and back ground pressure $P_b$. The effect of wall friction and heat flux to the flow (the situation that occurs in present

testing) always drives the Mach number of duct flow toward 1, decelerating a supersonic flow or accelerating a subsonic flow, and causing loss of the total pressure.

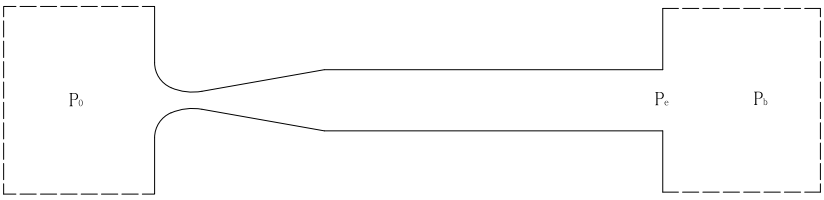


Figure 3.36: Schematic illustration of nozzle-duct flow with friction.

In the case of adiabatic flow with friction, a minimum length of duct is necessary to achieve the choking flow condition at the outlet for a given nozzle geometry and the wall roughness of duct when the back pressure is below the critical pressure $P_e^*$ for choking flow at the outlet. In the adiabatic case, increasing the length of the duct will only affect the flow structures; the total pressure loss and the choking flow parameters at the duct outlet will remain the same as long as chocked flow is established at the nozzle throat. Assuming an adiabatic flow process, the choking flow parameters at the outlet of the nozzle-duct can be calculated using (Oosthuizen and Carscallen, 1997):

$$T_e = \frac{2\,T_0}{\gamma + 1} \tag{3.17}$$

$$P_e = P_0(1 + \frac{\gamma - 1}{2}M^2)^{\frac{\gamma}{1-\gamma}} \cdot M\sqrt{\frac{2 + (\gamma - 1)M^2}{\gamma + 1}} \tag{3.18}$$

where $P_0$ and $T_0$ are the stagnation pressure and temperature upstream of the nozzle, $P_e$ and $T_e$ are the static pressure and temperature at the duct exit, and $M$ denotes the Mach number at the nozzle exit. Although the internal flow details may be complex, the overall effect of the friction tends to lead to choking flow at the exit and thus the fuel delivery system itself functions to some degree as a self-moderating unit.

CAD views of fuel system are given in Figure 3.37. Design of the system followed the preceding philosophy with the aim of obtaining a steady jet flow during the heat-induced combustion testing. The fuel supply system was designed to operate with two

different modes: (1) pure hydrogen delivery; and (2) premixed hydrogen-air mixture delivery. The solenoid valve ② is triggered by the wind tunnel triggering system while the solenoid valve ① is manually operated. The solenoid valve ① is kept closed when the experiment is conducted with fuel delivery of pure hydrogen, and it is opened manually before the wind tunnel shot and is shut down after the termination of the wind tunnel operation when the premixed hydrogen-air experiment is performed.

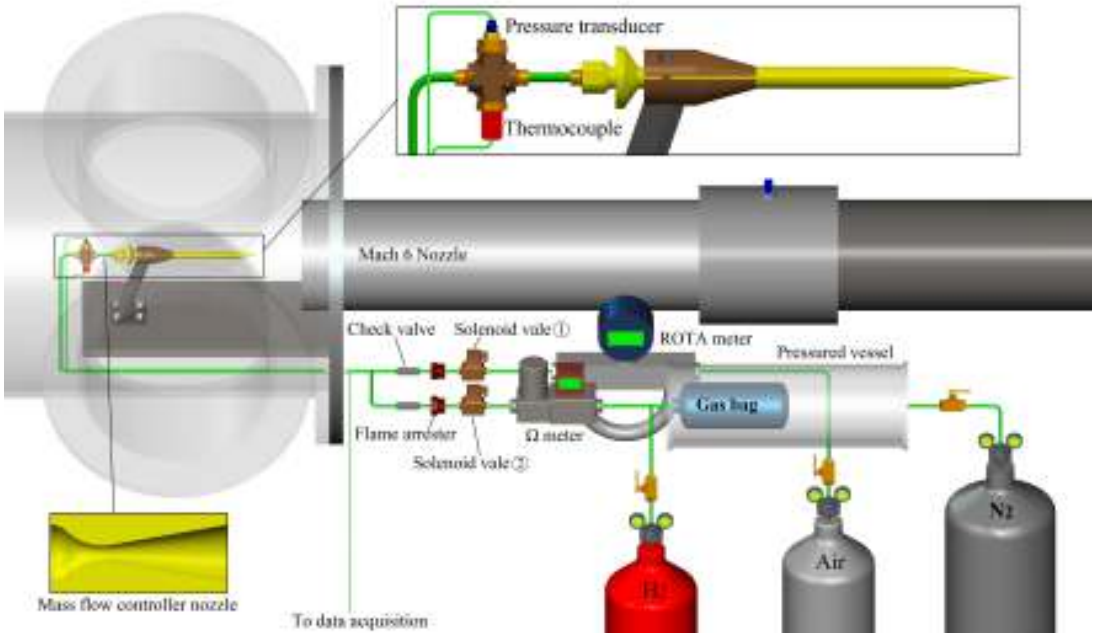


Figure 3.37: CAD views of fuel delivery system.

A K-type fine wire thermocouple (OMEGA, dia. 0.001 inch) with an estimated time constant of 0.01 s (Kreith et al., 2010) and a DRUCK pressure transmitter (PTX1400, 25 Bar) are mounted on a brass cross. Two fast-acting solenoid valves (Normally closed, PROCESS SYSTEMS B35) to control the timing of hydrogen and air delivery are mounted in each line. The mass flow rates of hydrogen and air are measured by OMEGA flow controller (FMA-2600A) and ROTA mass meter (YOKOGAWA, RCCS32), see Figure 3.38. The check valves are mounted in each line to ensure mixing of air and hydrogen does not occur upstream of these devices. The target pressure of the premixed hydrogen-air in the delivery lines was below 200 kPa. The investigation of quenching meshes in arresting hydrogen combustion suggested that the quenching distance has a minimum near stoichiometry and is inversely proportional to initial pressure (Yang

et al., 2003), as shown in Figure 3.39. Two bespoke flame arresters utilising stainless steel metal mesh with an aperture of 0.132 mm were installed upstream of the check valves. The flame arresters will prevent the flame propagation back upstream if the premixed hydrogen-air mixture is ignited accidently and the check valves do not close fast enough.

A 600 mm length of flat hose with diameter of 63 mm made of synthetic fibers and soft PVC is utilized as a flexible hydrogen gas bag having a maximum inflated volume of approximately 2 liters as shown in Figure 3.40a. A stainless steel vessel with a volume of 20 liters approximately enclosing the hydrogen gas bag is pressurized by filling it with nitrogen. Pressure and leak testing of the vessel was undertaken by using a hydraulic pumping device as shown in Figure 3.41. The pressure holding capability of the vessel container was demonstrated through a test by pressurizing it at 2.5 MPa, and no leaking was detected. Hydrogen pressure for fuel injection can be built up through the following two steps: (1) adjust the vessel container pressure to target values; and (2) carefully fill hydrogen to a gas bag pressure about 10 kPa above that of the nitrogen vessel.

The atmospheric pressure blow-down mode is an alternative method for pure hydrogen injection at lower total pressure. This operating mode is achieved by replacing the pressure vessel and synthetic PVC hose with the device shown in Figure 3.42. The device is composed of a PVC pipe ($\phi$=250 mm), a exhaust fan (50 W) mounted on top and a metal mesh with an aperture of 0.57 mm covering an observation window and a soft flexible bag (a cask-wine bladder) as shown in Figure 3.40b. The stainless mesh and exhaust fan were selected with reference to flame a quenching distance of 0.64 mm (Kuznetsov, Kobelt, Grune and Jordan, 2012) and flame speed of 3 m/s (Turns et al., 1996) of stoichiometric hydrogen-air mixture at pressure of 1 bar. The detailed description of this device can be found in Appendix A.

A 3D printed nozzle with a throat diameter of 1.2 mm was assembled in-line as a mass flow controller located downstream of the brass cross. The main dimensions of the mass control nozzle (MC nozzle) are shown in Figure 3.43. The time period of 2 seconds of hydrogen injection can be estimated by its volumetric rate when the flow is chocked in

the MC nozzle

$$\dot{V} = KRA^* \sqrt{T_0} \tag{3.19}$$

where $A^*$ is the throat area, $K = 0.0107$ (sK$^{0.5}$/m) and $R = 4124.6$ (J/kgK) for hydrogen. The flow duration of injection is a very important factor that impacts the system triggering arrangement.


(a) OMEGA flow controller (a laminar flow device)

(b) ROTA mass meter (a coriolis device)

Figure 3.38: Photographs of the mass flow meters.

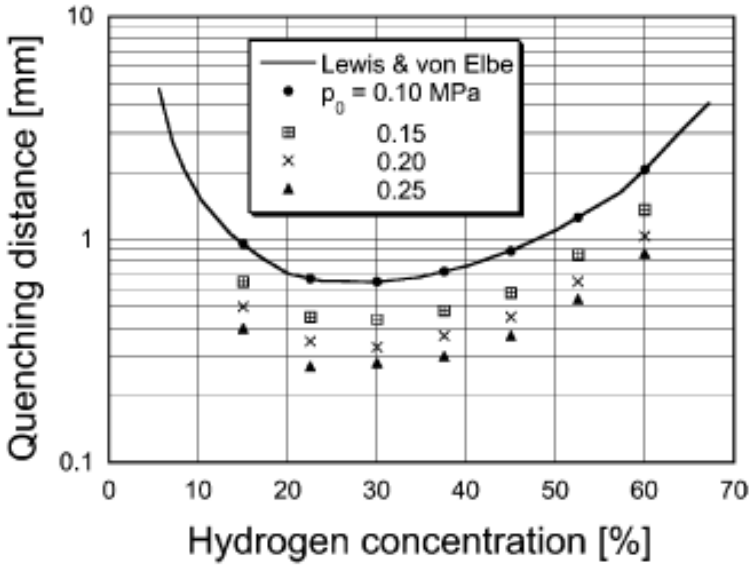


Figure 3.39: Quenching distance as a function of hydrogen concentration at various initial pressures (Yang et al., 2003).

(a) PVC hose bag (b) Flexible bag

Figure 3.40: Photographs of hydrogen gas bags.


Figure 3.41: Photograph of the hydraulic device used for pressure testing.

Figure 3.42: Housing for atmospheric blow-down device for fuel delivery.

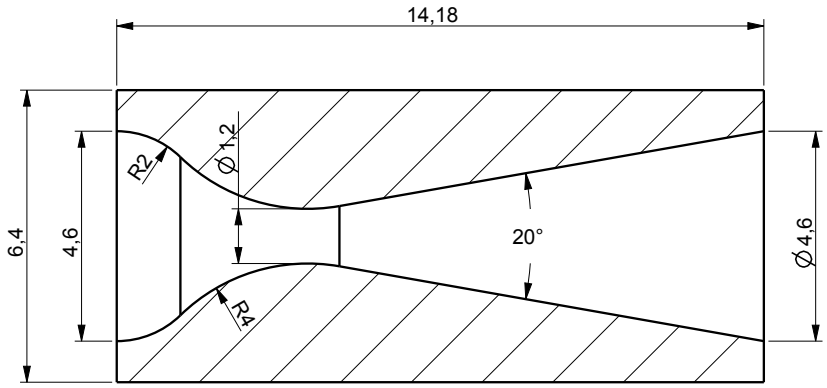


Figure 3.43: Sectional view of the mass-control nozzle with main dimensions.

### 3.4.2 Experiments and Analysis of the Fuel System

The presumed flow process within the fuel delivery system is that a subsonic flow coming from a gas reservoir is chocked at the MC nozzle followed a decelerating supersonic flow choking again at the slot injector exit when the nose-cone model is used. The investigation of the fuel delivery system was performed by combination of experimental testing and CFD numerical simulations using the Eilmer3 software (Jacobs et al., 2014). A detailed description of this CFD code as applied in this thesis is presented in Chapter 5.

Tests were performed in the atmospheric blow-down mode with an evacuated test section pressure of 1.0 kPa and using hydrogen injection with the nose-cone model for static surface pressure surveying. Because of the difficulty in placing measurement instruments at the injector exit due to geometrical restrictions, an alternative temperature and pressure measurement within the plenum upstream of injector was used. Thus, if measurements of conditions in the plenum can be demonstrated to be close to stagnation, the flow parameters of the jet injection can be derived from these conditions by isentropic flow relationships. The nose-cone model was adapted by replacing the cone-tip with a pressure measurement nipple connected with a Kulite sensor (XTL-190M-0.7BAR), as shown in Figure 3.44. The installation of a K-type fine wire thermocouple (OMEGA, Dia 0.001 inch) used for temperature measurement is also illustrated

in this figure. The experimental data was recorded with a frequency of 1 kHz.

The experimental results are listed in Table 3.8. Figure 3.45 presents the locations of pressure and temperature variables within the fuel flow path. The theoretical (adiabatic) flow parameters calculated by Eq. 3.17 and 3.18 are also presented in this Table.

Table 3.8: Summary of flow conditions at different locations.

| | **Experiment** | **CFD** | **Theoretical** |
|---|---|---|---|
| $P_1$ (kPa) | 94.43 | 94.43 | 94.43 |
| $T_1$ (K) | 287.8 | 287.8 | 287.8 |
| $P_2$ (kPa) | 7.08 | 7.44 | - |
| $T_2$ (K) | 284.9 | 294.6 | - |
| $P_e$ (kPa) | 3.68 | 3.17 | 3.39 |
| $T_e$ (K) | 242.0 | 239.3 | 239.8 |
| $\dot{m}$ (kg/s) | $4.52 \times 10^{-5}$ | $5.35 \times 10^{-5}$ | - |
| $\dot{m}_{th}$ (kg/s) | $5.56 \times 10^{-5}$ | - | - |
| $C$ | 0.81 | - | - |

The results of $P_e = 3.68$ kPa and $T_e = 242.0$ K are calculated from experimental measured $P_2 = 7.08$ kPa and $T_2 = 284.9$ K based on isentropic flow relationships.
$\dot{m}_{th}$ is the theoretical mass flow rate calculated based on the time-averaged measurement of $P_2$ and $T_2$ based on the annular area of the slot injector.
$C$ is the discharge coefficient for the slot injector.

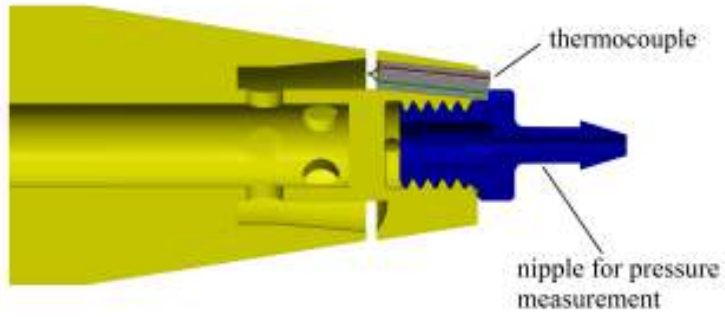


Figure 3.44: CAD views of pressure and temperature measurement arrangement within the plenum.

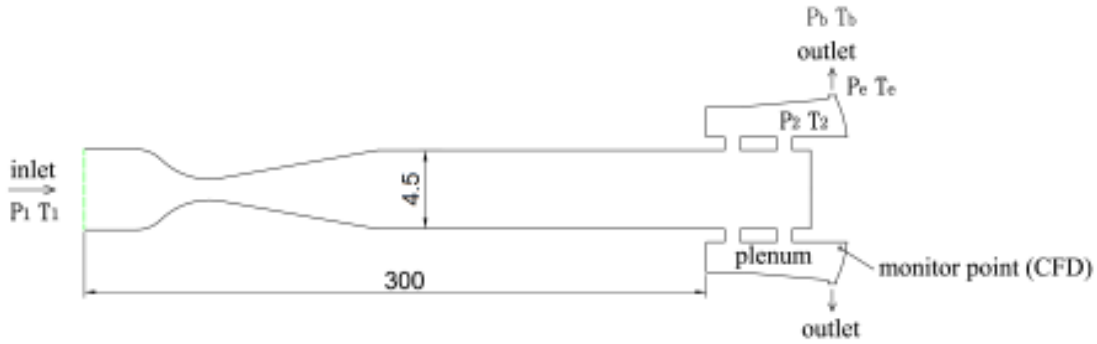


Figure 3.45: Schematic illustration of the internal flow path for hydrogen injection (dimensions in mm, not to scale).

Numerical simulation of the hydrogen delivery process was performed because it provides substantial insight into the prevailing flow mechanisms. The simulation was implemented using Eilmer3 software with an application of the $k-\omega$ turbulence model. The flow parameters at the inlet and outlet were set according to measurements listed in Table 3.8. The fixed temperature of 295 K was specified for the no-slip wall in accordance with the ambient temperature when the test was conducted. The computational domain consists of a 2-D axisymmetric geometry representing the dimensions of the hydrogen flow path starting from the MC nozzle as schematically illustrated in Figure 3.45. Noting that two annular flow paths were used in the simulation to represent the 8 portholes connecting the central circular flow path and the plenum, the total annular cross-section area was matched to that of the portholes. A monitoring point in the CFD was set to record the transient simulated history approximating the location of the pressure measurement in the experiment. The computational domain was divided into 80 sub-blocks and the simulation was run in parallel on USQs High Performance Computing (HPC) facility.

The simulated results for the Mach number in the front and rear segment of flow path is displayed in Figure 3.46. A Mach number of 3.6 in the nozzle exit flow was produced by the MC nozzle with the so-called shock diamond features. On average, the flow decelerates along the flow passage as expected. Figure 3.47 and Figure 3.48 illustrate a good agreement for the comparison of experimental results with CFD-simulated history of temperature and pressure at the monitoring point. The spatially-averaged Mach number across the injector exit is plotted in Figure 3.49; the dash line in this figure

represents the time-averaged result from this simulated Mach number and corresponds to a value of 0.99. The CFD results predict an unsteady flow within the injection flow path caused by the flow separation and standing waves formed downstream of the MC nozzle. However, the speculated sonic flow at the injector exit is reasonable because the time-spatially-averaged jet speed is close to sonic.

The averaged pressures and temperatures from the CFD-simulated results at the monitoring point and injector exit as well as the mass flow rate are included in Table 3.8. Comparison of experimental measurements and theoretical results and simulations in Table 3.8 suggests temperature, rather than pressure, is a more reliable parameter. Thus, the pressure of the jet flow can be calculated by

$$P_e = \frac{\dot{m}}{A^*}\sqrt{\frac{RT_e}{\gamma}} \tag{3.20}$$

where $\dot{m}$ is mass flow rate measured by the OMEGA mass flow meter, $A^* = A/C$ is the effective annular area of slot injector identified using the discharge coefficient $C = 0.81$, and $T_e$ is the temperature calculated from Eq. 3.17.

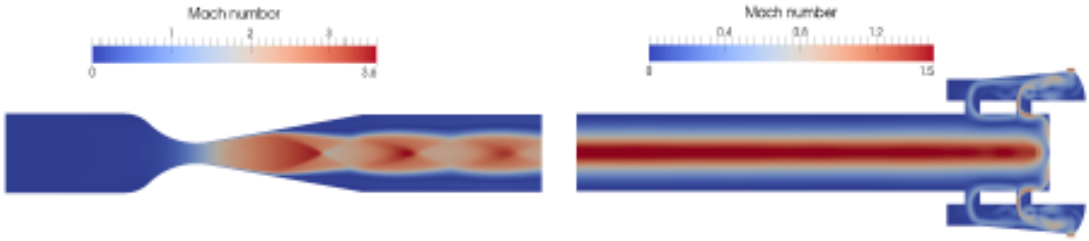


Figure 3.46: Map of CFD simulated Mach number; the front and rear segments are magnified for clarity.

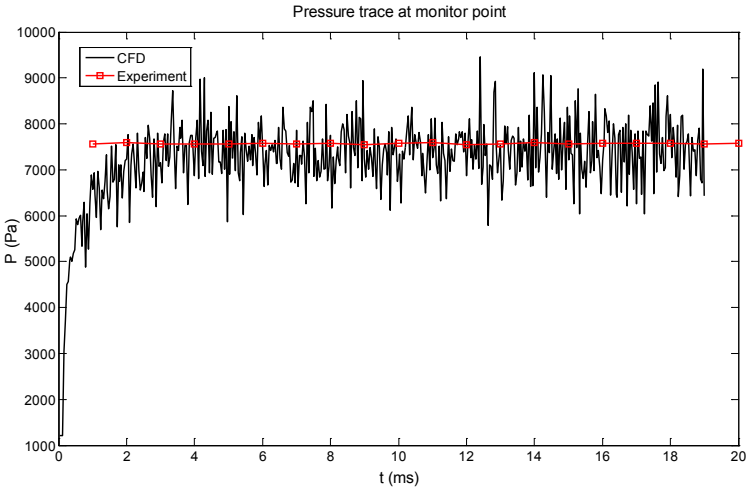


Figure 3.47: Comparison of measured pressures and CFD-simulated pressures at the monitor point.

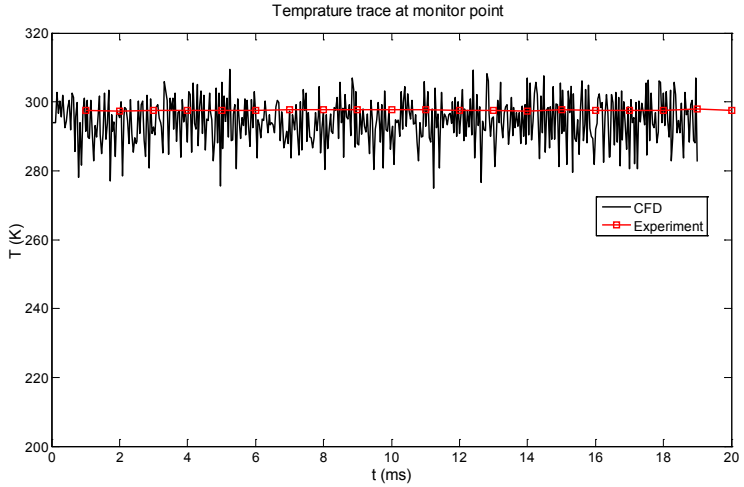


Figure 3.48: Comparison of measured temperatures and CFD-simulated temperatures at the monitor point.

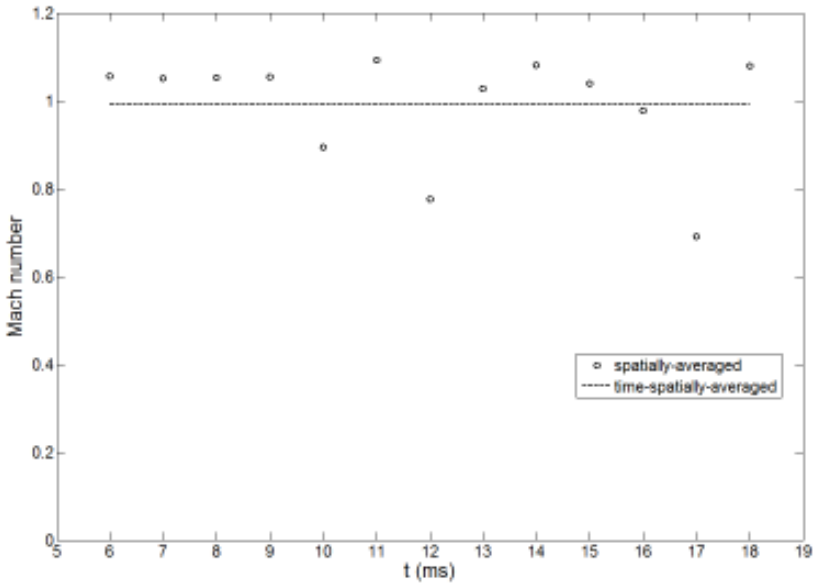


Figure 3.49: The CFD results for the spatially-averaged Mach number at the injector exit from simulation time of 6 ms to 18 ms.

## 3.5 Optical Diagnostics

Four optical techniques were applied in the experimental investigations in this thesis: (1) Two Colour Ratio Pyrometry (TCRP) for surface temperature measurement; (2) Visible/Near-Infrared (VnIR) spectrometry, also for surface temperature measurement; (3) high-speed schlieren imaging for flow visualization; and (4) an ICCD camera detecting excited OH (that is, OH*) chemiluminescence as a combustion diagnostic.

The merits of non-intrusive optical techniques over conventional measurement techniques lies not only in avoiding contact with the measured objects so that it can be applied to harsh environments, but also in excluding the interference caused by intrusive devices. Taking thermocouple measurements as an example, the thermocouple itself degrades in harsh environments and may also change the temperature of the material to which it is attached. The concept of the two temperature measurement methods are presented first to provide a generalized understanding of the methodology. A description of calibration and testing with these devices is then presented.

The imaging techniques based on high-speed schlieren and the ICCD camera were configured to observe a two-dimensional field of interest which can provide valuable insight into the flow structures and combustible reaction zone and greatly enhance the understanding in the flow behavior and the heat induced combustion processes near the surface.

### 3.5.1 Two Colour Ratio Pyrometry (TCRP)

The temperature of the heated model potentially has a critical impact on the combustion adjacent to the hot surface because it will influence the temperature of the flow within the boundary layer. In order to define the temperature conditions under which the combustion testing is taking place, reliable detection methods are necessary. If a commercial infrared camera is available the benefits would include spatial resolution of the hot surface, but the relatively low framing rate cannot fully resolve temperature variations during the test flow period. Two Colour Ratio Pyrometry (TCRP), with fast response times (10 kHz) was used to resolve the surface temperature evolution of the heated model for the present study. In addition to the TCRP, a Visible/Near-Infrared (VnIR) spectrometer was also used to acquire the radiation from the hot surface simultaneously and the temperature was deduced by fitting Planck radiation curves to the acquired spectrum. The main purpose of temperature measurement by the spectrometer configuration was to effectively provide an in-situ calibration for the fast-response TCRP measurement. The temporal resolution of the spectrometer itself is too low (5 Hz) to define the temperature variation of the hot model during the test flow duration. Details of the spectrometer system are presented in Section 3.5.2.

TCRP has been widely used for temperature measurement for combustion research in industrial furnaces and soot formation of internal combustion engine studies (Zhao and Ladommatos, 1998; Tago, Akimoto, Kitagawa, Arai, Churchill and Gupta, 2005; Godoy and Lockwood, 1998; Kuhn, Ma, Connelly, Smooke and Long, 2011; Levendis, Estrada and Hottel, 1992; Huang, Yan and Riley, 2000). It was adopted in a shock tunnel testing by Zander et al. (2012) for measuring a spatially resolved surface temperature of a hot carbon-carbon model. The TCRP method works on the principle that the ratio of any two wavelength intensities emitted by a grey body is unique to a particular

temperature. TCRP determines the temperature by measurement of the ratio of radiation emitted at two wavelengths, without knowledge of the absolute values of radiant intensity or the emissivity if the emitted radiation is grey over the wavelength interval. The operating wavelengths can be chosen arbitrarily as long as they are known and significant radiation can be received at these wavelengths for the temperature range of interest.

The monochromatic intensity $I(\lambda, T)$ of radiation emitted by a material at wavelength $\lambda$, is dependent on the material's emissivity $\epsilon(\lambda)$ and temperature $T$ according to Planck's law:

$$I(\lambda, T) = \epsilon(\lambda) E_{b,\lambda}(T) = \epsilon(\lambda) \frac{C_1}{\lambda^5 (e^{C_2/\lambda T} - 1)} \tag{3.21}$$

where $E_{b,\lambda}(T)$ is the intensity of monochromatic radiation from a blackbody, $C_1$ and $C_2$ are the radiation constants. In a practical experiment, the measured signal $S(\lambda, T)$ is a voltage directly proportional to the irradiance received by the detectors:

$$S(\lambda, T) = A(\lambda) I(\lambda, T) \tag{3.22}$$

where $A(\lambda)$ is a constant for the specified optical and geometrical configuration and the photodetector properties. The function $A(\lambda)$ incorporates modifications due to lens, optical fiber and filter transmittances, as well as the conversion factor from irradiance to signal voltage by the photodetector.

For two selected wavelengths, $\lambda_1$ and $\lambda_2$, the ratio of the signals is

$$\frac{S(\lambda_1, T)}{S(\lambda_2, T)} = \frac{A(\lambda_1) I(\lambda_1, T)}{A(\lambda_2) I(\lambda_2, T)} = \frac{A(\lambda_1) \epsilon(\lambda_1) E_{b,\lambda_1}(T)}{A(\lambda_2) \epsilon(\lambda_2) E_{b,\lambda_2}(T)} \tag{3.23}$$

Although graphite does not behave strictly as grey body, the investigation into the wavelength dependent emissivity of graphite has shown a maximum difference of 5% in the wavelength range of $500 \sim 1000\,\text{nm}$ (Neuer, 1992; Neuer and Jaroma-Weiland, 1998; Balat-Pichelin, Robert and Sans, 2006). The TCRP technique applied for this study

operates within the 500 $\sim$ 1000 nm range. Therefore, to a reasonable approximation, the Eq. 3.23 can be expressed with the grey body assumption as,

$$\frac{S(\lambda_1,T)}{S(\lambda_2,T)} = \frac{A(\lambda_1)I(\lambda_1,T)}{A(\lambda_2)I(\lambda_2,T)} = F_{(1,2)}\frac{E_{b,\lambda_1}(T)}{E_{b,\lambda_2}(T)} \tag{3.24}$$

where $F_{(1,2)} = A(\lambda_1)/A(\lambda_1)$ can be identified through calibration using a known monochromatic intensity radiance source at the two wavelength $\lambda_1$ and $\lambda_2$. The Labsphere CSTM-LR-2Z-4 luminance radiance source was used for the calibration as shown in Figure 3.50.

Figure 3.50: Integrating sphere used for calibration (on left) and an optical calibration tube (on right).

Figure 3.51: The set of Throlabs amplified photodetectors used in the TCRP.

Three narrow bandpass filters at wavelengths 600 nm (Thorlabs FB600-10), 700 nm (Thorlabs FB700-10) and 850 nm (Thorlabs FB800-10) were placed on the top of signal receiving window of the amplified photodetectors (Thorlabs PDA36A-EC) which have sensitivity within the wavelength range of 350 to 1100 nm. Figure 3.51 presents a photograph of the detectors. A schematic of the TCRP optical configuration is illustrated in Figure 3.52. Radiant light collected from the graphite by an uncoated bi-convex lens (f=50 mm) is transmitted through two bifurcated optical fiber bundles splitting the light signal into three bandpass filter and photodetectors. The output voltages converted via linear amplifiers from the detected light signatures were recorded by a Data Acquisition system at a frequency of 10 kHz. The optical collection tube was configured with an object distance of 150 mm approximately such that interference with the main hypersonic flow is avoided. Radiation from a circular spot with a di-

ameter of 3 mm approximately on the hot graphite surface was therefore collected and transmitted by the bundle of optical fibers to the filters and detectors.

The errors in the TCRP caused by ignoring the variation of 5 % in graphite emissivity for the three ratios: I(850nm)/I(700nm), I(850nm)/I(600nm) and I(700nm)/I(600nm) are estimated to be 60 K, 130 K and 140 K respectively over the temperature range of 1500 to 2000 K. Figure 3.53 shows the intensity ratios as functions of temperature for the selected three monochromatic wavelengths. Although the I(850nm)/I(600nm) ratio appears the most suitable for temperature deduction because of its relatively large ratio values relative to the other two wavelength ratios, the relatively low monochromatic radiation magnitude at 600 nm over the temperature range of interest may lead to large errors. In the practical TCRP operation in this work, the ratio of I(850nm)/I(700nm) exhibited the best performance and was chosen for temperature determination.

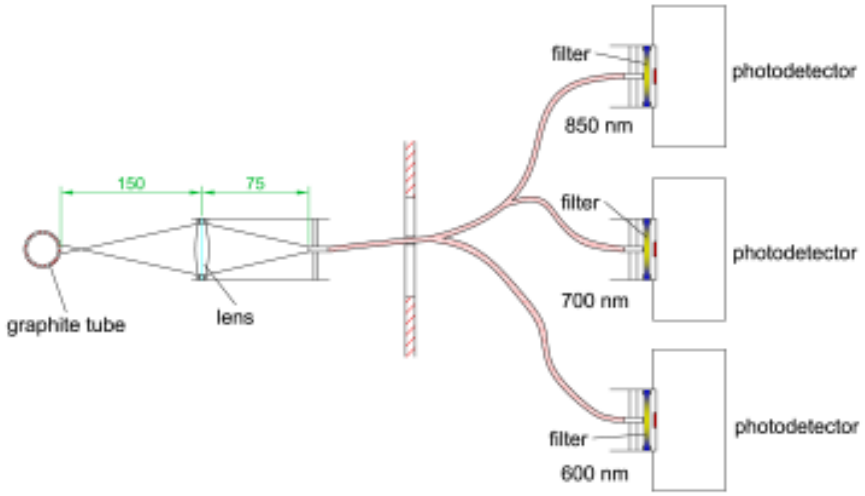


Figure 3.52: Schematic of the TCRP optical configuration.

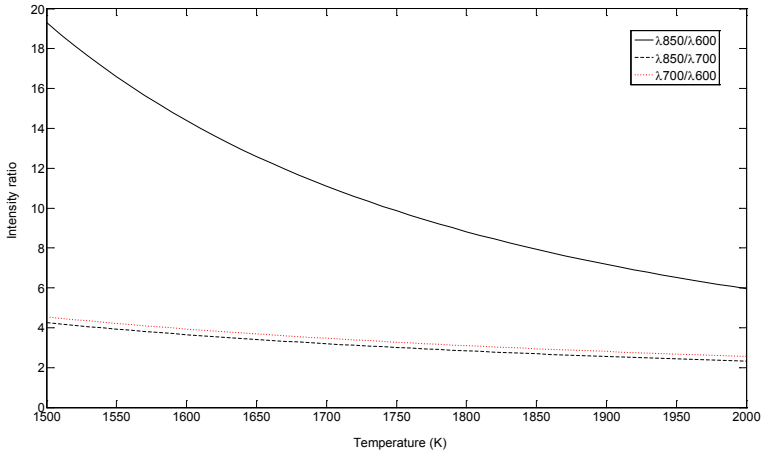


Figure 3.53: Intensity ratios for the three selected wavelengths: 600 nm, 700 nm and 850 nm.

### 3.5.2 Visible near Infrared (VnIR) Spectrometer

In addition to the TCRP method, the spectroscopic observation of the hot surface was recorded during hot model testing both with and without the external supersonic flow and the acquired signals were used to deduce the surface temperature. The purpose of this method was to provide an in-situ temperature calibration and reference for the fast-response TCRP measurement. This temperature measurement method was applied in TUSQ by Kraetzig for an investigation of heat flux measurement on hot models (Kraetzig et al., 2014).

The principle of temperature determination from VnIR spectroscopy is the fitting of Planck radiation curves to spectrum acquired from the hot graphite model. Again the graphite material is assumed to behave as a grey body. A VnIR instrument, the Thorlabs CCS175 pocket spectrometer, was driven by LabVIEW software for continuous spectrum acquisition during the model heating process. The spectrometer uses a $20\,\mu m \times 2\,mm$ entrance slit, a grating with 830 Lines/mm (800 nm Blaze), a detecting CCD chip with 3648 linear pixels (Toshiba TCD1304DG) and an electronic shutter function, shown in Figure 3.54. The spectral range specified by the manufacturer is stated as 496.92 nm to 1099.05 nm with a resolution of 6 px/nm.


Figure 3.54: Top view of the opened CCS175 Spectrometer (Kraetzig, 2013).

Figure 3.55: Mercury lamp (EYE, SB/RSP38).

The VnIR spectroscopy used the same configuration of the optical collecting tube as that of the TCRP, but a single optical fiber was used for coupling to the spectrometer. The spectrum data acquisition was triggered manually when the heating cycle started. The exposure time was adjusted in the range of 10 $\mu$s to 60 s by the LabVIEW software based on the internal counts with consideration of overexposure and the noise level.

It is not necessary to have an absolute intensity measurement, but the relative wavelength dependent intensity is critical for the temperature determination methodology that requires fitting a Planck curve to each acquired spectrum. The overall conversion factor $C_\lambda$ for the spectrometer and associated optical path was determined by comparing the measured spectrum to radiance data of the integrating sphere (Labsphere CSTM-LR-2Z-4). Thus the spectrum $S_\lambda$ with the corrected relative radiant intensities acquired from the assumed grey body surface can be calculated from the conversion factor $C_\lambda$ using

$$S_\lambda = \frac{S_{\lambda,aq}}{C_\lambda} = \epsilon \frac{C}{\lambda^5(e^{C_2/\lambda T} - 1)} \tag{3.25}$$

where $S_{\lambda,aq}$ is the acquired spectrum data from the spectrometer, $C$ is constant determined by conversion factor $C_\lambda$ and $C_2$ constant from Planck's law. The least-squares fitting of the Planck curve shape to each acquired $S_\lambda$ shape allows the determination the surface temperature evolution during a heating cycle.

A wavelength calibration of the CCS175 spectrometer was performed. A mercury vapor

lamp as shown in Figure 3.55 and two diode lasers with center wavelengths of 635 nm and 670 nm were utilized as calibration light sources. The emission spectra of the mercury vapor lamp was obtained from Bare and Demas (2000). Figure 3.56 illustrates the emission spectrum curves of the mercury lamp captured by the spectrometer and shows five obvious emission lines (denoted with letters A to E) which are chosen for calibration. The identified wavelengths and the corresponding pixels of the spectrometer are listed in Table 3.9. The calibrated spectral range of CCS175 spectrometer is identified as 490.86 nm to 1097.13 nm with a resolution of 6.0154 px/nm.

Table 3.9: Wavelength-pixels calibration of CCS175 spectrometer.

| | **Mercury vapor lamp** | | | | | **Laser** | |
|---|---|---|---|---|---|---|---|
| **wavelength (nm)** | 546.07 | 576.96 | 579.07 | 625.14 | 1092.14 | 635 | 670 |
| **pixels** | 320 | 515 | 528 | 785 | 3611 | 890 | 1108 |

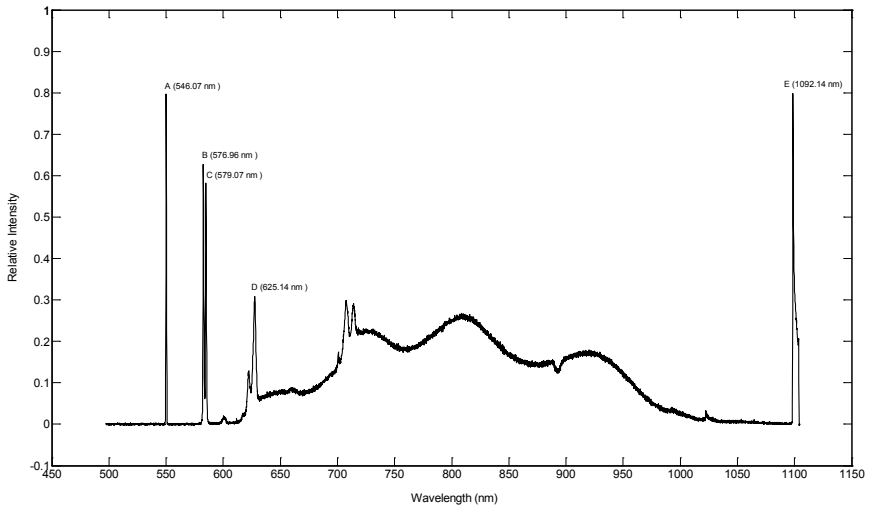


Figure 3.56: Emission profiles of the Mercury lamp (EYE, SB/RSP38) acquired by the CCS175 spectrometer.

### 3.5.3 Validation Test of Temperature Measurement

A heating test was performed to validate the temperature measurement methods of the TCRP and the VnIR spectrometer. The data acquisition system was triggered

simultaneously when the power supply delivering current to the model was switched on. The TCRP signals were recorded for 20 s at a frequency of 1 kHz while the varying integration time of the spectrometer was manipulated by LabVIEW software depending on the detected intensity of received signals transmitted from the hot surface. The data acquisition frequency of the spectrometer during the heating cycle is illustrated in Figure 3.57. The relative long integration times required for the present optical arrangement and operating condition results in a data acquisition frequency that is adequate for the overall heating cycle but is not sufficient for time-resolved temperature measurement during the hypersonic flow.

The measured spectra at four different times during the heating cycle are extracted and presented in Figure 3.58, which also shows the Planck curve fitting based on a temperature at the specified times. A discrepancy between measured spectra and the Planck curves is exhibited for wavelengths below 780 nm. It is unclear whether this arises due to a defect in the spectrometer arrangement, the calibrating process using the integrating sphere, or the non-uniformity of graphite emissivity. The spectral data between wavelengths of 800 and 950 nm which includes 900 pixels approximately is selected for Planck curve fitting.

Figure 3.59 illustrates the comparison of temperature evolution measured by the TCRP and the spectrometer. The result of TCRP with the ratio I(850nm)/I(700nm) has a good agreement with the result of the spectrometer particularly when the temperature exceeds 1500 K. The temperatures deduced from the ratio of I(850nm)/I(600nm) and I(700nm)/I(600nm) are over-predicted at lower temperatures, in comparison to the results from the spectrometer. The inaccurate temperature deduction of the TCRP with I(850nm)/I(600nm) and I(700nm)/I(600nm) might be caused by a low SNR arising from the weak radiant intensity at the wavelength of 600 nm as discussed in Section 3.5.1.

The temperature determination by least-squares fitting of Planck curves to measured spectra has a potential for higher accuracy than TCRP because it is less sensitive to errors at particular wavelengths relative to the TCRP.

For the practical operation of electrical heating during the combustion testing, the wind tunnel is triggered to fire when the model is heated up to the target temperature and

the current should be cut off immediately once the hypersonic flow is terminated. The TCRP based on I(850nm)/I(700nm) is selected for model temperature measurement with a recording frequency of 10 kHz. The spectrometer is employed as a supplementary monitor for the temperature evolution of the whole heating cycle.

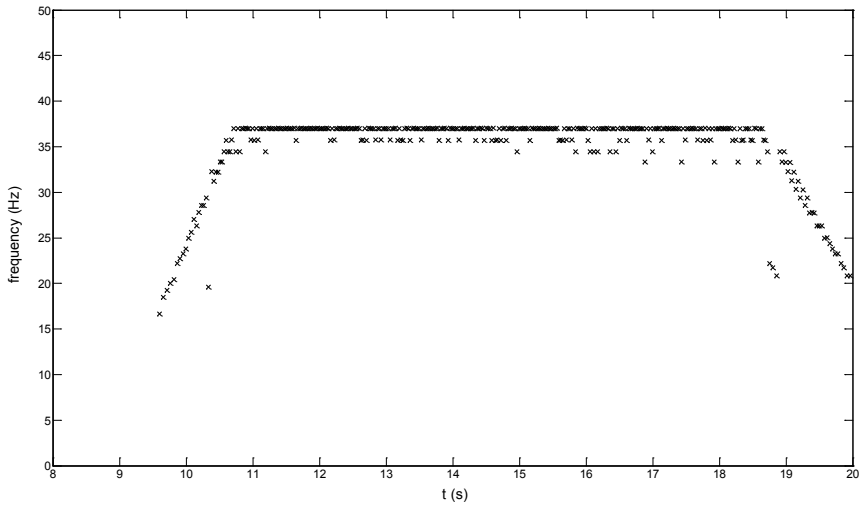


Figure 3.57: The data acquisition frequency of the CCS175 spectrometer during the heating test.

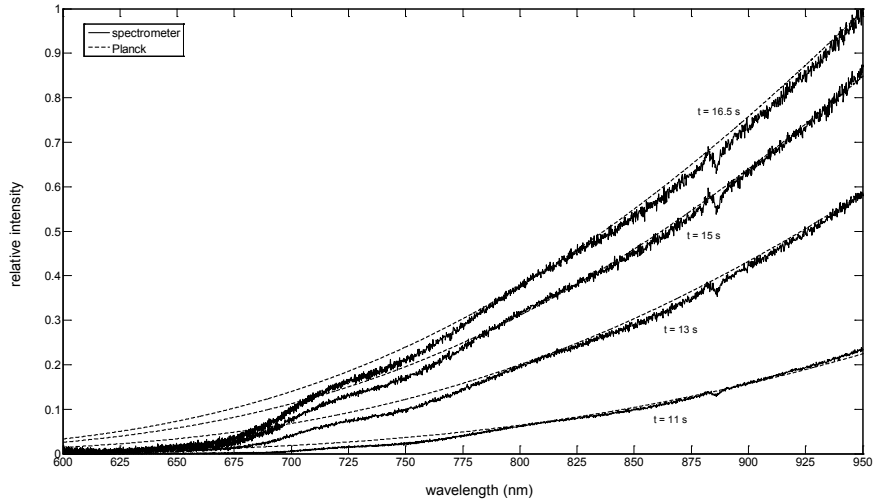


Figure 3.58: Spectra acquired from the heated graphite model by the CCS175 spectrometer with fitted Planck curves at recording times of 11, 13, 15, and 16.5 s.

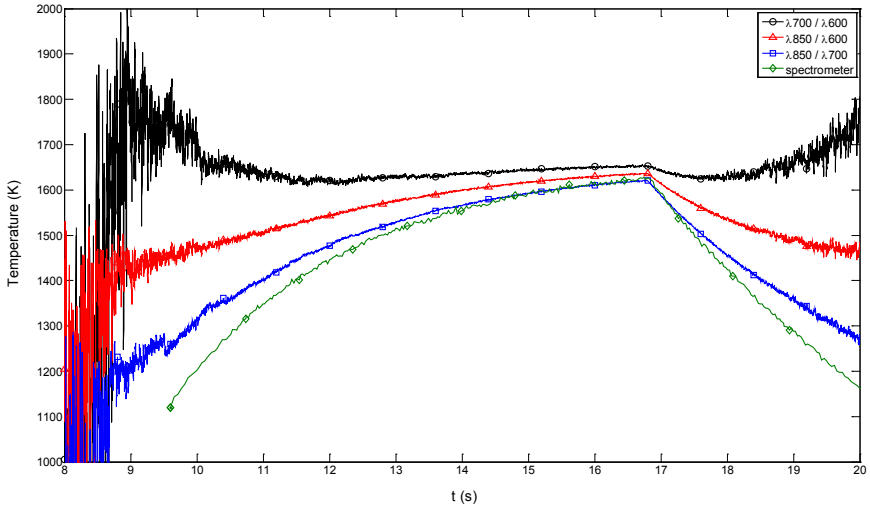


Figure 3.59: Comparison of temperature measurement by the TCRP and fitting the Planck curve to spectra from the CCS175 spectrometer.

### 3.5.4 High-speed Schlieren Imaging

The schlieren, shadowgraphic and interferometric techniques have been widely used for the flow visualision in transparent fluid. These method are based on the refractive index variations with changing density. The refractive index of a medium $n$ is related to its density by the GladstoneDale relation,

$$n = k\rho + 1 \tag{3.26}$$

where $\rho$ is the density and $k$ is the Gladstone-Dale constant of the medium under consideration.

The schlieren visualization technique which responds to the refractive index gradient corresponding to the first derivative of density was employed for this work. The schematic arrangement of a Herschellian Z-type schlieren system is shown in Figure 3.60, using two oppositely-tilted, on-axis telescopic parabolas.

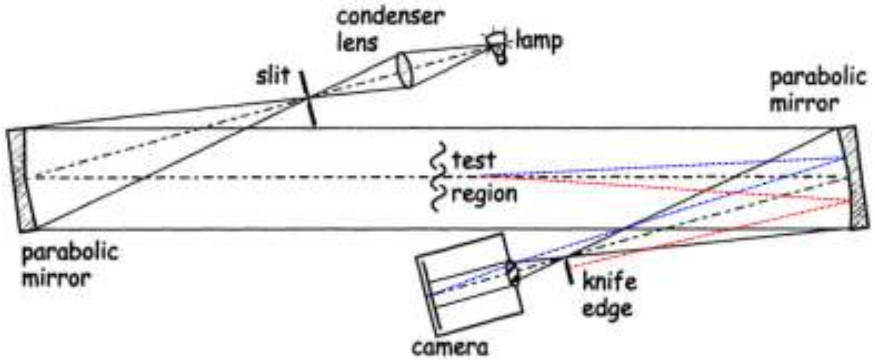


Figure 3.60: Schematic illustration of a Z-type schlieren arrangement, red and blue lines show the refracted light rays while the red is blocked by the knife edge (Settles, 2012).

The Z-type schlieren is the most commonly used system for studying high-speed flows in wind tunnels. It requires a collimated light source passing through the test region where the refractive index changes. In a supersonic flow, the pressure of shock and expansion waves affects the optical density of the flow. Schlieren visualization is thus a method that makes visible the changes in density across shock waves and expansion fans, depending on the system sensitivity. The straight light rays are bent away from their original path due to the density gradients in the test region. A knife-edge located at the focal plane of the second parabolic mirror is used to block off part of deflected light (as shown in the bent red downward dash line in Figure 3.60) causing reduced illumination intensity on the imaging plane. Meanwhile the refracted light (denoted in the blue dash line in Figure 3.60) is that is bent upward corresponding to the reversed density gradient, brightens a point on the focused imaging plane against the background. Thus the photograph taken at the imaging plane displays features that directly represent the line-of-sight integrated effect of density gradients along the light path.

The layout of schlieren visualization system setup operating with a high-speed camera in the TUSQ facility is illustrated in Figure 3.61. The high-speed camera (Photron SA3) is used to image and to record the schlieren-visualized flow fields, as shown in Figure 3.62. The normally-used continuous or pulsed light source is provided by a LED illuminator (HARDsoft IL-105/6X) as shown in Figure 3.63. The light source is first collimated by a parabolic mirror producing a parallel light beam passing through the test section and then it is refocused onto the knife-edge.

The LED light source is not applicable for hot surface model tests because the light from the LED is overwhelmed by the much stronger illumination from heated graphite. Five bundled laser diodes (Panasonic, LNCQ28PS01WW) with a wavelength of 661 nm replace the LED illuminator as the light source for schlieren visualization when hot surface model tests are performed, as shown in Figure 3.63. A narrow bandpass filter at the wavelength of 660 nm (Throlabs FB660-10) is placed behind the knife edge preventing most of the radiation emitted from the hot model to enter the high-speed camera.

The supersonic flow field produced by an axisymmetrical model with the horizontal knife-edge is shown in Figure 3.64. It is evident that the characteristics of scheliren image is represented by the dark and brightness regions corresponding to the density gradient within the axisymmetric features of the flow field.

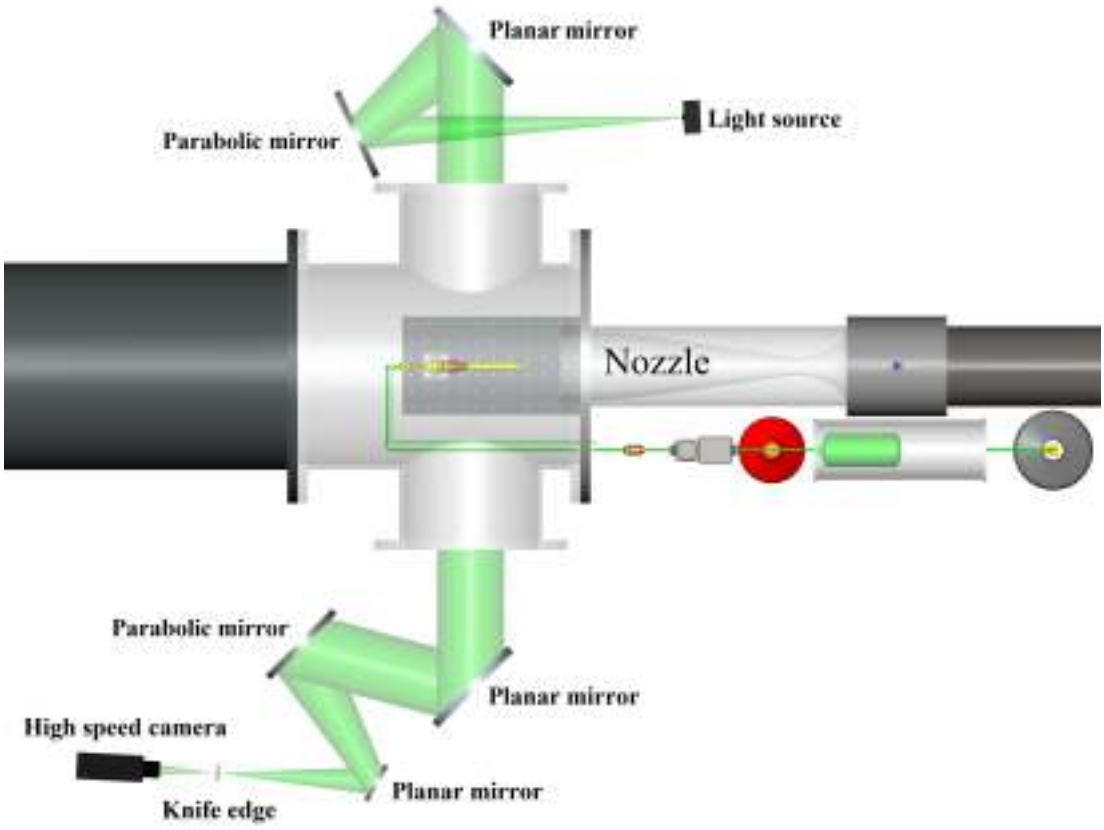


Figure 3.61: CAD views of the high-speed schlieren system setup in TUSQ.

Figure 3.62: Photograph of high speed camera (Photron SA3).

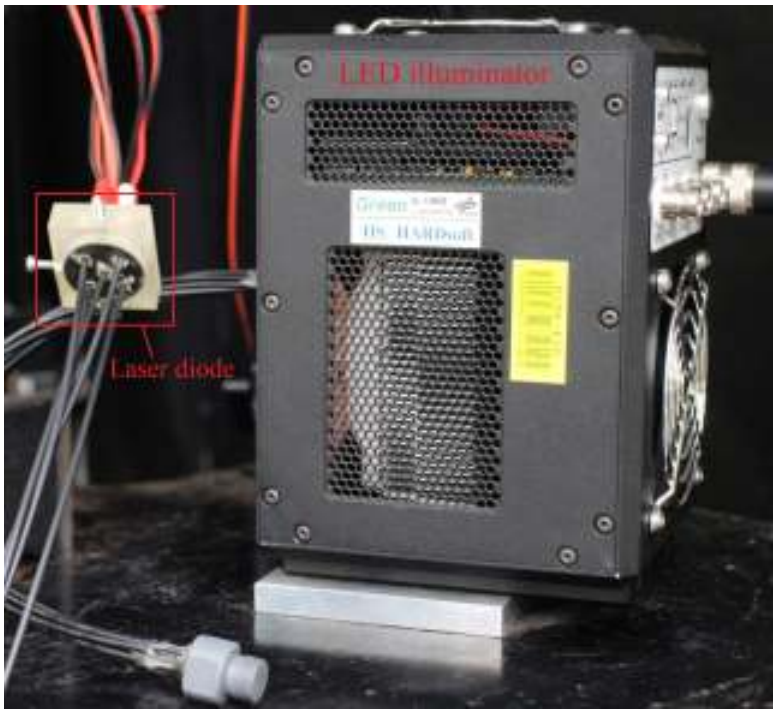


Figure 3.63: Photograph of light sources: LED illuminator and laser diodes bundle.

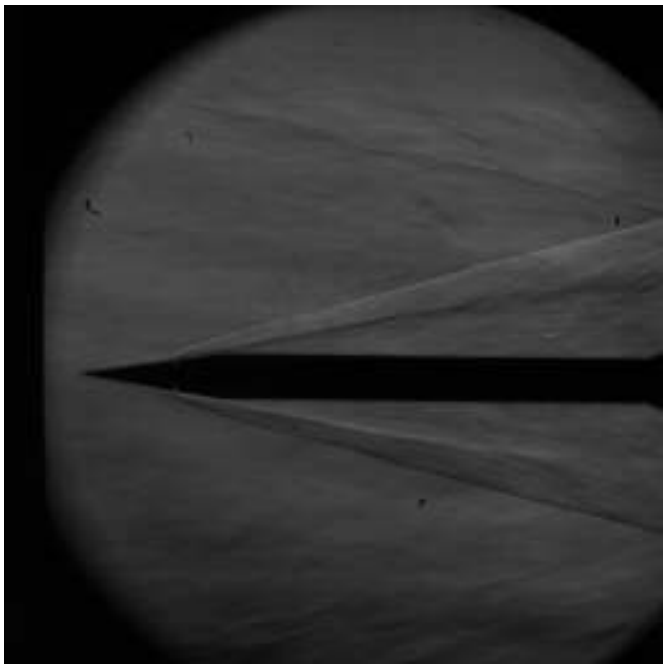

Figure 3.64: A horizontal knife-edge schlieren image extracted from the high speed camera footage using the nose-cone model in the Mach 6 flow.

### 3.5.5 OH* Chemiluminescence Imaging

Chemiluminescence measurements require no complex setups as the detected radiation is brought about by chemical reactions and is recorded directly using a Princeton Instruments PI-MAX intensified CCD (ICCD) camera equipped with an apochromatic, 105 mm focal length UV lens (Coastal Optical 105mm f/4 UV-Macro-Apo). A narrow-band-pass filter centered at 310 nm with 10 nm FWHM (ASAHI SPECTRA XBPA310) was assembled in front of the lens to exclusively capture the radiation emitted in the wavelength range of interest around 308 nm. The resolution of CCD array used in the camera is 1024px × 256px with each pixel being $26\,\mu m \times 26\,\mu m$ in size. The camera was mounted above the test section on a base which allows for vertical and horizontal adjustments of the camera position, as shown in Figure 3.65. The $CaF_2$ window on the top side of the test section provided transmittance for acquisition of the OH* chemiluminescence. The ICCD camera was placed with the object distance of 800 mm approximately on the centerline of the observation window as shown in Figure 3.66.

For the combustion testing in this study, the line-of-sight integrated ultraviolet signals

of chemiluminescence emission from OH* molecules were recorded in a two-dimensional plane. The intensity maps from this measurement can be used as a qualitative indicator for chemical self-luminosity of the hydroxyl radicals but the method is limited in providing detailed information for three-dimensional flow fields. The results from the chemiluminescence measurements and further data analysis with the Abel inversion and absolute concentration calculations are reported in Section 4.2.


Figure 3.65: ICCD camera setup for OH* chemiluminescence measurement.

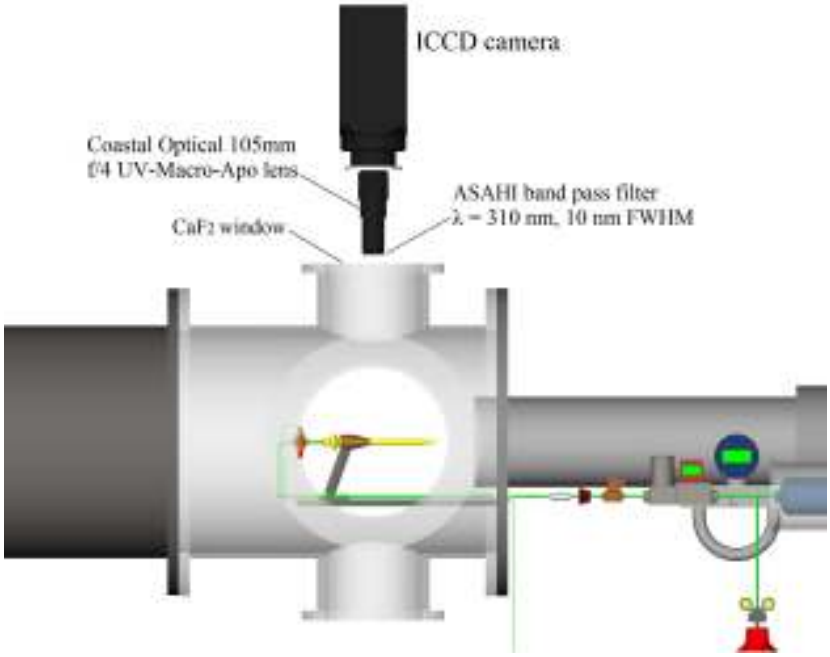


Figure 3.66: CAD views of ICCD camera installation.

# Chapter 4

# Experimental Results

This chapter describes the experimental results obtained in a set of tests performed in TUSQ using the Mach 2, Mach 2 and Mach 6 nozzles. The models and instruments used in this experimental study are described in Chapter 3. The slot injector of the nose-cone model was configured with a width of 0.5 mm for the current experimental campaigns. The static pressure surveys provide some information on the prevailing external flow fields in the heat induced combustion tests.

The combustion tests were performed using pure hydrogen fuel or premixed hydrogen-air fuel under a wide range of TUSQ and jet flow conditions. Prior to the combustion tests, the sensitivity of the ICCD camera was calibrated. The method for deduction of the axial temperature distribution and, the effect of the hot model on the jet flow is discussed. The combustion experiments in a nominally quiescent test section environment were performed for apparatus proof-testing. The Abel inversion method was implemented in the experimental data post processing. A method of determining the absolute number density of radiating excited-state radicals is proposed based on the Abel inverted-results.

## 4.1 Static Pressure Measurements

The local static pressure is one of important factors that affects the ignition process of a fuel-air mixture. The objective of the static pressure measurements is to provide information for the combustion testing and analysis. The pressure measurements can also offer some data to validate the CFD simulations. The pressure measurements with and without injection were performed and the contrast between them can be used to evaluate the effect of the jet flow on the static pressure distributions. The testing conditions for the pressure measurement experiments are summarized in Table 4.1, in which some other pertinent parameters are also presented. The pressure of the test section was set below 1 kPa for all pressure measuring tests. The Schlieren imaging technology was also used during the testing and the image frames are illustrated along with the pressure measurement results.

Table 4.1: Experimental conditions for static pressure measurements.

| Test NO. | Jet flow | | | | | Nozzle flow | |
|---|---|---|---|---|---|---|---|
| | $\dot{m}$ kg/s | $u_e$ m/s | $P_e$ kPa | $T_e$ K | $J$ | $P_0$ kPa | $T_0$ K |
| | Mach 2 Nozzle | | | | | | |
| run 370 | $4.29\times10^{-4}$ | 1206 | 23.7 | 252 | 0.21 | 225 | 584 |
| run 371 | - | - | - | - | - | 227 | 577 |
| | Mach 4 Nozzle | | | | | | |
| run 431 | $4.47\times10^{-5}$ | 198 | 2 | 296 | $4.5\times10^{-4}$ | 980 | 577 |
| run 432 | $1.05\times10^{-4}$ | 468 | 2 | 297 | $2.5\times10^{-3}$ | 970 | 579 |
| run 433 | - | - | - | - | - | 960 | 578 |
| | Mach 6 Nozzle | | | | | | |
| run 342 | $4.55\times10^{-5}$ | 1180 | 2.46 | 241 | 0.11 | 976 | 568 |
| run 366 | - | - | - | - | - | 1912 | 572 |

$P_0$ is the total pressure of nozzle exit flow

Static pressure measurements for the nose-cone and step-cone models were performed in the Mach 2, Mach 4 and Mach 6 flows using Kulite pressure transducers which were factory-new when employed for this study. So the manufacturer-sated 0.1% non-linearity at full scale was used in the error analysis. A two-point calibration method was

employed for the pressure transducers and amplifiers: the pressure of the evacuated test section prior to a run and the atmospheric pressure were used as the reference pressures. These two calibrating pressures were acquired by mercury gages resulting in the typical readings of $0.8\,\text{kPa} \pm 0.07\,\text{kPa}$ and $95\,\text{kPa} \pm 0.01\,\text{kPa}$ respectively during testing. An additional uncertainty of $\pm 3\%$ has been applied to accommodate variabilities in electrical cabling and cavity response effects. The error bars shown in the time-averaged pressure distribution figures represent a uncertainty of $\pm 8\%$ which represents a sum of the above effects.

### 4.1.1 Mach 2 Flow Tests - Nose-cone Configuration

Two tests with and without hydrogen injection were performed in the Mach 2 flow. The positions of model relative to nozzle exit are illustrated in Figure 4.1, which also presents the theoretically estimated core flow regions and the locations of the surface pressure measurement. The model was moved toward the nozzle in run 371 in order to increase the length of the model within the core flow. The model position in run 371 is same as that of the combustion tests.

Figure 4.2 shows the time-resolved pressure measurements and the static pressures normalized with the Mach 2 flow total pressure. The variation of measured static pressures during the nominally steady flow period arises due to the unsteady waves associated with the diaphragm-opening and piston oscillations. The averaged static pressures and the normalized pressures during the testing flow are plotted in Figure 4.3. It is noticeable that the pressure drops dramatically at locations downstream outside of the core flow regions. The hydrogen jet flows along the model surface, suppressed by the Mach 2 air flow because of the low momentum flux ratio ($J = 0.21$) as illustrated in Figure 4.1a.

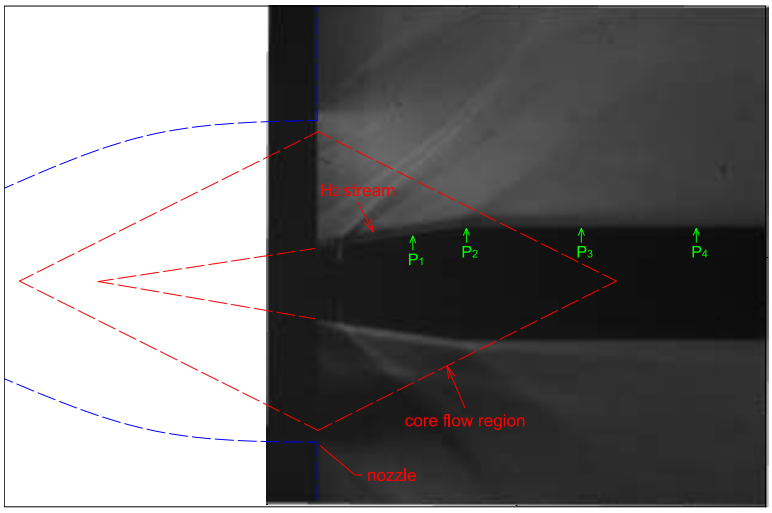


(a) Schlieren image of run 370

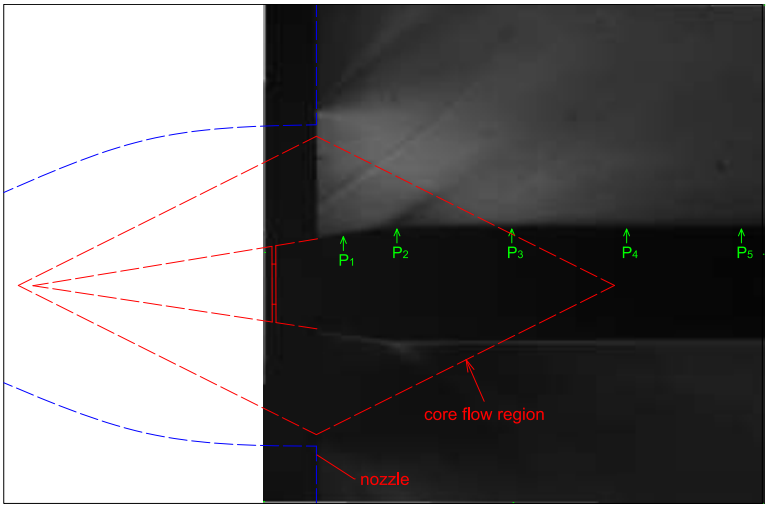


(b) Schlieren image of run 371

Figure 4.1: Schlieren images from the pressure measurement tests in the Mach 2 flow. 'P' indicates the positions of the pressure measurements.

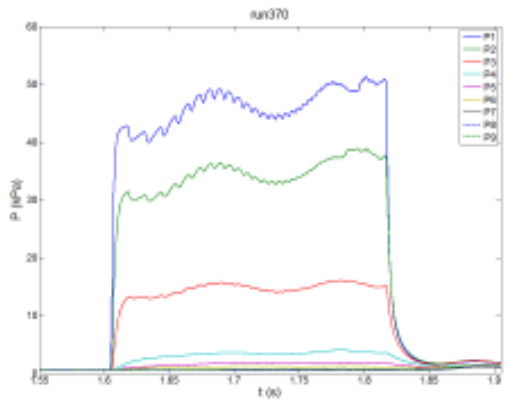


(a) Time-resolved static pressure meaurements of run 370

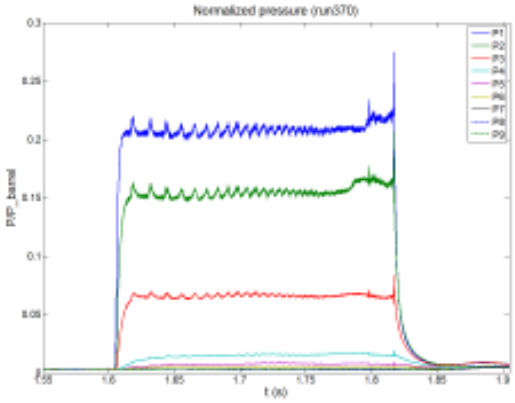


(b) Static pressure normalized with total pressure of the test flow of run 370

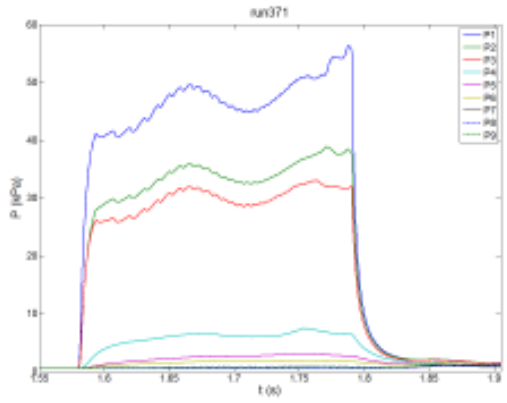


(c) Time-resolved static pressure meaurements of run 371

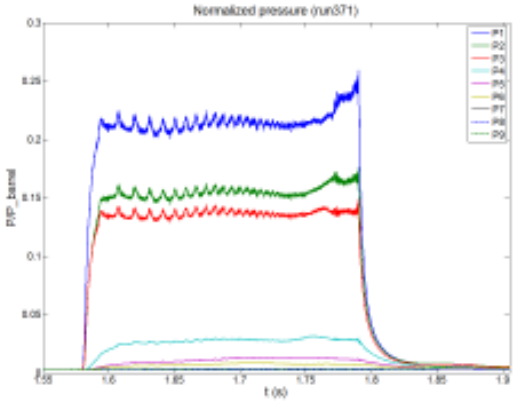


(d) Static pressure normalized with total pressure of the test flow of run 371

Figure 4.2: The time-resolved pressure measurements in the Mach 2 flow.

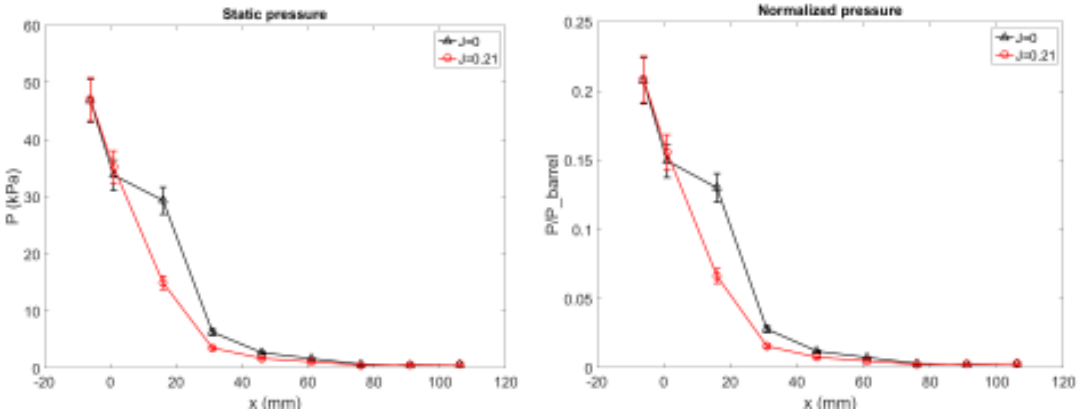


(a) Static pressure distribution (b) Normalized static pressure distribution

Figure 4.3: Static pressure distribution on the nose-cone model in the Mach 2 flow time-averaged over a nominally steady test flow period from t = 50 ms to t = 100 ms.

### 4.1.2 Mach 4 Flow Tests - Step-cone Configuration

The problem of supersonic or hypersonic flow over a backward-facing step has been investigated experimentally and numerically by many researchers (Roshko and Thomke, 1966; Korkegi and Shang, 1968; Dwoyer et al., 1971; Loth et al., 1992; Halupovich et al., 1999). The flow is characterized by a large local expansion around the corner, which dominates the downstream separated region as shown in Figure 4.4. A key feature of the flow is found to be the splitting of the shear layer at reattachment, where part of the flow is deflected upstream into the recirculating flow region while other part continues to flow downstream. The reattachment point, where the flow reversal occurs was measured by Roshko and Thomke (1966) using an axisymmetric downstream-facing step in supersonic flow. The experimental results revealed a nearly fixed reattachment point at the dimensionless distance $x/h = 3$ and a monotonically increasing pressure distribution within the recirculation zone.

The recirculation zone may assist the ignition process because the residence time of fuel mixture is increased whereas the relatively low pressure within this region has a negative affection. Measurements of static surface pressure using the step-cone model were carried out in the Mach 4 nozzle flow. The experimental conditions are listed in Table 4.1. The jet-to-free-stream momentum flux ratio $J$ is still presented to quantify

the jet flow but it should be noted that the $J$ value here does not relate to injection penetration in transverse jet injection. The positions of pressure measurements are indicated in Figure 4.5 which are frames extracted from the Schileren imaging during the testing. The positions of the model relative to Mach 4 nozzle can also be identified from these Schileren images.

The reattachment point of the baseline test without injection is estimated to be 21 mm approximately according to the Roshko and Thomke (1966) results. The typical flow structures described previously of a supersonic flow over a backward-facing step can be found in the Schileren images of Figure 4.5. A noteworthy feature is the elongated recirculation zone when hydrogen is injected. The injected flow reduces the strength of the reattachment shock and pushes it downstream.

The time-resolved pressure measurements and the static pressures normalized with total pressure of the mach 4 flow are plotted in Figure 4.6. The evident variation in the time-resolved pressure measurements arises due to TUSQ operation as discussed in the previous section. It can be observed from Figure 4.7 that the pressures rises monotonically and overshoots in the reattachment region for three different jet flow conditions. The magnitude of the static pressure is slightly elevated within the recirculation zone due to the presence of the injected flow.

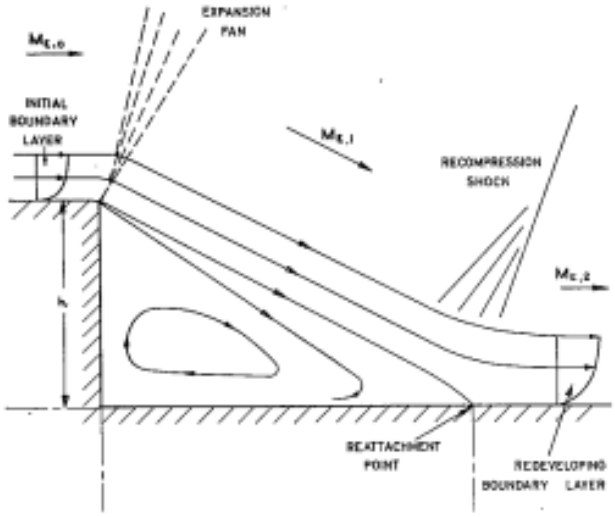


Figure 4.4: Schematic of supersonic flow over a backward-facing step (Roberts, 1966).

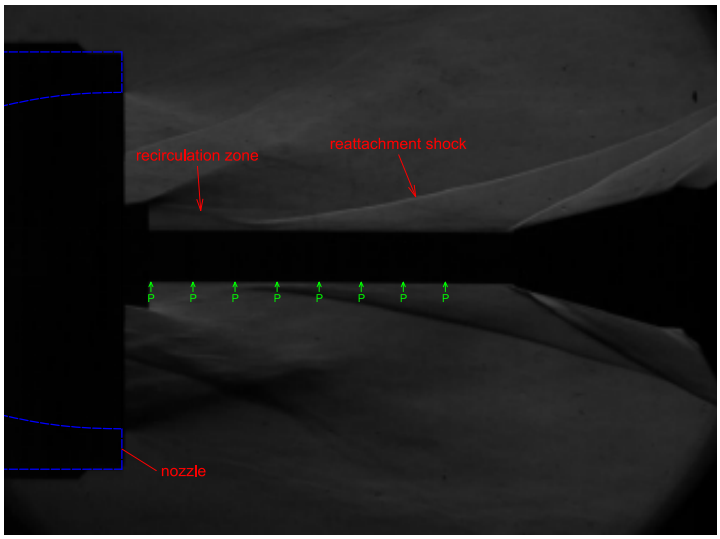


(a) Schlieren image of run 433

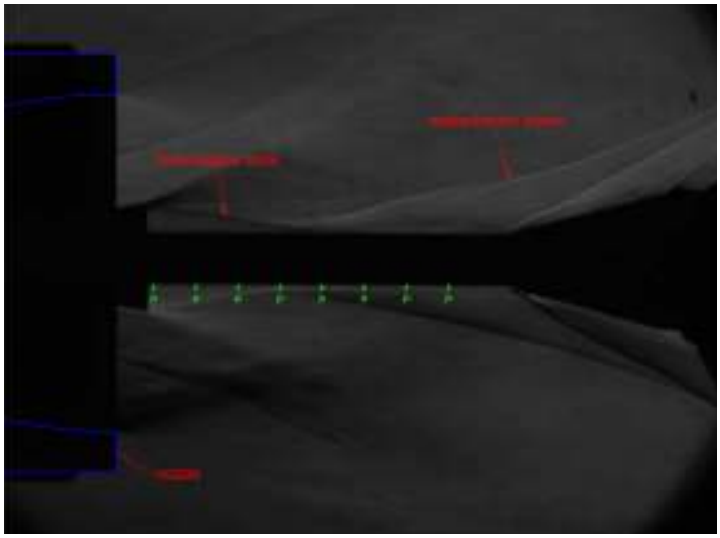

(b) Schlieren image of run 431

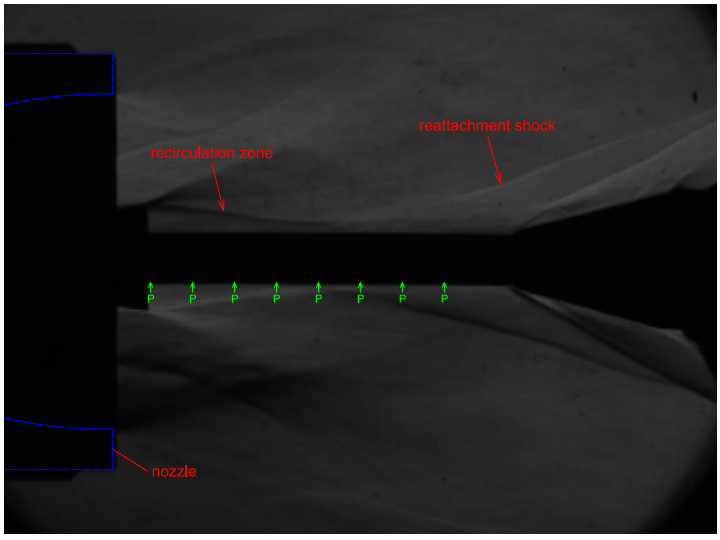


(c) Schlieren image of run 432

Figure 4.5: Schlieren images from the pressure measurement tests in the Mach 4 flow. 'P' indicates the positions of the pressure measurements.

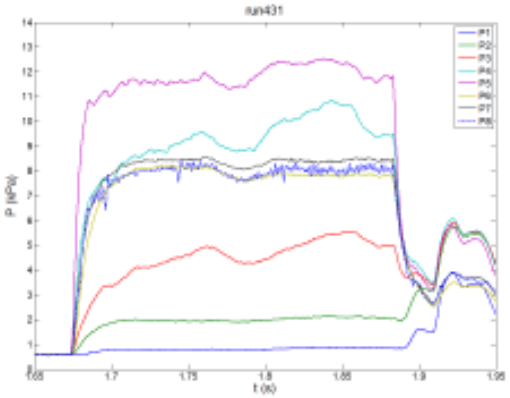


(a) Time-resolved static pressure meaurements of run 431

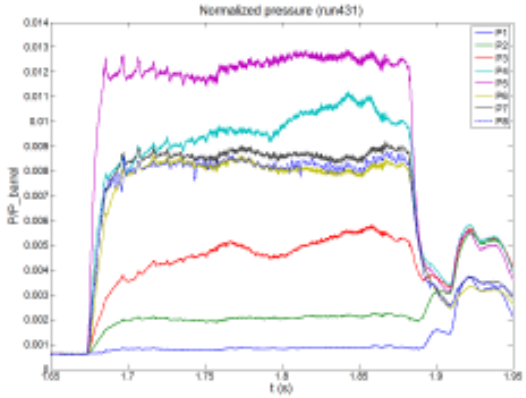


(b) Static pressure normalized with total pressure of the test flow of run 431

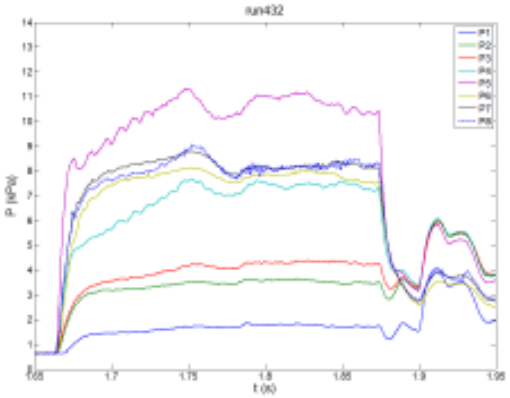


(c) Time-resolved static pressure meaurements of run 432

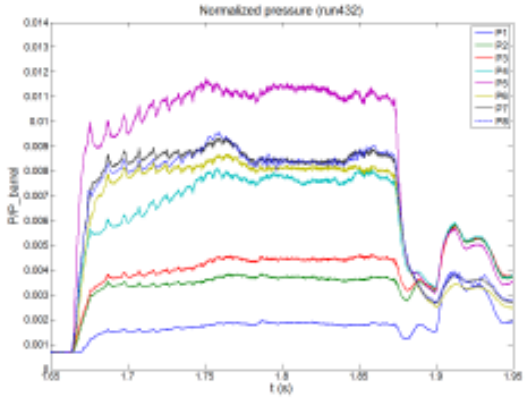


(d) Static pressure normalized with total pressure of the test flow of run 432

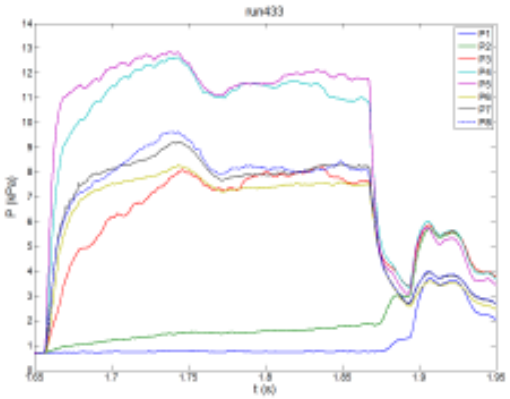


(e) Time-resolved static pressure meaurements of run 433

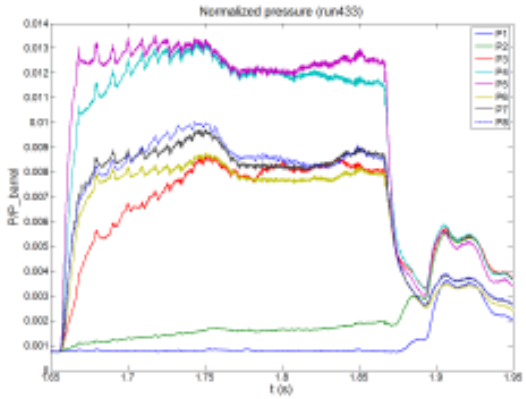


(f) Static pressure normalized with total pressure of the test flow of run 433

Figure 4.6: The time-resolved pressure measurements in the Mach 4 flow.

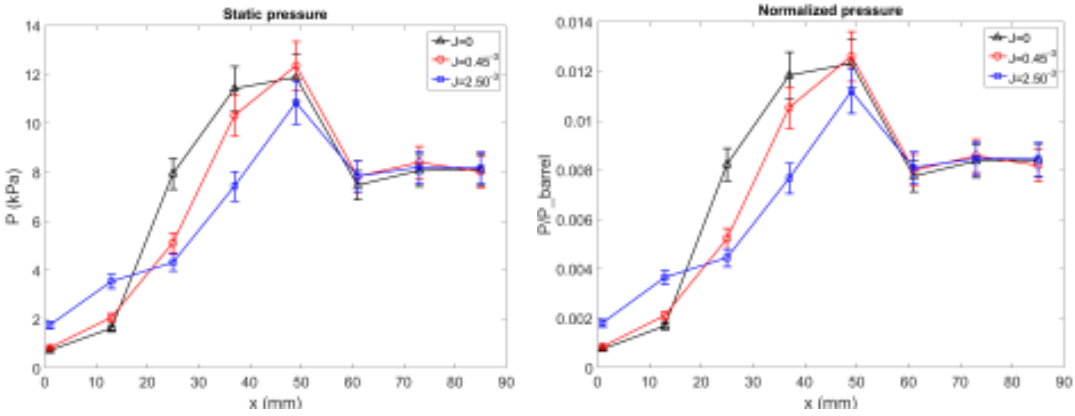


(a) Static pressure distribution (b) Normalized static pressure distribution

Figure 4.7: Static pressure distribution on the step-cone model in the Mach 4 flow time-averaged over a nominally steady test flow period from t = 100 ms to t = 150 ms.

### 4.1.3 Mach 6 Flow Tests - Nose-cone Configuration

The locations of pressure measurements on the nose-cone model in the Mach 6 flow are depicted in the Schlieren images presented in Figure 4.8a and 4.8b. Diaphragms with different thickness were used for these two tests and the Mach 6 flow total pressures are listed in Table 4.1. Figure 4.9 illustrates the evolution of measured pressure and the pressure normalized with the Mach 6 flow total pressure. The measurements indicate that there is a pronounced difference between the pressure measured on the cone surface behind the bow shock and on the cylindrical surface. It is noticeable that the jet flow has a significant influence on the static pressure which diminishes this difference, compare Figure 4.9a and 4.9c .

The jet flow induced a turbulent flow as can be observed clearly at regions near the surface in Figure 4.8b, while it is evident that a stable boundary layer was formed in the case without hydrogen injection, see Figure 4.8a. The conical shock angle increased from 28.2° to 32.8° due to the displacement effect from the jet flow as measured in the schlieren images Figure 4.8a and 4.8b at a flow time of 10 ms.

A pronounced increase of static pressure measured in the case of run 342 is observed at the flow time of 100 ms, see Figure 4.9c. This rapid pressure increase can be explained

with reference to the flow structures observed in the schlieren images at flow times of 10 ms, 120 ms and 180 ms as presented in Figure 4.8b, 4.8c and 4.8d. A shock wave labeled 'back-pressure shock' is formed due to the pressure of the test section which increases with time due to the delivery of the testing air into it. The back-pressure shock becomes stronger with time and impinges on the cylinder support structures, causing boundary layer separation which propagates upstream and causes the elevated static surface pressure.

The pressure distributions shown in Figure 4.10 indicate that the pressure on the cylindrical surface is increased by the hydrogen jet injection, but is reduced on the cone surface immediately downstream of the injector.

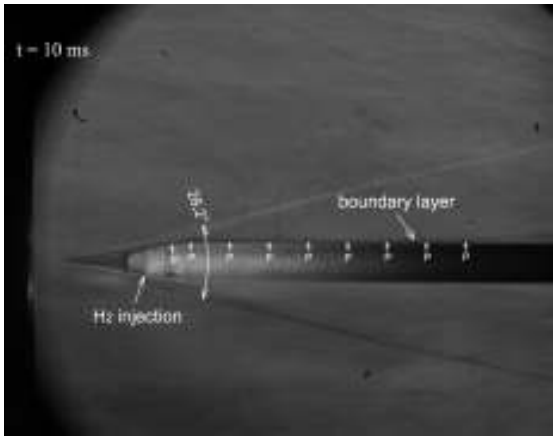


(a) Schlieren image of run 339 at flow time 10 ms

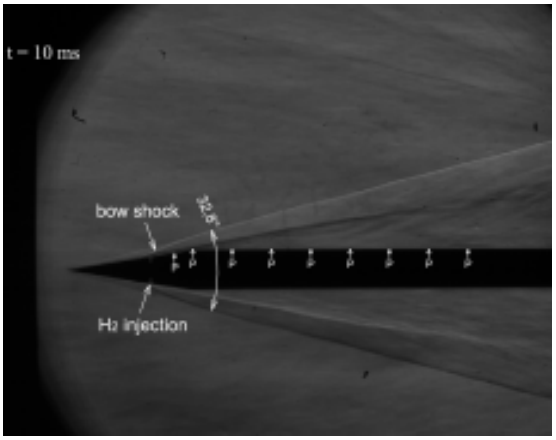


(b) Schlieren image of run 342 at flow time 10 ms

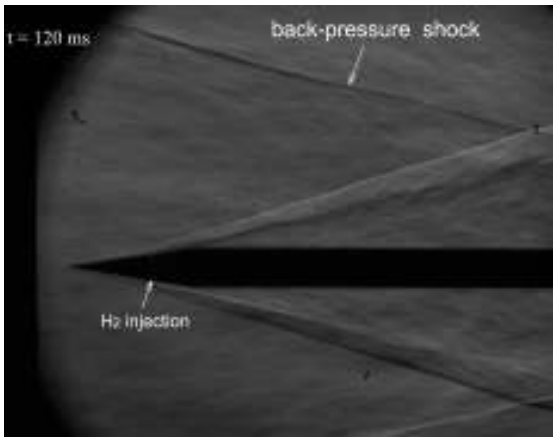


(c) Schlieren image of run 342 at flow time 120 ms

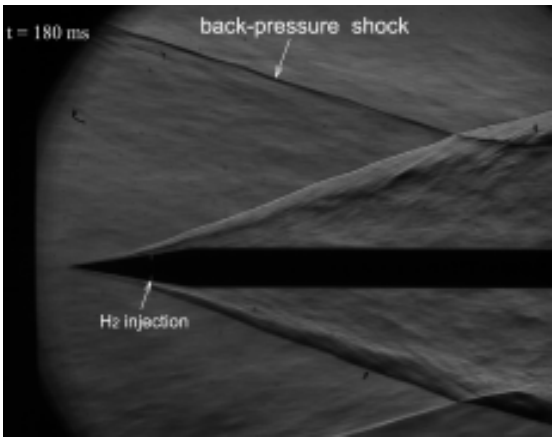


(d) Schlieren image of run 342 at flow time 180 ms

Figure 4.8: Schlieren images from the pressure measurement tests in the Mach 6 nozzle. 'P' indicates the positions of the pressure measurements.

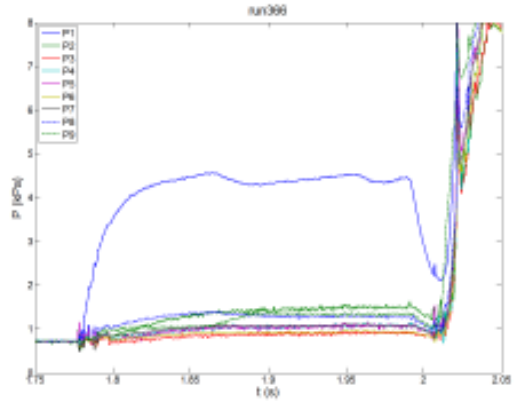


(a) Time-resolved static pressure meaurements of run 366

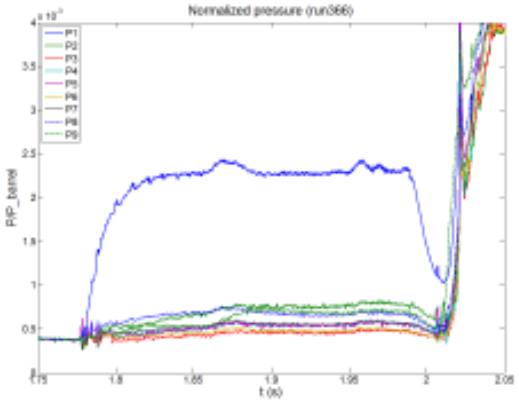


(b) Static pressure normalized with total pressure of the test flow of run 366

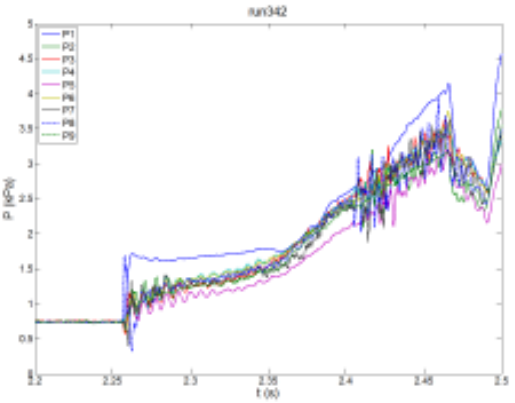


(c) Time-resolved static pressure meaurements of run 342

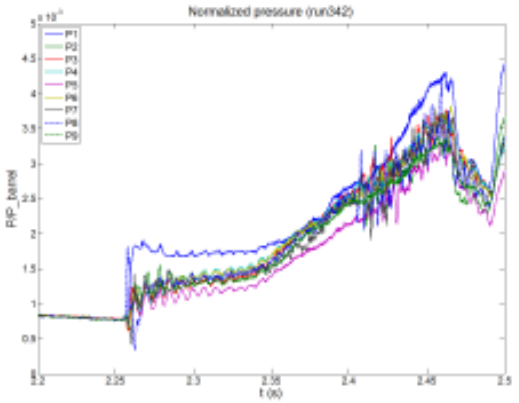


(d) Static pressure normalized with total pressure of the test flow of run 342

Figure 4.9: The time-resolved pressure measurements in the Mach 6 flow.

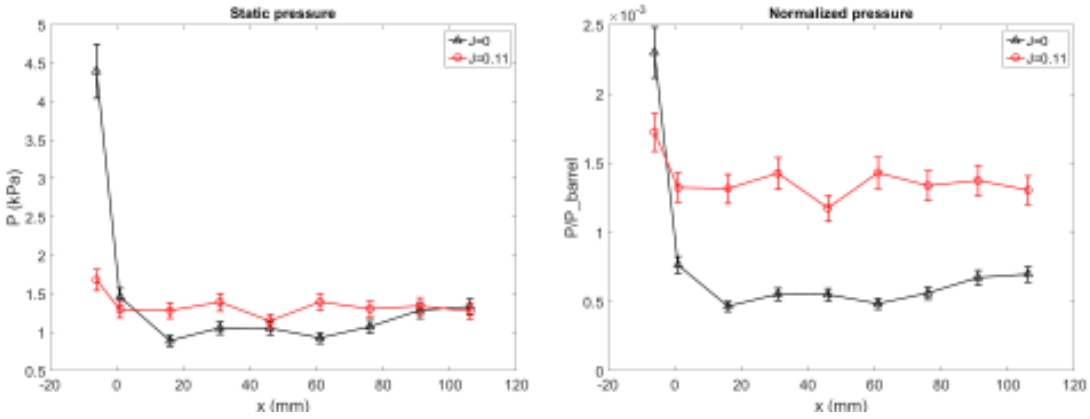


(a) Static pressure distribution (b) Normalized static pressure distribution

Figure 4.10: Static pressure distribution on the nose-cone model in the Mach 6 flow time-averaged over a nominally steady test flow period from t = 50 ms to t = 100 ms.

## 4.2 Hot Wall Experiments

The results of the heat induced combustion experiments are reported in this section for the hot surface model exposed to Mach 2, Mach 4 and Mach 6 flow. The sensitivity of the ICCD camera is calibrated firstly because it is vital for accurate data analysis of OH* concentrations. Then the deduction method for the axial temperature distribution and the hot model effect on the jet flow is discussed. The static combustion testing provides a reference for the combustion testing with high speed flow conditions. The Abel inversion is implemented for the measured OH* chemiluminescence and a method for the absolute number density computation is proposed. The Matlab codes for Abel inversion and number density computation are presented in Appendix B.

### 4.2.1 ICCD Sensitivity Calibration

The sensitivity calibration of the ICCD to determine the relative efficiency of each individual pixel in counts per unit of radiation emitted from a source is necessary when performing the data analysis.

A calibration was first performed by measuring the luminosity of a piece of white

paper illuminated from a far-positioned light source so as to generate an approximately homogeneous source when viewed by the ICCD. The exposure time was adjusted until a good signal count was achieved. The averaged result from two hundred continuous frames is shown in Figure 4.11a. Note that the coordinates of the ICCD image dictates the pixels indices. The sensitivity of individual pixels relative to an arbitrarily chosen reference point is shown in 4.11b .

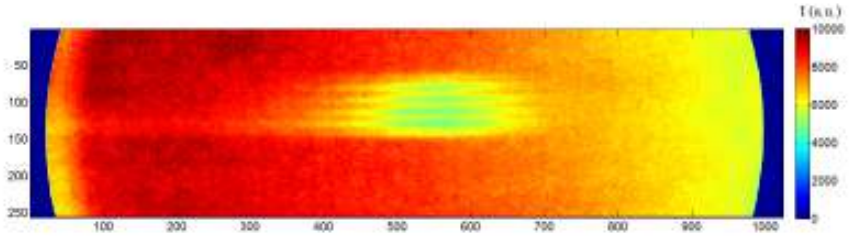

(a) The averaged intensity from 200 ICCD frames

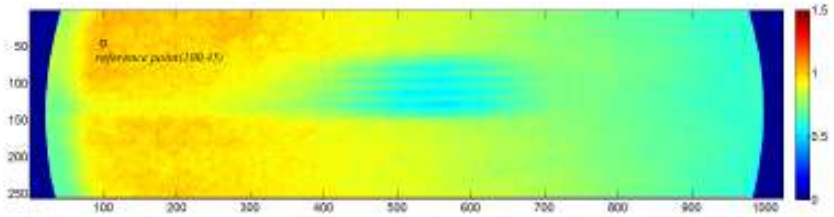

(b) Realtive sensitivity of ICCD pixels

Figure 4.11: Calibration for the spatial uniformity of the ICCD pixel sensitivity.

### 4.2.2 Deduced Temperature Distribution from ICCD Imaging

The temperature of the hot surface model is a critical factor that affects flow structures and chemical reaction rates of combustible mixtures within and near the boundary layers for the high-speed test flows. Although measurements at specified locations were obtained during testing (see Section 3.5), the axial temperature distribution along the model surface is not defined by those measurements. The temperature distribution along the model can be deduced from the ICCD recorded data to provide more detailed information to define the conditions under which the testing is taking place.

The transmission of Asahi optical bandpass filter used in this study is plotted in Fig-

ure 4.12, in which the transmitted intensity of blackbody radiation at 1500 K is also illustrated. Then the detected signals of an individual pixel receiving transmitted radiation from a blackbody via this bandpass filter can be expressed as

$$S(T) = \Omega \int_{\lambda=0}^{\infty} \xi \varepsilon \eta E_{b,\lambda}(T)\, d\lambda \tag{4.1}$$

where $E_{b,\lambda}(T)$ is the intensity of monochromatic radiation according to Planck's law, $\eta$ is transmission of the bandpass filter, $\Omega$ is the solid angle over which the light is collected, $\xi$ is the pixel efficiency in counts per unit radiative flux from the blackbody surface and $\varepsilon$ is the efficiency of the collection optics.

Because of the narrow band pass of the optical filter as shown in Figure 4.12, Eq. 4.1 can be integrated from $\lambda = 290\,nm$ to $330\,nm$, so that $\xi$ and $\varepsilon$ can therefore be treated as constant over this wavelength band. We neglect the different solid angle $\Omega$ of different pixels. Thus the signal intensity ratio at any pixel relative to the signal from pixels corresponding to the location where the temperature is measured by other instruments is given by

$$\frac{S}{S_{me}} = \frac{\xi}{\xi_{me}} \cdot \frac{\int_{\lambda=290}^{330} \eta E_{b,\lambda}(T)\, d\lambda}{\int_{\lambda=290}^{330} \eta E_{b,\lambda}(T_{me})\, d\lambda} \tag{4.2}$$

where $\xi/\xi_{me}$ can be identified by ICCD sensitivity calibration and thus the temperature at other pixels ($T$) can be deduced from the temperature measured at a particular point ($T_{me}$) by solving Eq. 4.2.

Data from the pixels located on the model axis when viewed from above are extracted for temperature deduction and are denoted with line s-e in Figure 4.13. The model positions relative to the ICCD camera field of view for all testing campaigns are also summarized in Figure 4.13. An example of pixel data extracted for temperature deduction from a static combustion test is illustrated in Figure 4.14 and the deduced temperature distribution in the axial direction based on these data according to Eq. 4.2 is shown in Figure 4.15, where the measured temperature of 1723 K is located at x = 30 mm.

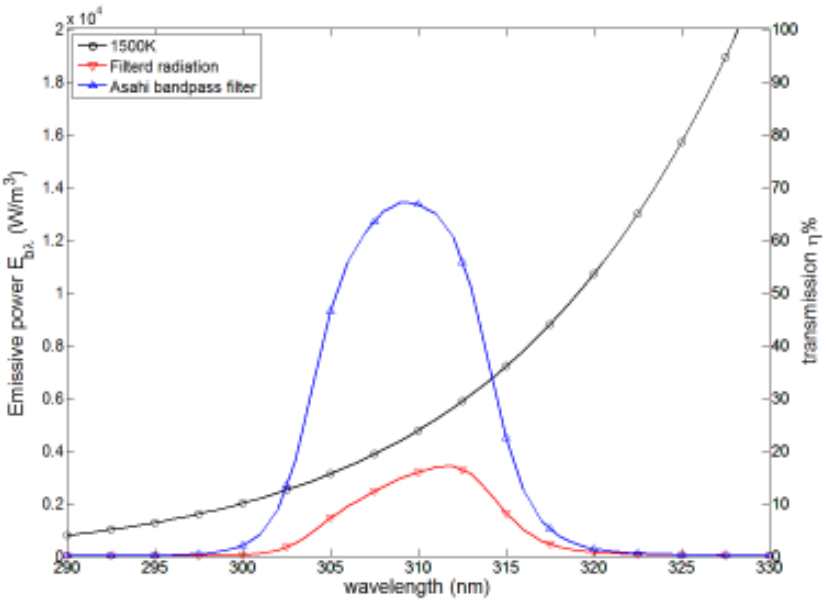


Figure 4.12: Illustration of transmitted block body radiation passing through a Asahi optical bandpass filter (XBPA310), the transmission of the filter was obtained from : `http://www.asahi-spectra.com/opticalfilters/detail.asp?key=XBPA310`

(a) PR1

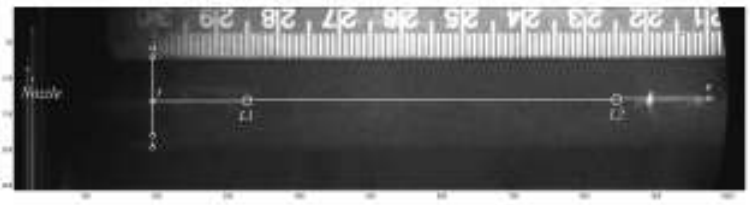

(b) PR2

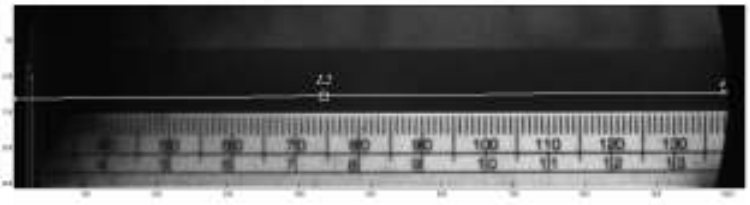

(c) PR3

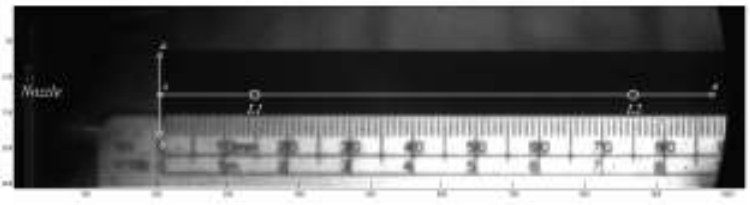

(d) PR4

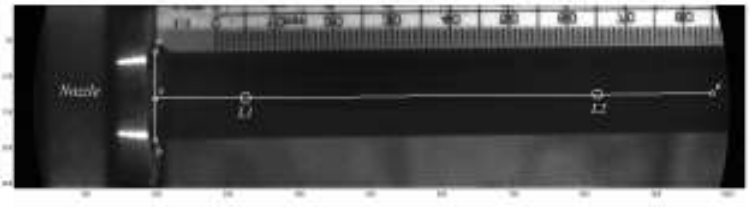

(e) PR5

Figure 4.13: The field of view summary of ICCD imaging within different combustion testing. Line a-b depicts the leading edge of graphite tube (x = 0); line s-e indicates the traces of pixels used for temperature deduction; L1 and L2 represent the detection location for the temperature measurement (TCRP and SSC175). 'PR' is abbreviation of 'Position Reference'.

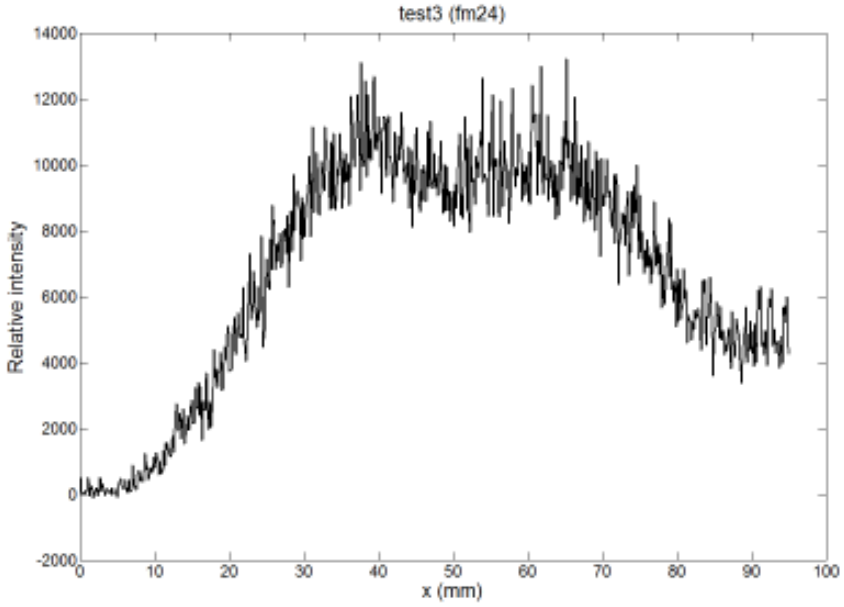


Figure 4.14: The relative intensity of pixel signals extracted from ICCD image 24 of static combustion test 3. $x = 0$ refers to the leading edge of the graphite tube.

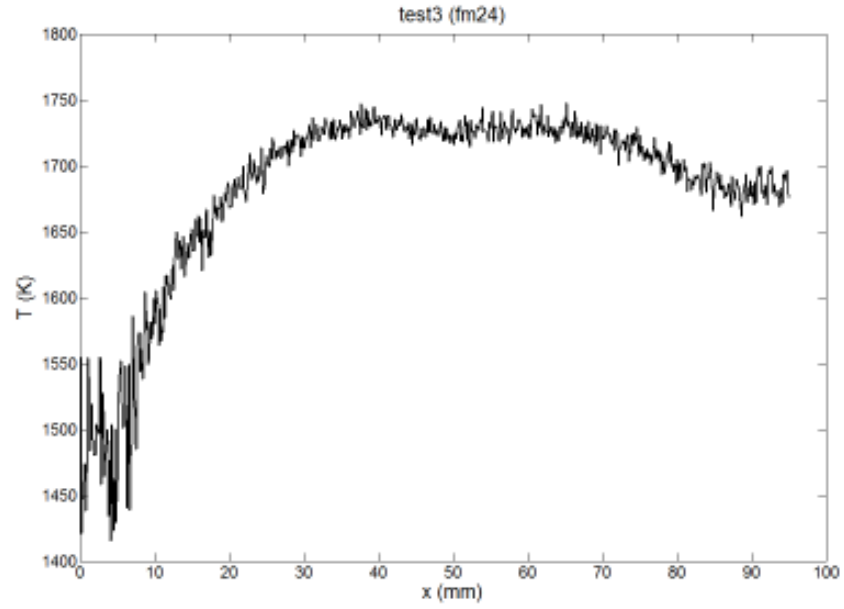


Figure 4.15: The deduced temperature distribution from ICCD image 24 of static combustion test 3. $x = 0$ refers to the leading edge of the graphite tube.

### 4.2.3 Heating Effect on Injected Flow

When it comes to high speed flow regimes, the dimensionless heat transfer coefficient Nusselt number $Nu$ or Stanton number $St$ becomes more complex to calculate than the case of low speed flow in which heat transfer is related to Reynolds number $Re$ and Prandtl number $Pr$ (Kreith et al., 2010). Taking a flat-plate for example, $St$ is plotted vs Mach number $M$ in Figure 4.16, where $St$ is the function of dimensionless parameters of $M$, $Pr$, specific heat ratio $\gamma$, the temperature ratio of wall and free stream $T_w/T$ and local $Re_x$ (Anderson, 2000)

$$St = \frac{f(M, Pr, \gamma, T_w/T)}{\sqrt{Re_x}} \tag{4.3}$$

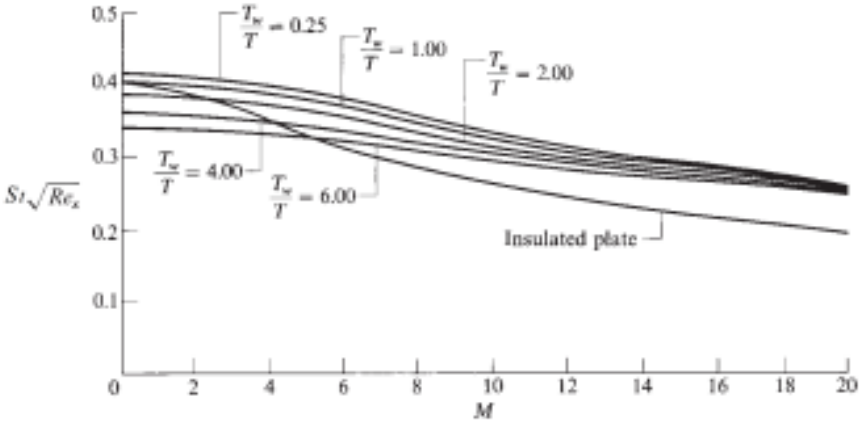


Figure 4.16: Flat-plate Stanton numbers (Anderson, 2000).

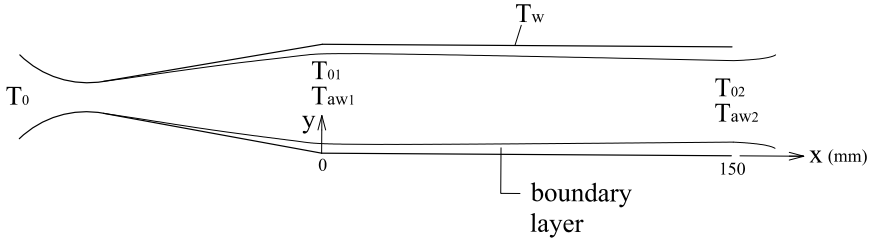


Figure 4.17: Illustration of injected fuel flow through the hot surface model (not to scale).

The hot surface model for heat induced combustion tests in this study was designed to be operated within a relative small temperature range. A stable flow is produced

when the fuel delivery system is operated at designed conditions, see Section 3.4. The analysis of fuel delivery system shows the flow speed at the mass-control nozzle exit is stabilized at Mach 3.6 approximately and will be chocked at the hot model injector exit because of frictional effect. We note from Figure 4.16 that $St$ does not change too much when the flow speed is below Mach 4 and the $T_w/T$ varies within a small range. Thus the influence of $M$, $T_w/T$ and $\gamma$ can be neglected for the particular case in this study concerning thermal analysis of the hot model heating effect on injected flow.

The schematic of injected fuel flow through the hot surface model is illustrated in Figure 4.17. An adiabatic process of flow through the mass-control nozzle and a uniform wall temperature $T_w$ starting from x = 0 in Figure 4.17 are assumed. The heat transfer to and from the surface in high-speed flow can be related to adiabatic temperature $T_{aw}$ because the viscous dissipation and conversion from kinetic to internal energy changes the boundary layer temperature distribution relative to the low-speed flow. Thus the heat flow transfered from the hot model to the jet flow can be written as

$$\dot{m}\, c_p\, (T_{02} - T_{01}) = \overline{h}\, A\, (T_w - \frac{T_{aw1} + T_{aw2}}{2}) \tag{4.4}$$

where the subscript 0 indicates the stagnation temperature and the 1 and 2 refer to the flow conditions at x = 0 and hot model injector exit. $A$ is the inner area of the flow path. The arithmetic mean value of $T_{aw1}$ and $T_{aw2}$ is used to represent the mean bulk temperature. The relationship of stagnation temperature and adiabatic temperature can be expressed with a recovery factor $r$

$$r = \frac{T_{aw} - T}{T_0 - T} \tag{4.5}$$

and the ratio of stagnation and static compressible flow temperature is

$$\frac{T_0}{T} = 1 + \frac{\gamma - 1}{2} M^2 \tag{4.6}$$

We assume $r = \sqrt{Pr}$ and that the averaged heat-transfer coefficient $\overline{h}$ can be deduced

from the incompressible empirical correlation of Dittus-Boelter (Kreith et al., 2010)

$$\overline{Nu} = \frac{\overline{h}\,d}{k} = 0.023\,Re^{0.8}\,Pr^{0.4} = 0.023\,(\frac{4\dot{m}}{\pi d\mu})^{0.8}\,Pr^{0.4} \tag{4.7}$$

The heating effect of the hot model on the injected flow was investigated by measuring the jet flow temperature variation as shown in Figure 4.18 with fuel delivery via the atmospheric blow-down operating mode. The measurement of temperature and pressure upstream the mass-control nozzle is described in Section 3.3. The measured temperature $T_0$ equals to the stagnation temperature $T_{01}$ and the flow temperature at the exit of hot model measured by a K-type fine wire thermocouple (OMEGA, dia. 0.001 inch) is $T_{aw2}$. Thus the measured temperatures and jet mass flow rate with combination of flow speed information from Section 3.4 can be used to calculate wall temperature $T_{aw}$ based on Eq. 4.4 to 4.7.

The results for the temperature measurement of the hot model surface, the flow upstream of mass-control nozzle and the exit of the model, as well as the jet mass flow rate are exhibited in Figure 4.19. The temperatures measured towards the termination of experiment are selected for thermal analysis and evaluation because hot surface temperatures of around 1500 K at this time during the heating recycle are close to temperatures used in combustion testing. The calculated $T_w$ as well as the measured temperatures and pertinent conditions used for calculation are listed in Table 4.2.

Once the wall temperature $T_w$ is obtained, the hot model effect on injected flow can be estimated by

$$T_{02} = \frac{C\,\dot{m}^{0.2}\,T_{01} + A(T_w - \frac{0.89T_{01}}{2})}{C\,\dot{m}^{0.2} + \frac{0.97A}{2}} \tag{4.8}$$

where

$$C = \frac{c_p\,d}{0.023\,(\frac{4}{\pi d\mu})^{0.8}\,Pr^{0.4}\,k} \tag{4.9}$$

It should be noted that the properties of $\mu$, $k$, $c_p$ and $Pr$ need to be calculated base on the composition of the flow medium when the evaluation of heating effect on injected flow is applied to premixed air-hydrogen mixture.

Table 4.2: Experimental conditions for the evaluation of the heating effect on injected flow

| entrance | | | | exit | | | | | | |
|---|---|---|---|---|---|---|---|---|---|---|
| $P_{01}$ kPa | $T_{01}$ K | $M_1$ | $T_{aw}/T_0$ | $T_{aw2}$ K | $M_2$ | $T_{aw}/T_0$ | $T_w$ K | $T_g$ K | $P_t$ kPa | $\dot{m}$ kg/s |
| 94.45 | 301.3 | 3.6 | 0.89 | 336.1 | 1.0 | 0.97 | 353.8 | 1552 | 1.1 | $4.94\times10^{-5}$ |

$T_g$ refers the measured surface temperature by TCRP.

$P_t$ is the pressure of the test section during the test.

Figure 4.18: Photograph of test arrangement to determine the heating effect on the jet flow.

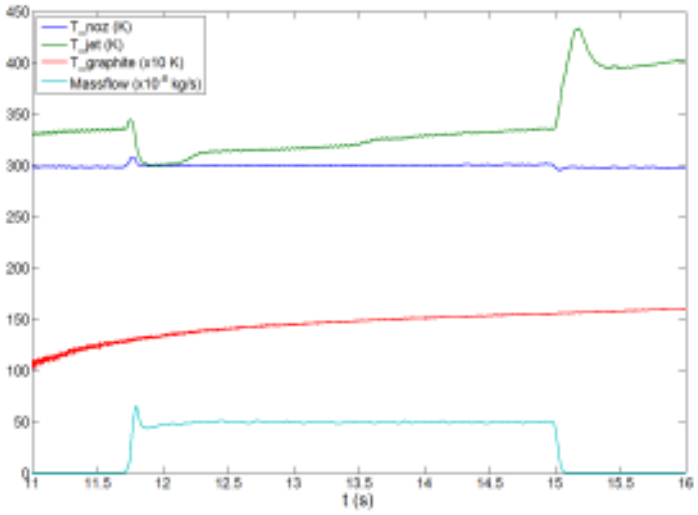


Figure 4.19: Variation of the temperature and mass flow rate during evaluation of the heating effect on injected flow.

### 4.2.4 Static Combustion Test

The chemical mechanism of hydrogen ignition is complex and is determined by the concentrations, the temperature, the pressure of hydrogen-air mixture and the residence time. A series of static combustion tests was conducted before performing the high speed flow combustion testing in the wind tunnel with the objective of proof-testing the apparatus and to target the possible conditions under which the ignition might occur. The testing was conducted based on the step-cone model (see Section 3.3 for details) by using the premixed hydrogen-air mixture.

The test conditions are summarized in Table 4.3. The time-resolved measurements including the timing of the ICCD camera frames are presented in Figure 4.20. The deduced axial temperature distribution corresponding to the ICCD image recorded just before the onset of the hydrogen injection are illustrated in Figure 4.21. Note that the temperature distribution of Test 3 is presented in the aforementioned Figure 4.15. Figure 4.22 illustrates the position of model and injector in the ICCD imaging field of view, and this position applies not only for static combustion test but also for combustion tests of the step-cone model with the Mach 4 nozzle.

The ICCD camera was operated in the Free Run mode and recorded 50 frames. The acquisition frequency in the Free Run model is 0.3 seconds approximately and the exposure time was set to 20 ms. The camera was triggered manually to start recording at the same time as when the heating of the model was initiated in order to capture the entire heating cycle with the ICCD imaging. The time evolution of ICCD imaging of these four tests is displayed in Figure 4.23, 4.24, 4.25 and 4.26. Note the frames presented here were identified to provide visual contrast through the sequence.

It is observed that the hydrogen-air mixture was ignited when the background pressure was increased up to 10 kPa. Comparing the two cases with 10 kPa background pressure it is also observed that the flame is positioned further upstream with reduced jet flow speed. Although the empirical ignition time of stoichiometric hydrogen-air mixture is valid for the pressure range of 0.2 to 2 atm (Pergament, 1963), the estimation of ignition delay length $L_{ignition}$ is calculated here and may provide some insight to the

combustion phenomena that occurred during the testing:

$$L_{ignition} = \frac{8 \times 10^{-9} e^{9600/T}}{p/101300} \times u \tag{4.10}$$

The calculated ignition delay length reported in Table 4.3 differs substantially from the experimental observation where combustion first occurred at about 45 mm and 5 mm in Test 3 and Test 4 respectively, but was not observed in Test 2.

There are several reasons for this difference including: 1. The reduced possibility of molecular collisions on which the chemical reaction rates depend does not scale in the manner of Eq. 4.10 when pressure is low. 2. The temperature of mixed flow is determined by the heat transfered from the hot surface where only a very thin high temperature layer has capability to produce the highly reactive radicals. Thus the production of radicals necessary to initiate the chain reaction is reduced which increases the ignition time.

It is interesting to notice that at the higher pressure conditions, a halo appeared surrounding the hot model prior to injection and it was blown off by the injected flow, see Figure 4.24 (fm 14, 15), 4.25 (fm 22, 23) and 4.26 (fm 12, 13). The observed weak luminosity might be caused by chemiluminescence emitted from the excited-state radical $CO_2^*$ arising from the oxidation of the graphite (Kopp, Brower, Mathieu, Petersen and Güthe, 2012).

Table 4.3: Flow conditions and temperature measurements for the static combustion tests.

| Test NO. | $\dot{m}$ (kg/s) | $u_e$ (m/s) | $P_t$ (kPa) | $T_e$ (K) | $T_g$ (K) | $\phi$ | $L_{ignition}$ (mm) | locations |
|---|---|---|---|---|---|---|---|---|
| Test 1 | $8.37\times10^{-4}$ | 370 | 1.1 | 247 | 1652 | 1.01 | 112 | L2, PR5 |
| Test 2 | $8.25\times10^{-4}$ | 143.5 | 5.0 | 298.9 | 1716 | 1.03 | 14 | L2, PR5 |
| Test 3 | $8.14\times10^{-4}$ | 71.5 | 10.0 | 299.8 | 1723 | 1.08 | 4 | L2, PR5 |
| Test 4 | $1.09\times10^{-4}$ | 9.8 | 10.0 | 299.6 | 1592 | 1.17 | 0.5 | L1, PR5 |

$T_g$ refers the measured temperature by TCRP at the time when the ICCD camera takes a frame just before the hydrogen injection.

$\phi$ refers equivalence ratio of the hydrogen-air mixture.

$P_t$ is the test section pressure.

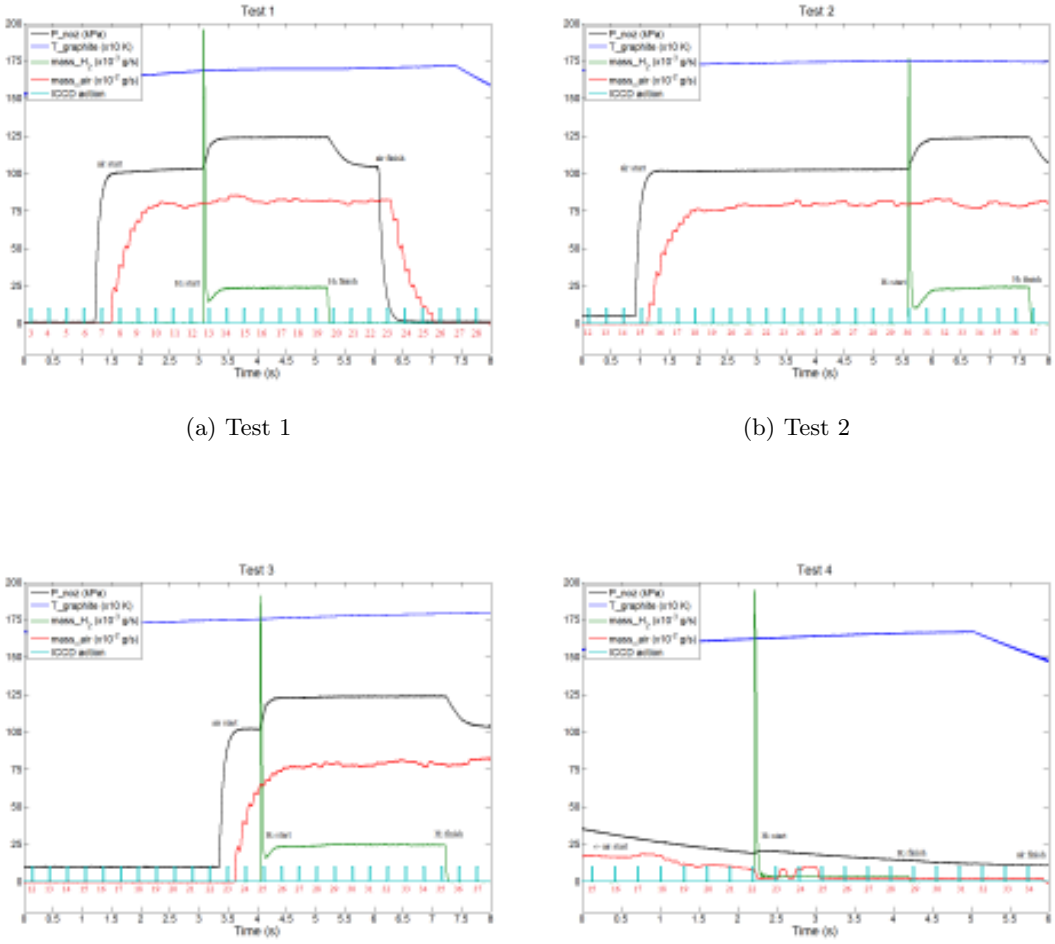


(a) Test 1

(b) Test 2

(c) Test 3

(d) Test 4

Figure 4.20: Time-resolved measurements for premixed $H_2$-Air during static tests.

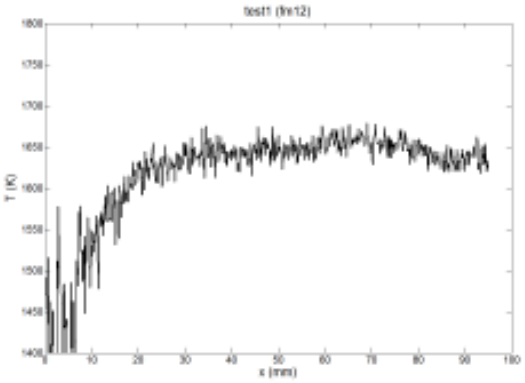


(a) Test 1

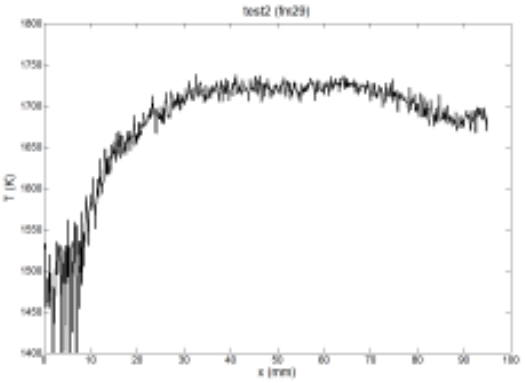


(b) Test 2

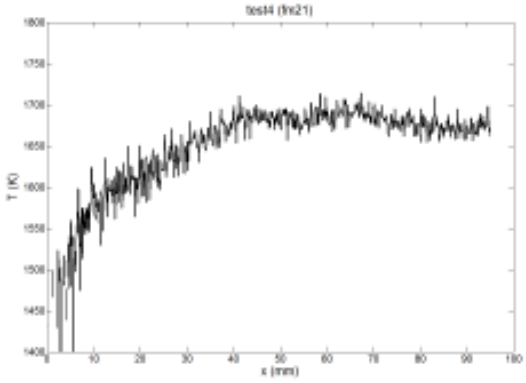


(c) Test 4

Figure 4.21: Axial distribution of surface temperature just prior to injection onset for premixed $H_2$-Air static tests. (Temperature for Test 3 is illustrated in Figure 4.15)

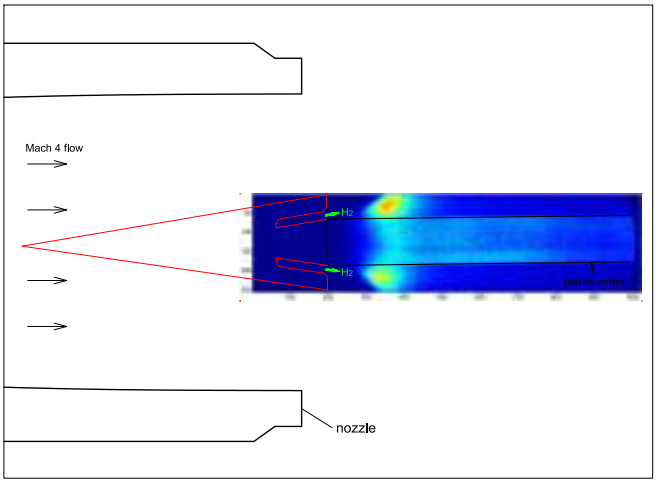


Figure 4.22: Schematic illustration of the model and injector position in the ICCD imaging field.

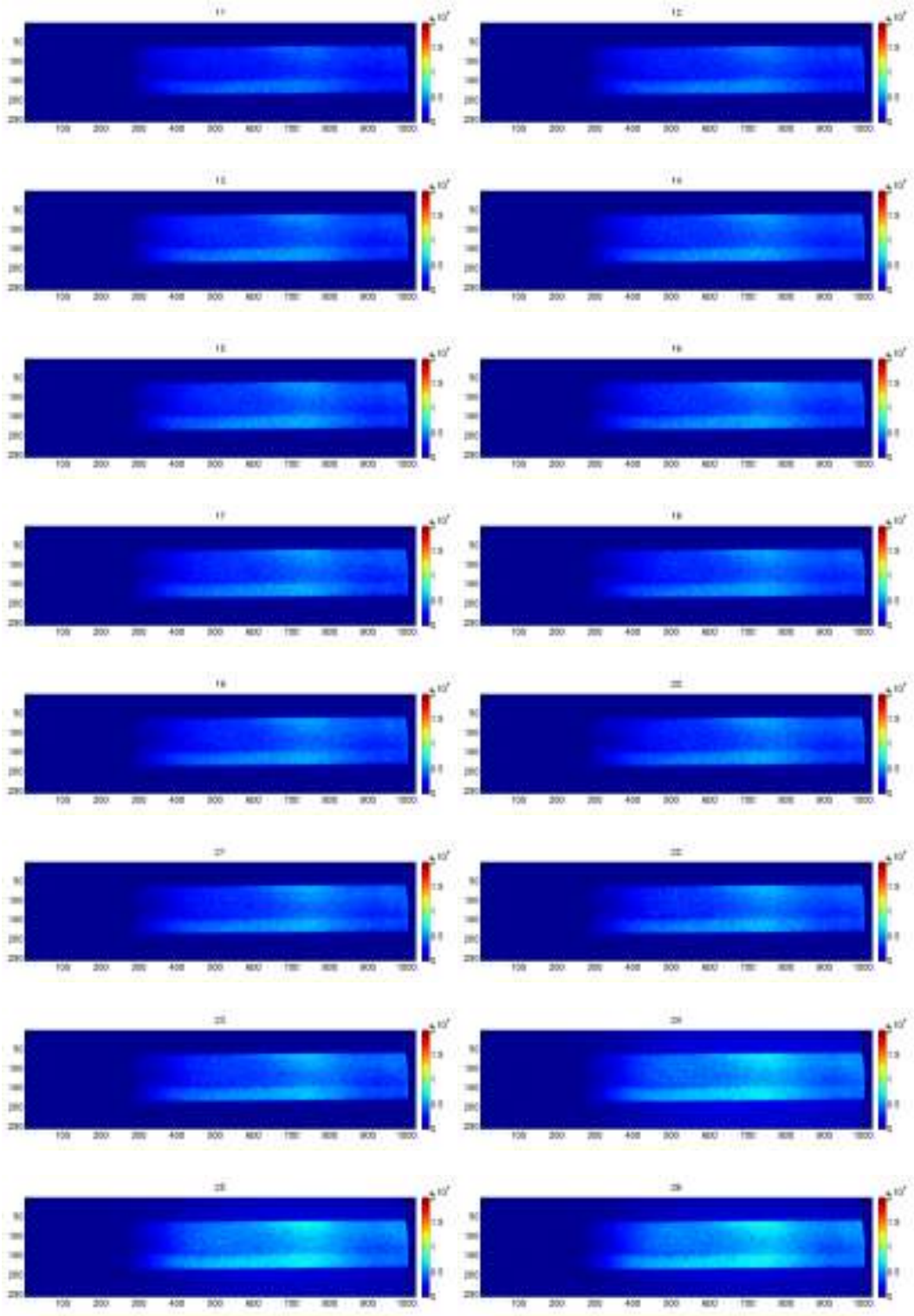

Figure 4.23: Time evolution of ICCD imaging of static combustion test at background pressure of 1.1 kPa (Test 1).

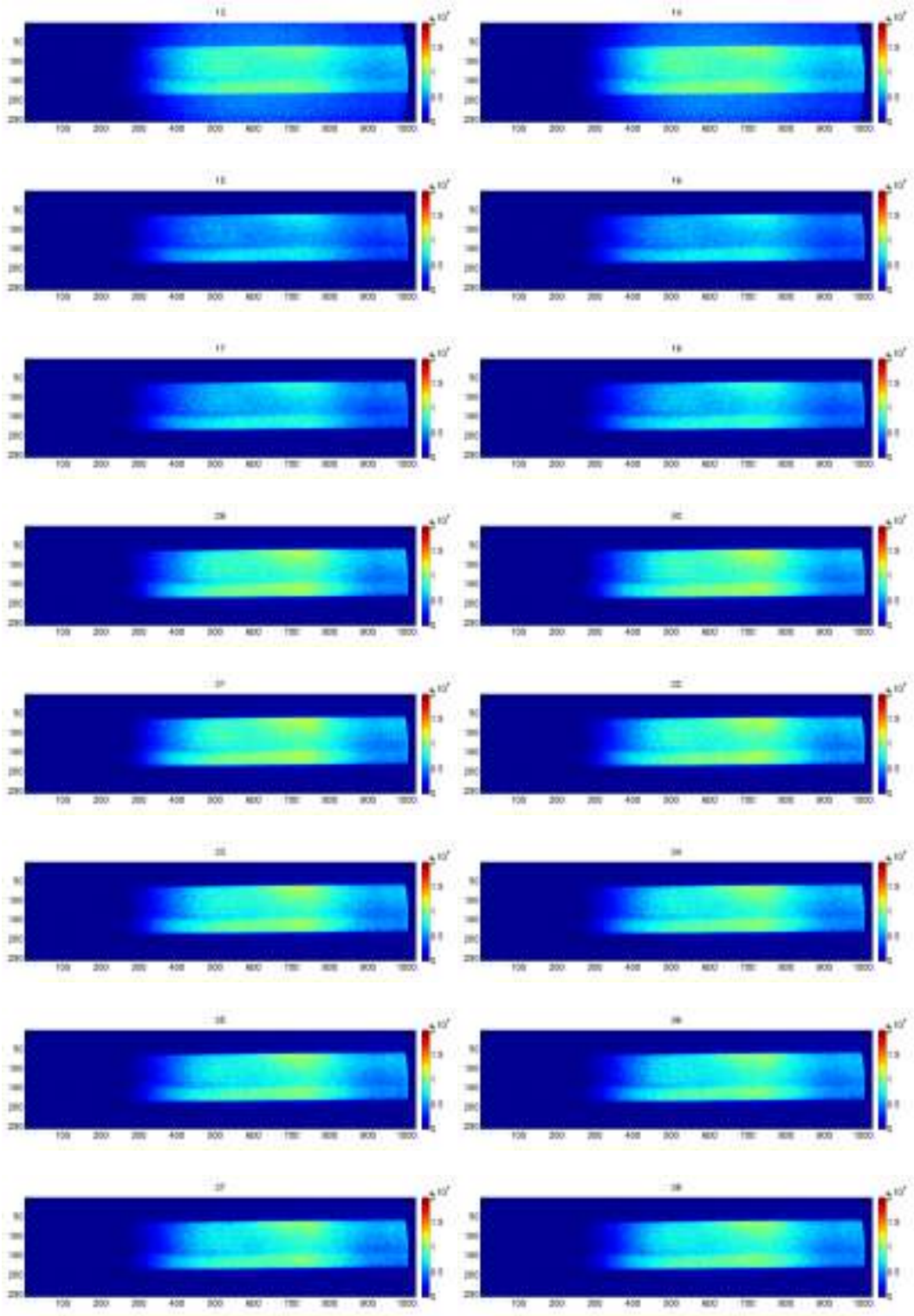

Figure 4.24: Time evolution of ICCD imaging of static combustion test at background pressure of 5.0 kPa (Test 2).

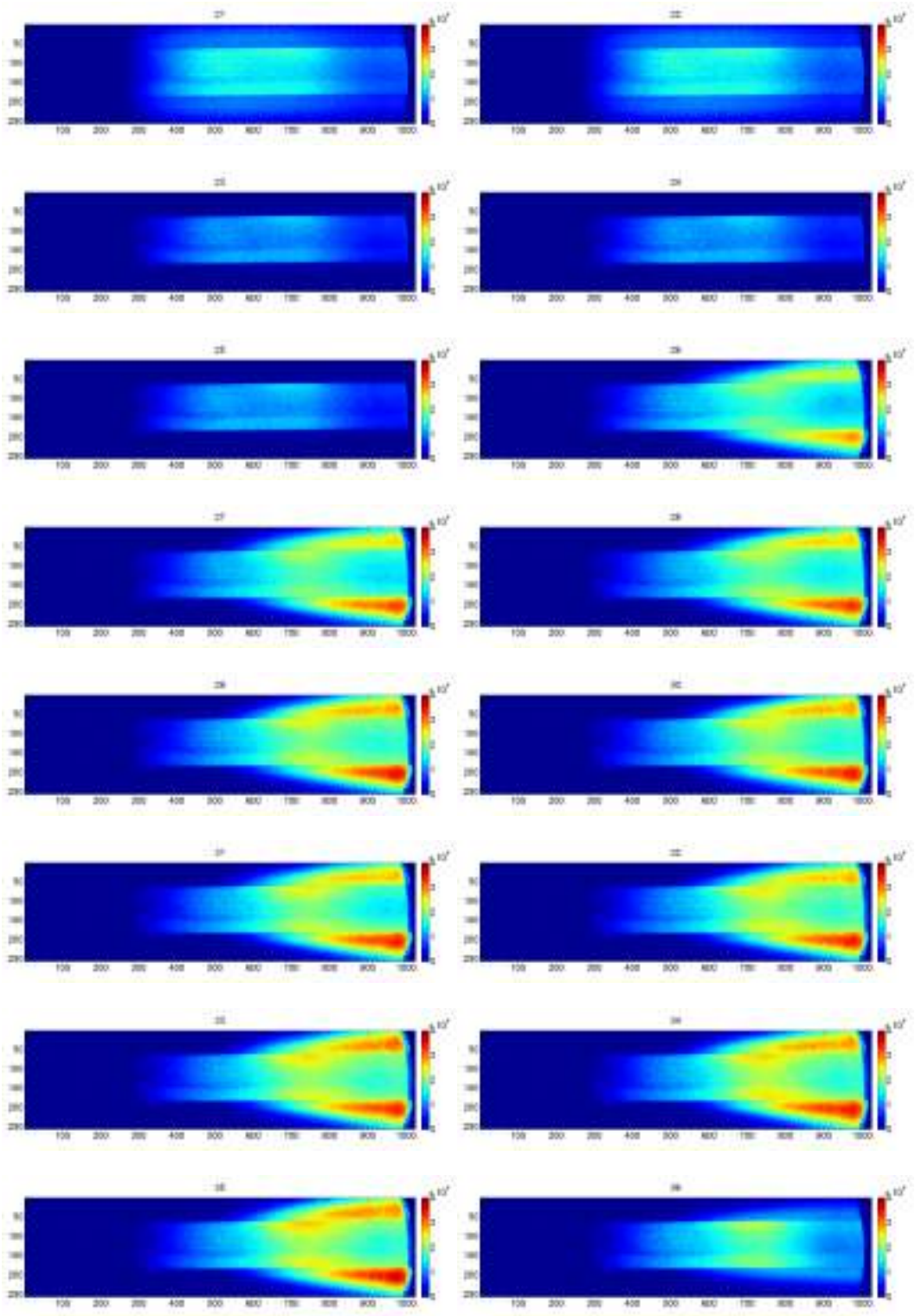

Figure 4.25: Time evolution of ICCD imaging of static combustion test at background pressure of 10.0 kPa (Test 3).

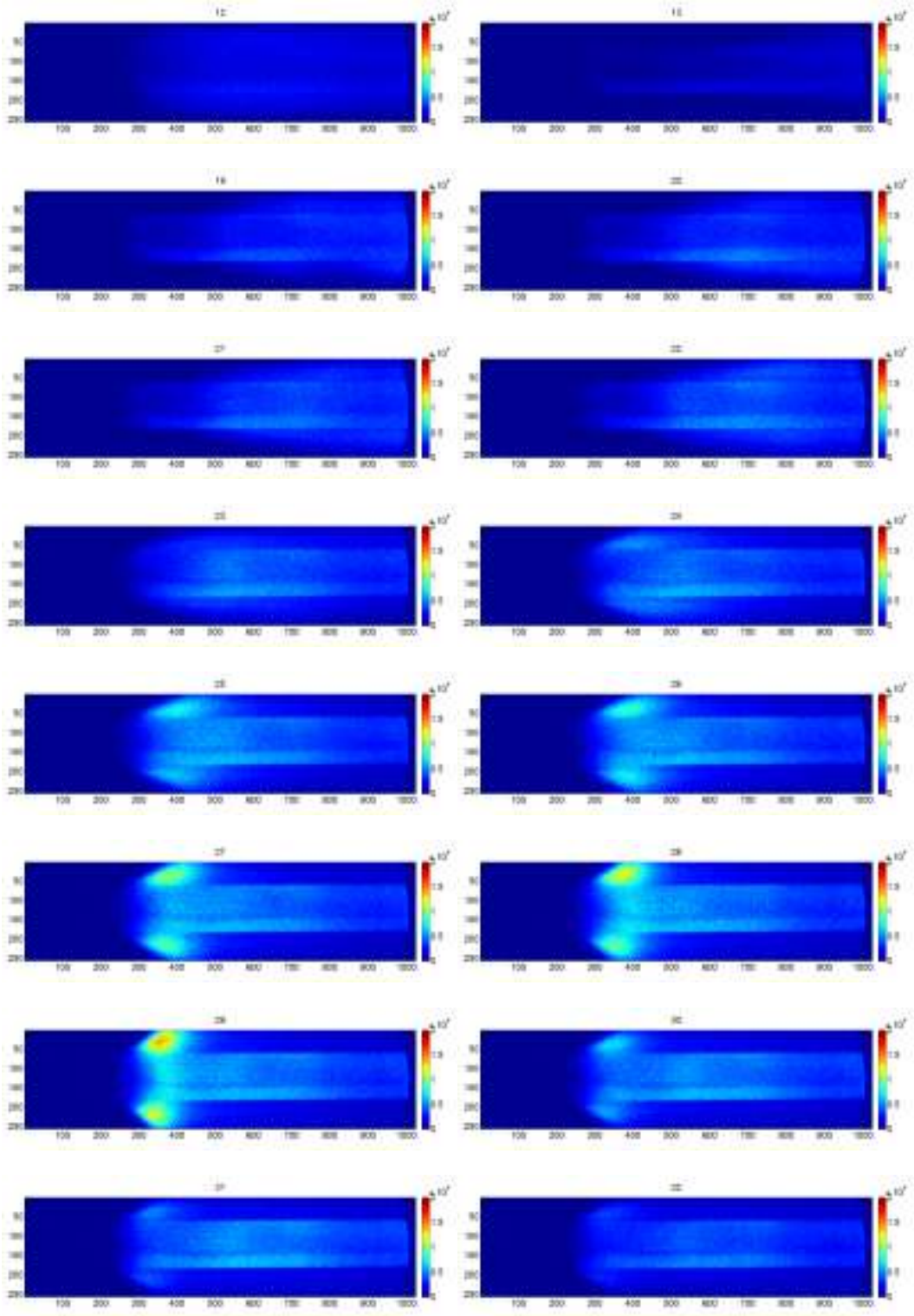

Figure 4.26: Time evolution of ICCD imaging of static combustion test at background pressure of 10.0 kPa (Test 4).

### 4.2.5 Mach 2 Combustion Test

The combustion testing using the nose-cone model (see Section 3.3) was performed at Mach 2 flow conditions with hydrogen injection. The flow conditions of the fuel jet, Mach 2 nozzle and temperature measurements are summarized in Table 4.4 which also includes the jet-to-free-stream momentum flux ratio $J$. The variation of parameters and sequencing of measurements during the testing is shown in Figure 4.27a. To define the time-resolved measurements of pressure, temperature and the fuel mass flow rate, the numbers presented on the ordinate should be scaled by the factors given in the legends when the experimental conditions need to be examined, which is the specific convention applied through out this thesis. The model position relative to the ICCD camera's field of view can be identified from Figure 4.13b and its position relative to the Mach 2 nozzle is displayed in Figure 4.1b. The axial temperature distribution deduced from the ICCD image (Figure 4.27c) is illustrated in Figure 4.27b.

The ICCD images indicate that no obvious ignition or combustion took place under the specified Mach 2 flow conditions and the geometrical configuration of experiment. Due to the relatively small size of the Mach 2 nozzle, the core flow can only cover a small region of the hot surface (13 mm from the graphite leading edge approximately, see Figure 4.1b). The pressure and temperature will decrease dramatically when the flow leaves the core flow region and goes through the expansion waves. The pressure of 30 kPa approximately within core flow region (referring to Section 4.1.1) implies an ignition delay length of 8 mm for stoichiometric hydrogen-air mixture estimated by Eq. 4.10 with a flow speed of 500 m/s at temperature of 1500 K.

As discussed previously in the context of the static combustion tests, the ignition of hydrogen fuel in air is related not only to the local flow parameters of static pressure and temperature but also the local fuel-air mixture concentration and the residence time. The poor hydrogen-air mixing can suppress the fuel ignition. Unfortunately the Schlieren images do not provide information of sufficient detail to evaluate the hydrogen mixing process; the CFD simulations presented in Chapter 5 offer some insight to the mixing process in this case.

Table 4.4: Experimental conditions of Mach 2 combustion testing.

| Test NO. | jet flow conditions | | | | | air flow & other conditions | | | | |
|---|---|---|---|---|---|---|---|---|---|---|
| | $\dot{m}$ kg/s | $u_e$ m/s | $P_e$ kPa | $T_e$ K | $J$ | $P_0$ kPa | $T_0$ kPa | $P_t$ K | $T_g$ K | locations |
| run 380 | $7.45\times10^{-4}$ | 1220 | 41.6 | 258 | 0.39 | 208 | 576 | 1.0 | 1535 | PR2, L2 |

$T_g$ refers the measured temperature by TCRP during the time of the Mach 2 flow.

$P_0$ is the total pressure of the Mach 2 flow.

$P_t$ is the pressure of test section prior to the wind tunnel operation.

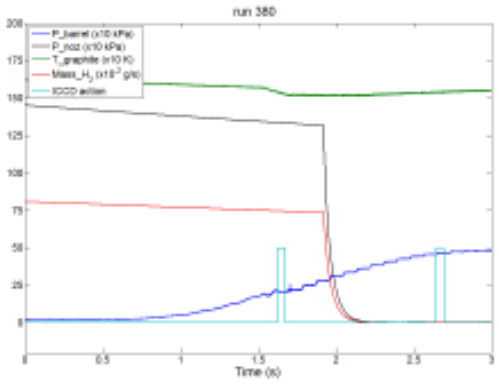


(a) Time-resolved measurements

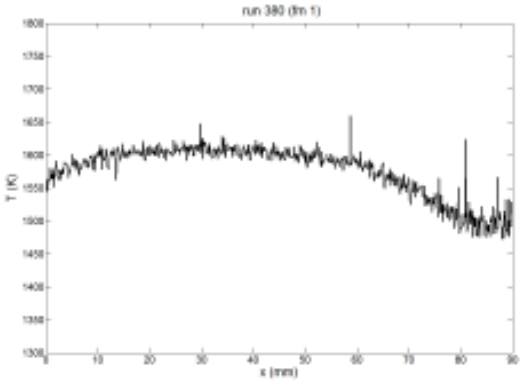


(b) Axial distribution of surface temperature

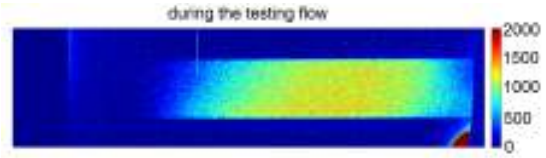


(c) ICCD imag (fm 1)

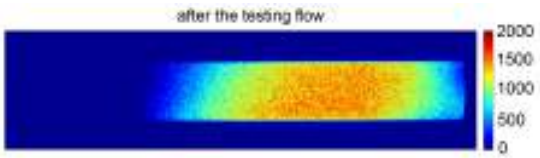


(d) ICCD image (fm 2)

Figure 4.27: Combustion testing results for run 380.

### 4.2.6 Mach 4 Combustion Test

A series of combustion tests using the nose-cone and step-cone models was performed using the Mach 4 nozzle flow with hydrogen or premixed hydrogen-air mixture injection. The flow conditions produced by the fuel jet and the Mach 4 nozzle, temperature measurement results, the equivalence ratio of hydrogen-air as well as the jet-to-free-stream momentum flux ratio $J$ of nose-cone model are summarized in Table 4.5. The

model position relative to nozzle is shown in Figure 4.28.

A range of jet mass flow rates coupled with different barrel pressures of the wind tunnel were used to explore the potential for heat induced hydrogen combustion adjacent to the hot surface. The experimental results showing the variation of parameters and sequencing of the measurements during the testing, the deduced axial temperature distribution of the hot model and the ICCD imaging are displayed in Figure 4.30 to 4.39. The position of model and injector relative to the ICCD imaging field of view can be seen in Figure 4.22. No ignition or combustion was evident from the ICCD images during the Mach 4 testing flow.

The static pressure distribution for two different TUSQ operations according to the static pressure experimental results obtained using the cold wall step-cone model (see Figure 4.7) is illustrated in Figure 4.29. The eight locations corresponding to the position of pressure transducers of step-nose model (see Section 3.3.3) used in the pressure surveying test are depicted in Figure 4.28 with symbol 'P'. Although the hot surface will alter the flow field relative to the cold surface, we expect the pressure distribution would not change too much, since a comparison of schileren images of hot surface model and cold wall model shows the position of wave structures to be largely consistent. It is noticeable that the pressure within the recirculation zone is not conducive to fuel ignition. The fuel mixture will be entrained and accelerated by the main flow when it leaves the recirculation zone and the new sub-boundary layer will be established which causes the static pressure drop. Despite the increased pressure downstream of the recirculation zone, ignition is not observed because the higher speed flow reduces the residence time significantly.

Combustion is observed in run 455 before and after the Mach 4 nozzle flow; testing in this case was carried out under the increased initial background pressure of 10 kPa. The detected OH* chemiluminescence signal is much more intense after the conclusion of the Mach 4 nozzle flow because of the elevated test section pressure of 15 kPa approximately which arises from the additional air mass in the test section and dump tank volume after the run.

Figure 4.40 shows images extracted from the high-speed camera footage during the

initial 2.5 ms of test flow. The frame rate in this case was 2 kHz. It is interesting to note that tiny particles ablated from heated graphite model are recorded by the camera as denoted with the red rectangle for zoom-in views of magnified segments in Figure 4.40 b and c.

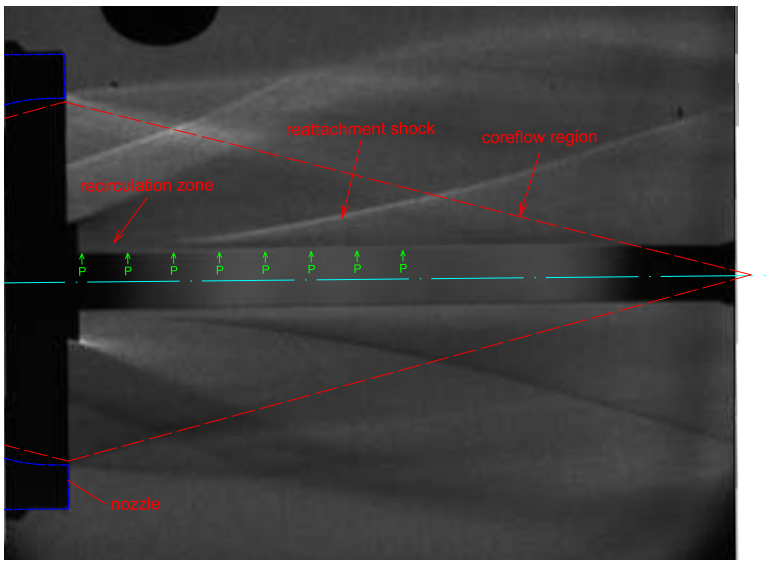


Figure 4.28: Model position relative to the Mach 4 nozzle. 'P' indicates the positions corresponding to where the pressure measurements were located in cold wall model.

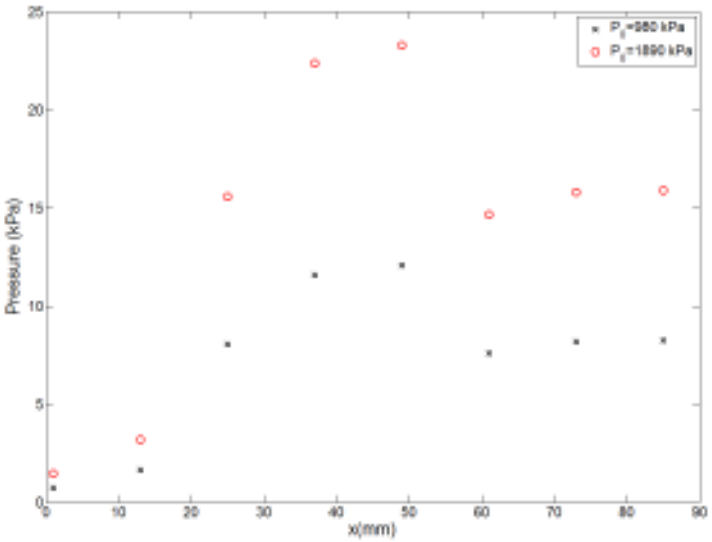


Figure 4.29: Static pressure distribution of two TUSQ operation conditions obtained from the results of static surface measurement using the cold wall cone-step model with the Mach 4 nozzle (see Section 4.1.2). $x = 0$ refers to the leading edge of the graphite tube.

Table 4.5: Experimental conditions of Mach 4 combustion testing.

| Test NO. | jet flow conditions | | | | | | air flow & other conditions | | | | |
|---|---|---|---|---|---|---|---|---|---|---|---|
| | $\dot{m}$ kg/s | $u_e$ m/s | $P_e$ kPa | $T_e$ K | $\phi$ | $J$ | $P_0$ kPa | $T_0$ K | $P_t$ kPa | $T_g$ K | locations |
| | nose-cone model | | | | | | | | | | |
| run 425 | $6.02\times10^{-4}$ | 1218 | 33.6 | 257.2 | - | 0.32 | 984 | 579 | 0.9 | 1637 | PR3, L2 |
| run 426 | $7.93\times10^{-4}$ | 1218 | 44.3 | 257.3 | - | 0.22 | 1928 | 577 | 0.9 | 1757 | PR3, L2 |
| run 456 | $1.20\times10^{-3}$ | 550 | 30.2 | 254.4 | 5.96 | 0.15 | 1924 | 579 | 1.0 | 1750 | PR5, L1 |
| | step-cone model | | | | | | | | | | |
| run 435 | $9.36\times10^{-5}$ | 341 | 2.7 | 328.2 | - | $1.7\times10^{-3}$ | 920 | 582 | 1.0 | 1729 | PR3, L2 |
| run 436 | $2.41\times10^{-5}$ | 94.9 | 2.7 | 353.9 | - | $1.2\times10^{-4}$ | 927 | 582 | 0.8 | 1771 | PR3, L2 |
| run 438 | $2.30\times10^{-5}$ | 90.5 | 2.7 | 353.9 | - | $1.1\times10^{-4}$ | 934 | 584 | 0.9 | 1747 | PR4, L2 |
| run 442 | $1.40\times10^{-4}$ | 496 | 2.7 | 319.8 | - | $3.5\times10^{-3}$ | 958 | 582 | 0.9 | 1764 | PR4, L2 |
| run 449 | $8.52\times10^{-4}$ | 283 | 2.7 | 311.2 | 1.01 | $1.2\times10^{-2}$ | 980 | 582 | 0.8 | 1656 | PR5, L2 |
| run 452 | $8.49\times10^{-4}$ | 164 | 4.6 | 307.8 | 1.02 | $3.6\times10^{-3}$ | 1893 | 578 | 0.9 | 1712 | PR5, L2 |
| run 455 | $1.40\times10^{-4}$ | 28.2 | 4.6 | 320.2 | 1.03 | $1.0\times10^{-4}$ | 1897 | 572 | 10.0 | 1784 | PR5, L1 |

$T_g$ refers the measured temperature by TCRP during the time of the Mach 4 flow.

$P_0$ is the total pressure of the Mach 4 flow.

$P_t$ is the pressure of test section prior to the wind tunnel operation.

$\phi$ refers equivalence ratio of hydrogen-air mixture; '-' represents the pure hydrogen was used.

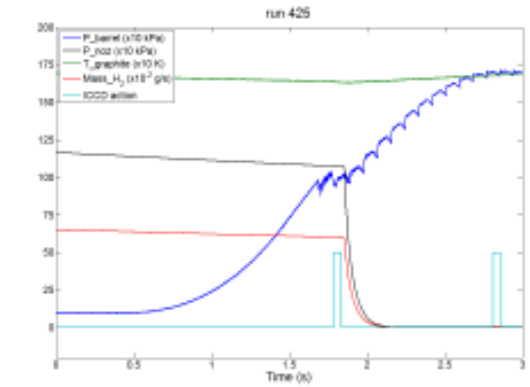


(a) Time-resolved measurements

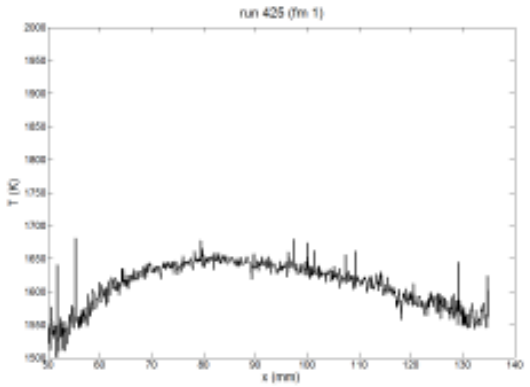


(b) Axial distribution of surface temperature


(c) ICCD imaging (fm 1)

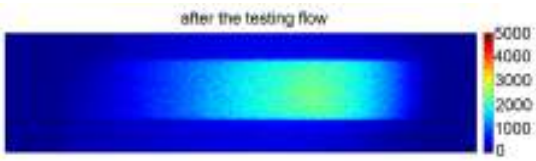


(d) ICCD imaging (fm 2)

Figure 4.30: Combustion testing results for run 425.

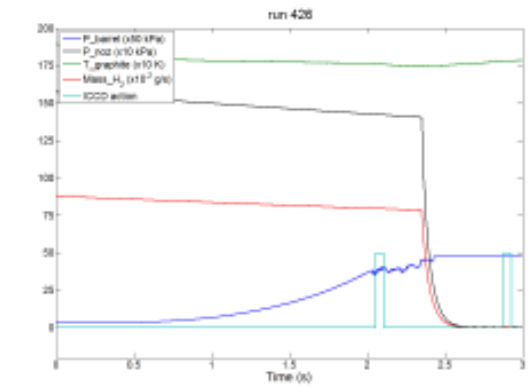


(a) Time-resolved measurements

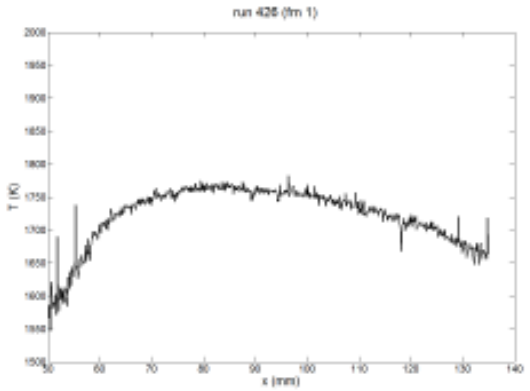


(b) Axial distribution of surface temperature

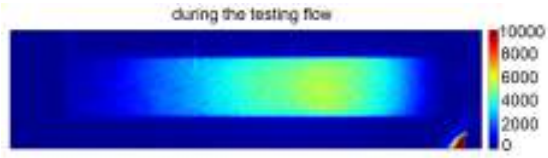


(c) ICCD imaging (fm 1)

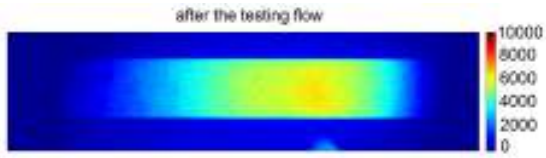


(d) ICCD imaging (fm 2)

Figure 4.31: Combustion testing results for run 426.

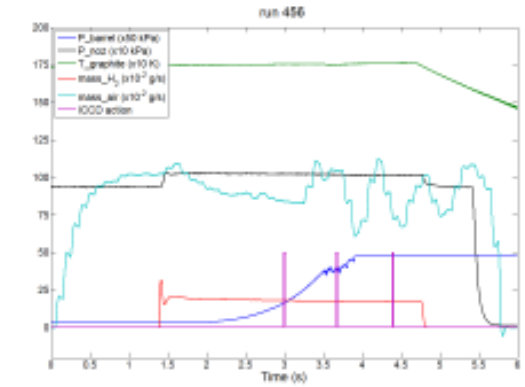


(a) Time-resolved measurements

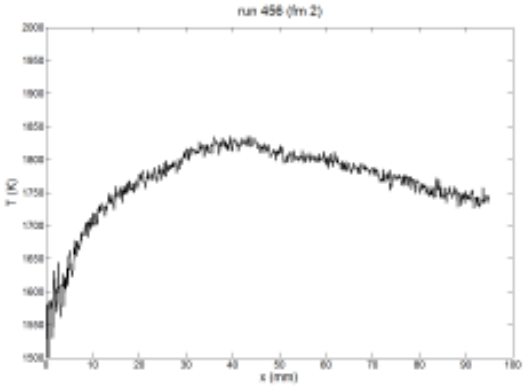


(b) Axial distribution of surface temperature

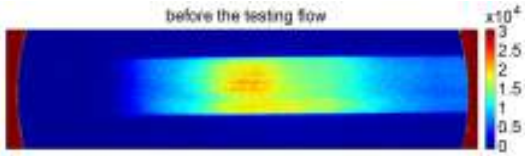


(c) ICCD imaging (fm 1)

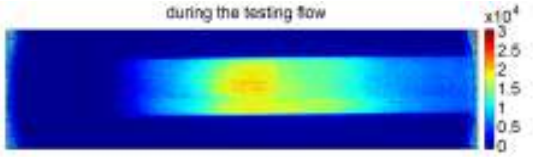


(d) ICCD imaging (fm 2)

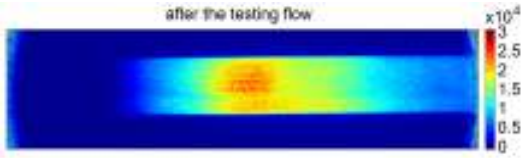


(e) ICCD imaging (fm 3)

Figure 4.32: Combustion testing results for run 456.

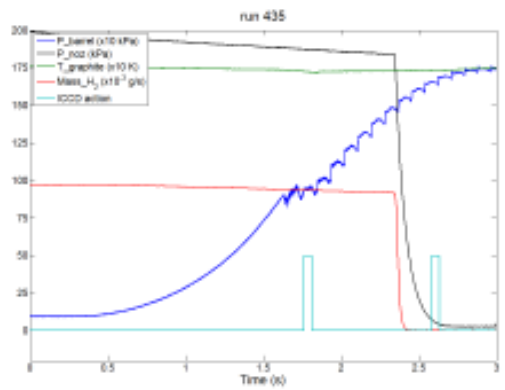


(a) Time-resolved measurements

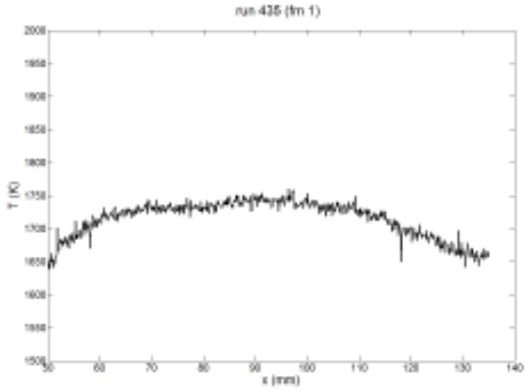


(b) Axial distribution of surface temperature


(c) ICCD imaging (fm 1)

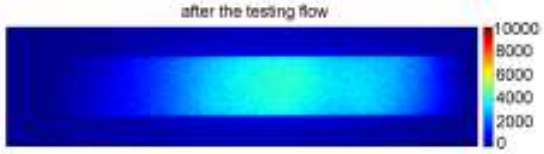


(d) ICCD imaging (fm 2)

Figure 4.33: Combustion testing results for run 435.

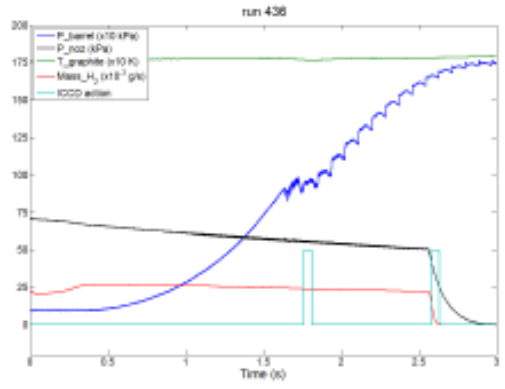


(a) Time-resolved measurements

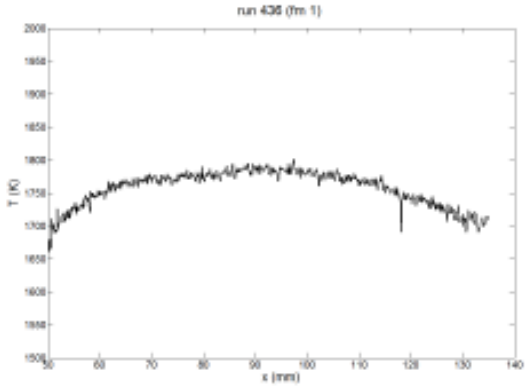


(b) Axial distribution of surface temperature

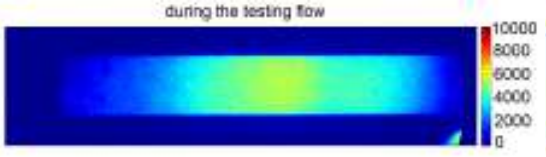


(c) ICCD imaging (fm 1)

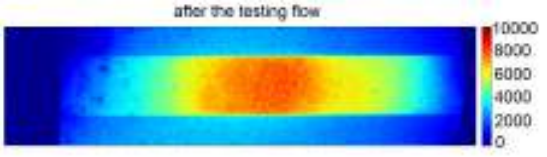


(d) ICCD imaging (fm 2)

Figure 4.34: Combustion testing results for run 436.

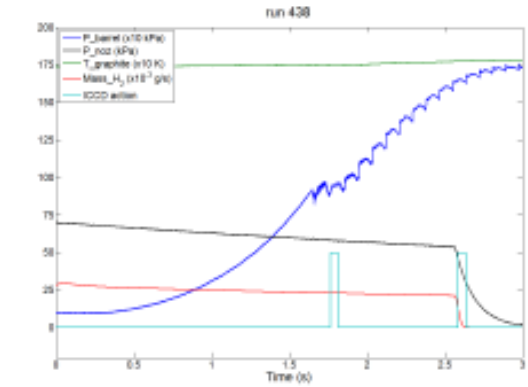


(a) Time-resolved measurements

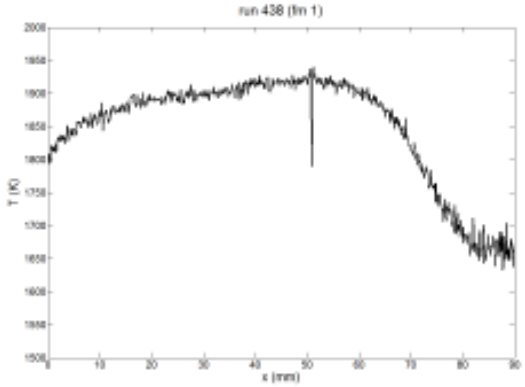


(b) Axial distribution of surface temperature

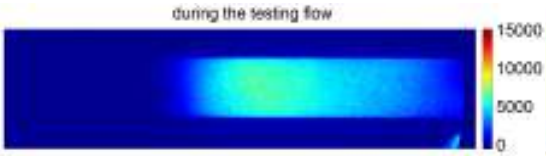


(c) ICCD imaging (fm 1)

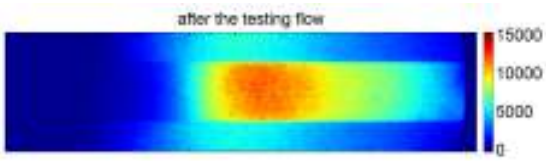


(d) ICCD imaging (fm 2)

Figure 4.35: Combustion testing results for run 438.

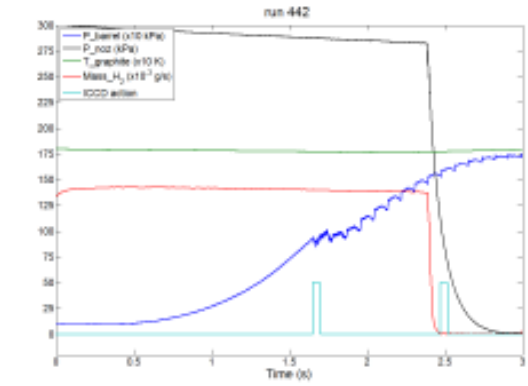


(a) Time-resolved measurements

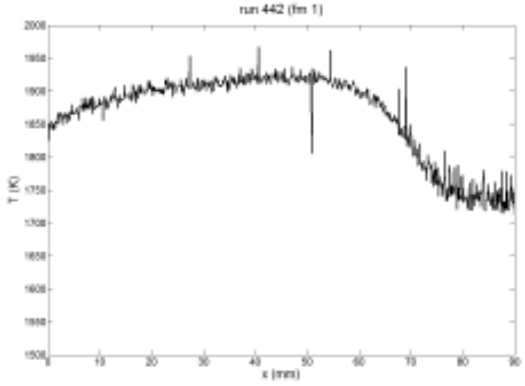


(b) Axial distribution of surface temperature


(c) ICCD imaging (fm 1)

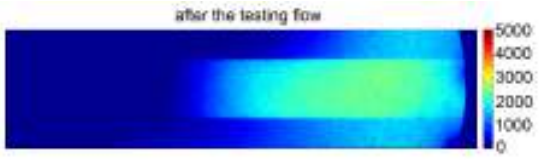


(d) ICCD imaging (fm 2)

Figure 4.36: Combustion testing results for run 442.

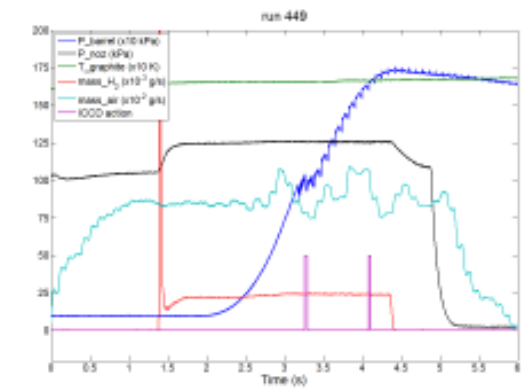


(a) Time-resolved measurements

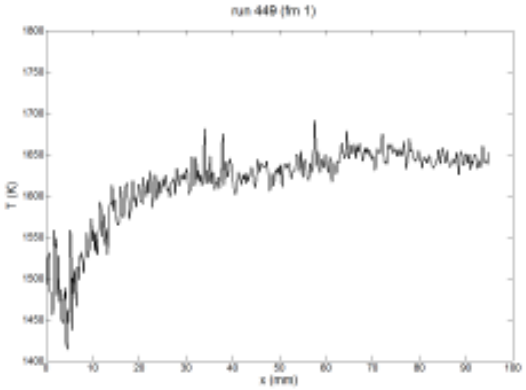


(b) Axial distribution of surface temperature

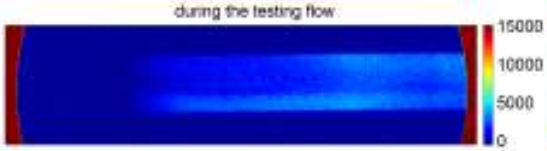


(c) ICCD imaging (fm 1)


(d) ICCD imaging (fm 2)

Figure 4.37: Combustion testing results for run 449.

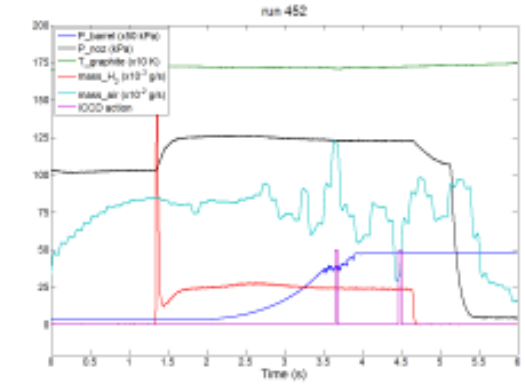


(a) Time-resolved measurements

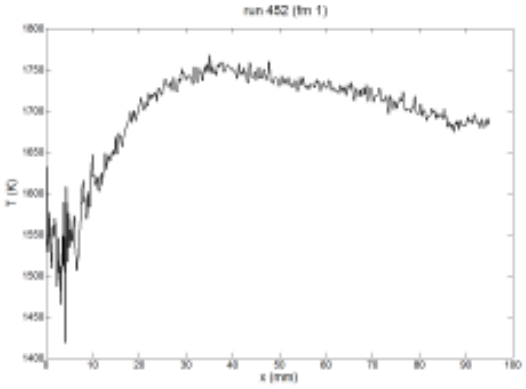


(b) Axial distribution of surface temperature

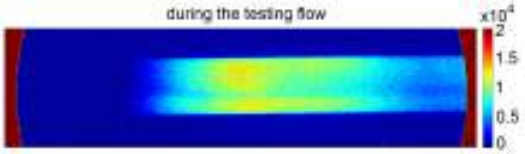


(c) ICCD imaging (fm 1)

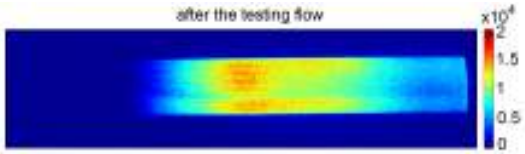


(d) ICCD imaging (fm 2)

Figure 4.38: Combustion testing results for run 452.

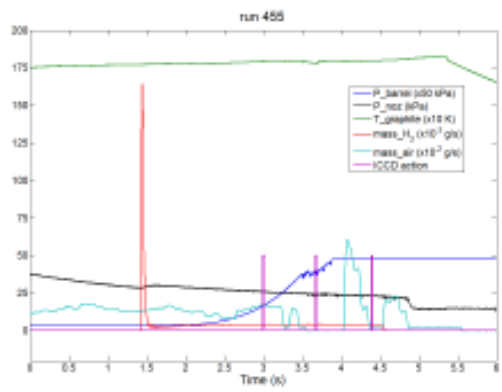


(a) Time-resolved measurements

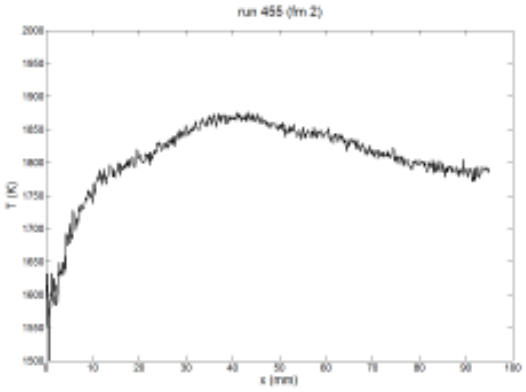


(b) Axial distribution of surface temperature

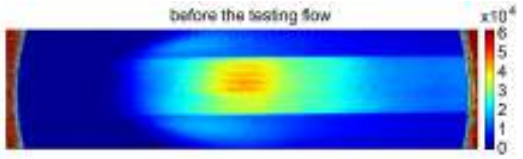


(c) ICCD imaging (fm 1)

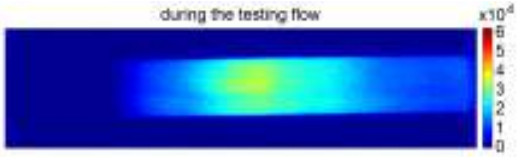


(d) ICCD imaging (fm 2)

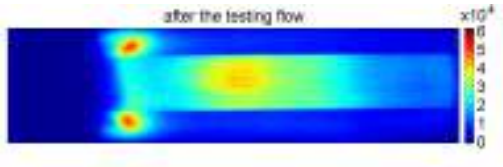


(e) ICCD imaging (fm 3)

Figure 4.39: Combustion testing results for run 455.

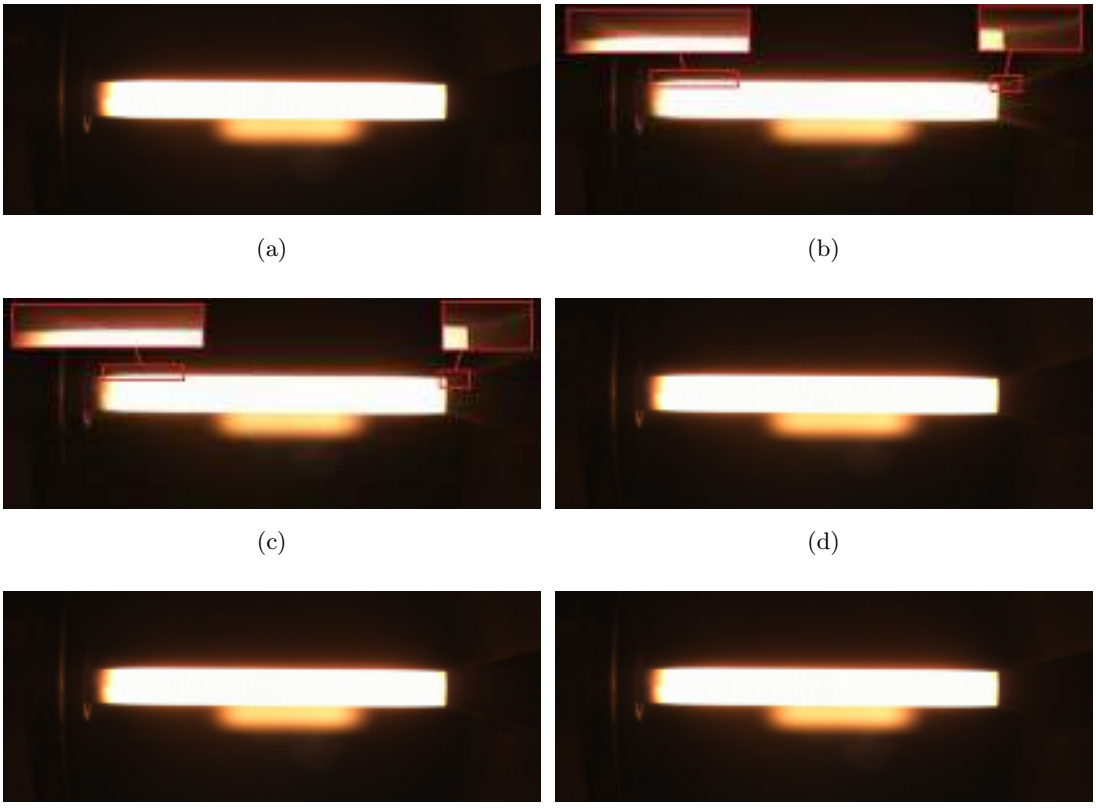

(a) (b)

(c) (d)

(e) (f)

Figure 4.40: Images extracted from high speed camera footage during the first 2.5 ms of test flow (run 438). The zoom-in views of the magnified segment is shown in red rectangle.

### 4.2.7 Mach 6 Combustion Test

Combustion test using the nose-cone model were also performed using the Mach 6 flow with hydrogen injection. The conditions of the fuel jet and the Mach 6 nozzle flow, the temperature measurements and jet-to-free-stream momentum flux ratio $J$ are summarized in Table 4.6. The test results are presented in Figure 4.41 to 4.43. No evidence of combustion was observed in any of the ICCD imaging from the Mach 6 testing flow. The low static pressure and temperature conditions in the of Mach 6 flow produced by current operation of the wind tunnel actually make it more difficult to ignite the fuel than in the Mach 2 and Mach 4 conditions.

Table 4.6: Experimental conditions of Mach 6 combustion testing.

| Test NO. | jet flow conditions | | | | | air flow & other conditions | | | | |
|---|---|---|---|---|---|---|---|---|---|---|
| | $\dot{m}$ kg/s | $u_e$ m/s | $P_e$ kPa | $T_e$ K | $J$ | $P_0$ kPa | $T_0$ K | $P_t$ kPa | $T_g$ K | locations |
| run 351 | $4.27\times10^{-5}$ | 1275 | 2.5 | 281.7 | 0.11 | 968 | 579 | 1.0 | 1604 | PR1, L2 |
| run 411 | $2.72\times10^{-4}$ | 1230 | 15.3 | 262.2 | 0.69 | 1928 | 579 | 0.9 | 1529 | PR3, L2 |
| run 412 | $4.89\times10^{-4}$ | 1223 | 27.4 | 259.1 | 0.48 | 2491 | 589 | 0.9 | 1618 | PR3, L1 |

$T_g$ refers the measured temperature by TCRP during the time of the Mach 6 flow.

$P_0$ is the total pressure of the Mach 6 flow.

$P_t$ is the pressure of test section prior to the wind tunnel operation.

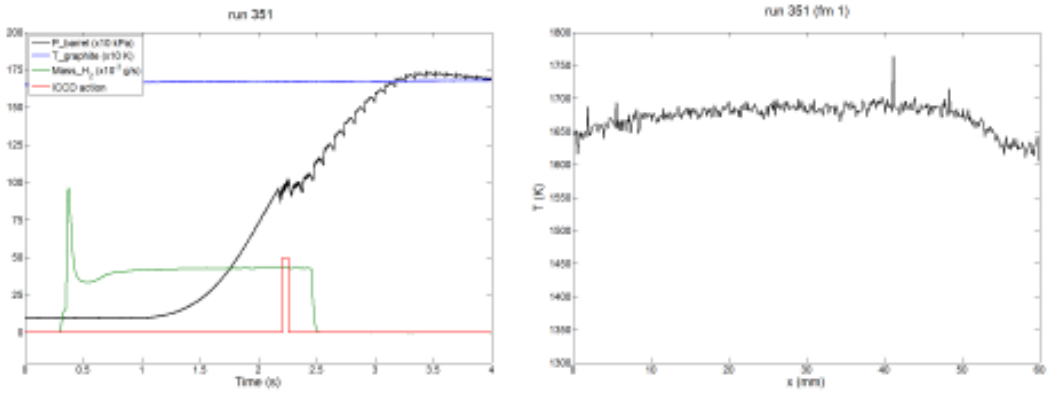


(a) Time-resolved measurements (b) Axial distribution of surface temperature

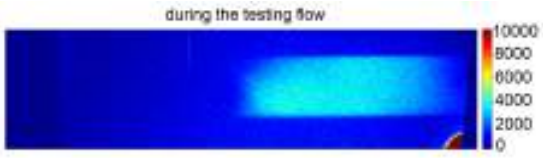


(c) ICCD imaging

Figure 4.41: Combustion testing results for run 351.

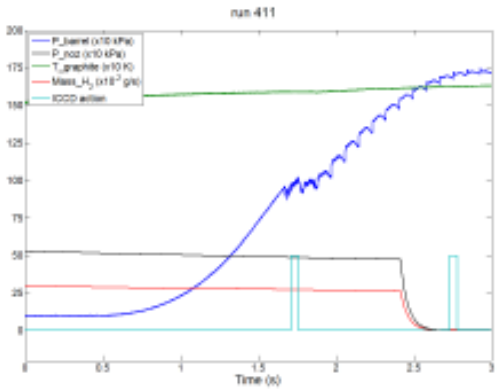


(a) Time-resolved measurements

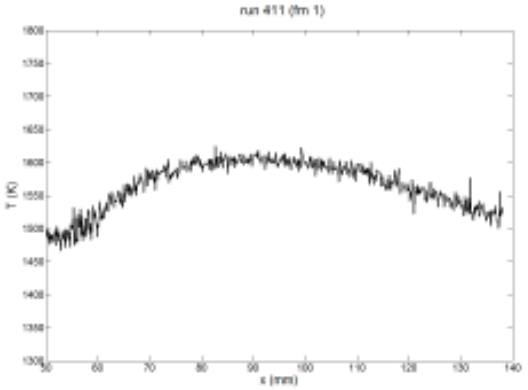


(b) Axial distribution of surface temperature


(c) ICCD imaging (fm 1)

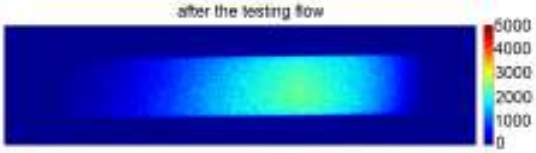


(d) ICCD imaging (fm 2)

Figure 4.42: Combustion testing results for run 411.

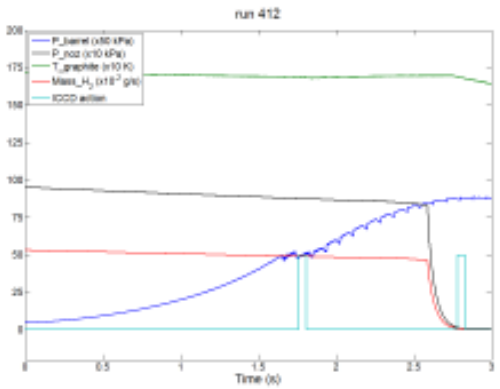


(a) Time-resolved measurements

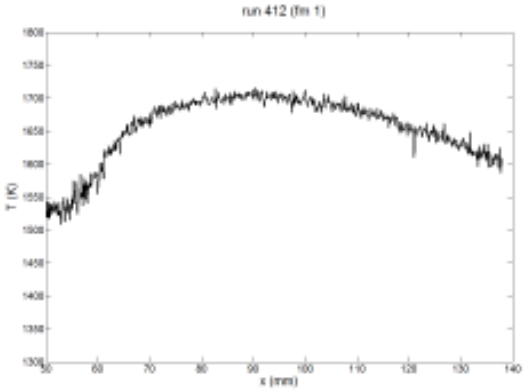


(b) Axial distribution of surface temperature

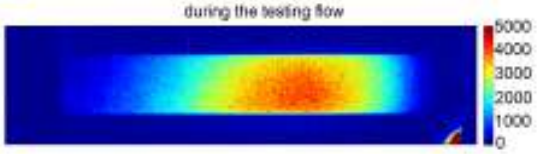


(c) ICCD imaging (fm 1)

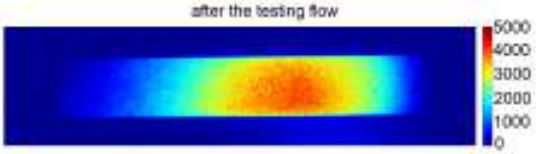


(d) ICCD imaging (fm 2)

Figure 4.43: Combustion testing results for run 412.

### 4.2.8 Abel Inversions and Absolute Number Density of Radiating OH*

In the study of cylindrically symmetrical fluid flow around objects, the line-of-sight integral projection data $P(y)$ is generally more readily measured than the radial distribution $F(r)$ of some physical quantity, as shown in Figure 4.44(a), and mathematically given by the forward Abel transformation:

$$\begin{aligned} P(y) &= 2\int_0^\infty F[(y^2+x^2)^{1/2}]dx \\ &= 2\int_y^\infty \frac{r'F(r')}{(r'^2-y^2)^{1/2}}dr' \end{aligned} \tag{4.11}$$

The well-known analytical form of the Abel inversion can be used to reconstruct the unknown radial distribution function $F(r)$ from the measured projection $P(y)$

$$F(r) = -\frac{1}{\pi}\int_r^\infty \frac{dP(y)}{dy}\frac{1}{(y^2-r^2)^{1/2}}dy \tag{4.12}$$

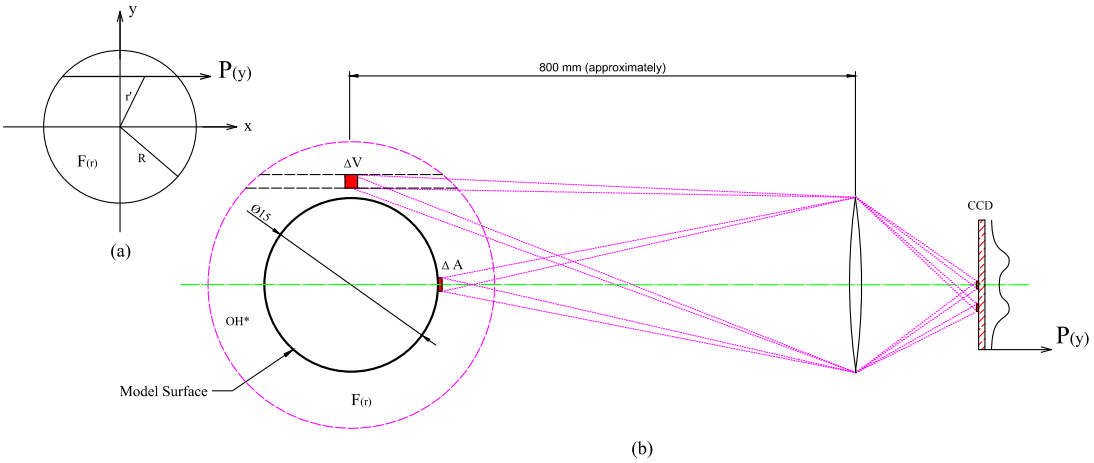


Figure 4.44: Illustration of: (a) axisymmetric field $F(r)$ with parallel collection and (b) optical arrangement of OH* chemiluminescence detecting system in present experiments.

The necessary conditions are a radially symmetrical field distribution and the value at the outer boundary $R$ and its derivative being zero when the Abel deconvolution is applied to a finite region. The inverse Abel transformation of Eq. 4.12 is not readily performed because in practice, the projection data $P(r)$ is not given analytically but in the form of a certain number of measured data points. Thus neither the differentiation

nor the integration in Eq. 4.12 can be calculated analytically. Many numerical methods have been developed to perform the Abel deconvolution based on an interpolation of either the measured data $P(y)$ or the unknown local function $F(r)$. Pretzier et al. (1992) and Fulge et al. (2011) reviewed some of these method. Pretzler et al. compared five Abel inversion methods of Matrix, h-Interpolation, f-Interpolation, Convolution method and Fourier method. The results show that the reconstruction errors are negligible when an undisturbed simulated projection $P(y)$ is used but when errors are presented in $P(y)$, the performance of the Matrix method is poor. The author recommended f-Interpolation in practice because it produces a good inversion results and is very efficiently programmed. Fulge et al. proposed a new method called the spline method with which combines the Fourier method and the f-Interpolation method. The spline method has improved behavior based on the assessment of relative construction errors, but the algorithm is more complex than these other methods.

The axisymmetrically-distributed OH* chemiluminescence produced by the heat induced combustion experiments is a good application for the Abel transformation. The test results of run 455 were selected for application of the inverse Abel transformation process and calibration to determine the OH* number density.

The Abel inversion algorithm based on the 2-point and 3-point interpolation methods as proposed by Dasch (1992) were used in this study. This method is the so-called f-Interpolation method. Another method, the Fourier-based Abel inversion as described in Pretzier (1991) was also used for comparison. Here the algorithm of these two methods is repeated in order to correct some minor typographical errors in Dasch's paper.

The projection data $P(r_j)$ at spacing $\Delta r$ can be deconvolved to give the field distribution $F(r_i)$ using

$$F(r_i) = \frac{1}{\triangle r} \sum_{j=0}^{\infty} D_{ij} P(r_j) \tag{4.13}$$

where $r_i = i\Delta r$ is the distance from the center of the object. The linear operator coefficients $D_{ij}$ are independent of the data spacing $\Delta r$.

The linear operator coefficients $D_{ij}(3pt)$ for the 3-points Abel deconvolution is given

by

$$D(i,j)(3pt) = \begin{cases} 0 & j < i-1 \\ I_{i,j+1}(0) - I_{i,j+1}(1) & j = i-1 \\ I_{i,j+1}(0) - I_{i,j+1}(1) + 2I_{i,j}(1) & j = i \\ I_{i,j+1}(0) - I_{i,j+1}(1) + 2I_{i,j}(1) - I_{i,j-1}(0) - I_{i,j-1}(1) & j \geq i+1 \\ I_{i,j+1}(0) - I_{i,j+1}(1) + 2I_{i,j}(1) - 2I_{i,j-1}(1) & j = 1i = 0 \end{cases} \tag{4.14}$$

where

$$I_{i,j}(0) = \begin{cases} 0 & j = i = 0 \; or \; j < i \\ \frac{1}{2\pi} ln \left\{ \frac{[(2j+1)^2 - 4i^2]^{1/2} + 2j + 1}{2j} \right\} & j = i \neq 0 \\ \frac{1}{2\pi} ln \left\{ \frac{[(2j+1)^2 - 4i^2]^{1/2} + 2j + 1}{[(2j-1)^2 - 4i^2]^{1/2} + 2j - 1} \right\} & j > i \end{cases} \tag{4.15}$$

$$I_{i,j}(1) = \begin{cases} 0 & j < i \\ \frac{1}{2\pi}[(2j+1)^2 - 4i^2]^{1/2} - 2jI_{i,j}(0) & j = i \\ \frac{1}{2\pi}\left\{[(2j+1)^2 - 4i^2]^{1/2} - [(2j-1)^2 - 4i^2]^{1/2}\right\} - 2jI_{i,j}(0) & j > i \end{cases} \tag{4.16}$$

The linear operator coefficients $D_{ij}(2pt)$ of 2-points Abel deconvolution is given by

$$D_{i,j}(2pt) = \begin{cases} 0 & j < i \\ J_{i,j} & j = i \\ J_{i,j} - J_{i,j-1} & j > i \end{cases} \tag{4.17}$$

where

$$J_{i,j} = \begin{cases} 0 & j < i \\ \frac{2}{\pi} & j = i = 0 \\ \frac{1}{\pi} ln \left\{ \frac{[(j+1)^2 - i^2]^{1/2} + j + 1}{[j^2 - i^2]^{1/2} + j} \right\} & j \geq i \end{cases} \tag{4.18}$$

The ICCD imaging results of run 455 which shows OH* chemiluminescence with deduction of hot surface radiation is presented in Figure 4.45. In this figure, the red rectangle indicates the region of interest for the Abel transformation and concentration calculation, and the data along the black line was extracted for a detailed illustration of the Abel inversion analysis. In order to reduce the noise, a moving average filter with

10 points was used to smooth the raw OH* chemiluminescence signals in the region of interest and the results are shown in Figure 4.46a in a zoom-in view.

Figure 4.47 illustrates the raw and smoothed OH* chemiluminescence signals extracted along the black line (X = 9.2 mm) indicated in Figure 4.45. The Abel-inverted results for the data shown in Figure 4.47 are plotted in Figure 4.48. The Abel-inverted results suggest these three algorithms have similar performance for the current data except at the center and outer boundaries. The deviation of Abel transformed results at the outermost radius arises because of the non-zero value and derivative at the outer boundary, which is due to a relatively small field of view of ICCD camera. The Fourier-based Abel method resulted in smoother inverted data; this method is claimed to be non-iterative and derivative-free but with compromised calculation efficiency and inversion quality (Pretzier, 1991).

In Figure 4.48, it is noticeable that physically unreasonable negative values appear within the radial range from 0 to 8.4 mm. Values of radius less than 7.5 mm should be zero theoretically since this radius corresponds with the graphite surface. Two factors contribute to this error. 1. The hot surface used as a calibrating source for radiation deduction has a slightly different temperature during the flow period resulting in a different radiating graphite background intensity giving a false contribution to apparent OH* chemiluminescence captured by ICCD camera (Figure 4.45). 2. Aerodynamic loading on the model during the testing causing the model to move slightly and this made it very difficulty to match the graphite edges perfectly when processing. It can be noted in Figure 4.45 that a good match for the graphite edges was achieved for the front part of the model but the matching was less successful downstream. As the Abel inversion is sensitive to the derivative values close to the point being processed, the error at the locations near the graphite edge is amplified. However, as the Abel inversion method is effectively marched from $r$ to $\infty$ (see Eq. 4.12), the Abel-inverted results at locations greater than the graphite edge would not be affected by the graphite edge and graphite background errors.

In order to assess the effect of non-zero values at the outer boundary of the ICCD images on the Abel-inverted results, the smoothed data was extrapolated to zero based on the second-order polynomial fitting as shown in Figure 4.47. The Abel-inverted result

using the 3-points method based on the extrapolated data is plotted in Figure 4.48. It is clear that the anomalous inverted results at the outer-most radius (r=16 mm) can be corrected using extrapolated data and this makes the results physically reasonable. It is interesting to note that the use of the extrapolated data does not affect the inverted peak value significantly (less than 2%) and the other values away from the outer-most radius in the present case.

Figure 4.46(b-d) illustrate the radial distribution of the signals of OH* chemiluminescence obtained via the three different Abel inversion methods. The Fourier-based method gives a high value at the outer-most radius and has high noise-filter-off capability.

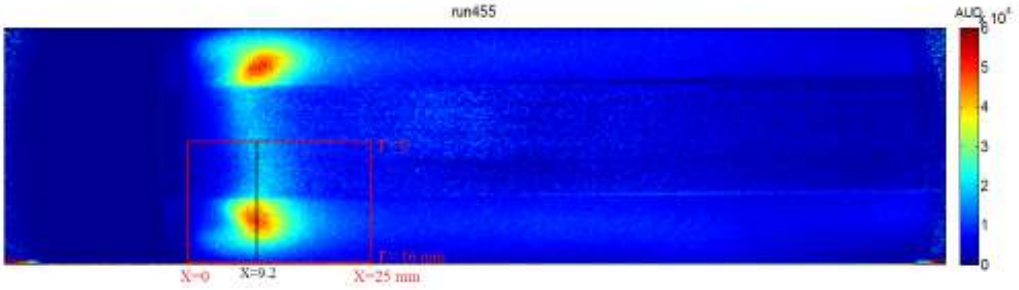


Figure 4.45: Counts from the ICCD image for run 455 showing OH* chemiluminescence. The rectangle in red indicates the region of interest for application of the Abel inversion processing. The data along the black line indicated at location of X=9.2 mm is extracted for a more detailed illustration of the Abel inversion analysis.

Measurements of chemically excited flame radicals are relatively easy to obtain, but it can be challenging to achieve reliable conversion to meaningful concentration information in the flame or combustion study. Rayleigh scattering as the calibration source has been utilized in the past decades in some optical arrangements in order to relate the measured signals to absolute physical quantities (Luque and Crosley, 1996; Walsh et al., 1998; Smith et al., 2002; Bohm et al., 2005).

The calibration method to compute the number density proposed here relates the measured OH* chemiluminescence to the emission from the hot graphite which is assumed a blackbody. The intensity ratio of OH* chemiluminescence and radiation of hot graphite recorded by the ICCD camera simultaneously during testing is used to determine the

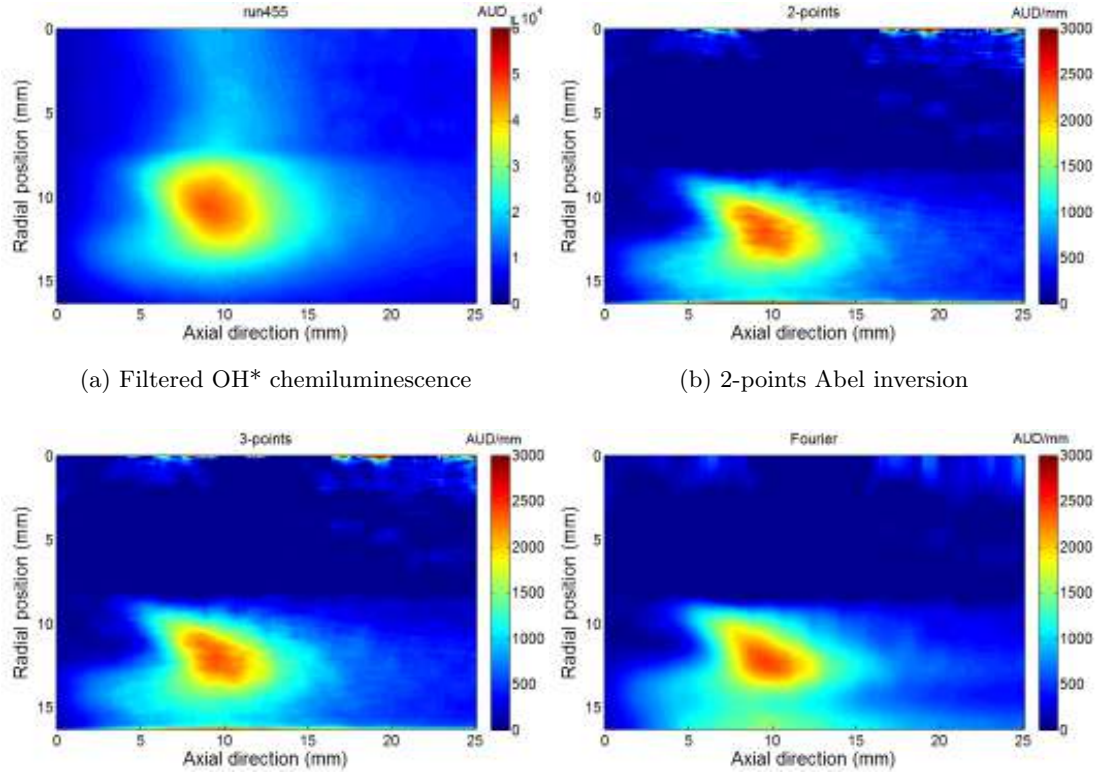


(a) Filtered OH* chemiluminescence

(b) 2-points Abel inversion

(c) 3-points Abel inversion

(d) Fourier-based Abel inversion

Figure 4.46: Image of OH* chemiluminescence signals in the region of interest and Abel-inverted data.

number density of the radiating radical OH*. The schematic illustration of the optical chemiluminescence detection system is depicted in Figure 4.44(b). Pixels that collect radiation from $\Delta A$ at the intersection of the graphite surface and the axis through its center are chosen as the calibration sources. $\Delta V$ represents an observed volume in the path of the line-in-sight integration for a pixel.

The ratio of signal intensity $S_g$ (units of ADU) and the Abel inverted OH* chemiluminescence $S_{OH^*}(Abel)$ (units of ADU/mm) can be related to the number ratio of photons collected by the optical system that are emitted from the hot graphite surface

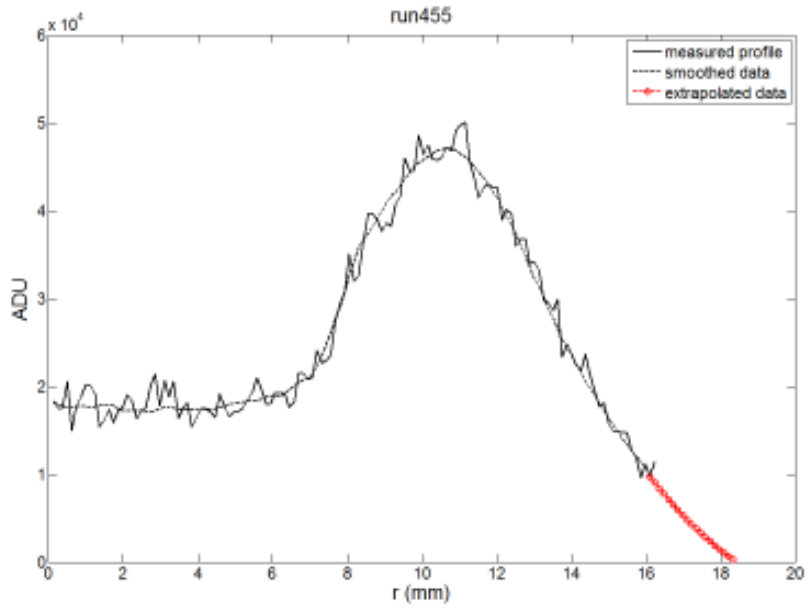


Figure 4.47: Extracted OH* chemiluminescence signals of pixels at X = 9.2 from the ICCD image.

($N_g$) and those emitted by excited-state OH* chemiluminescence ($N_{OH^*}$) within $\Delta V$.

$$\begin{aligned}
\frac{S_g}{S_{OH^*(Abel)}} &= \frac{N_g}{N_{OH^*}} \\
&= \frac{\int_{\lambda=290}^{330} \frac{I_{b\lambda}}{h\nu}\,\eta\,d\lambda\,\Omega_1\,\xi_1\,\varepsilon\,\Delta t}{\frac{[OH^*]_{em}}{4\pi}\,\eta_{(\lambda=308nm)}\,\Omega_2\,\xi_2\,\varepsilon\,\Delta t} \\
&= \frac{\int_{\lambda=290}^{330} \frac{E_{b\lambda}}{\pi\,h\nu}\,\eta\,d\lambda\,\Omega_1\,\xi_1\,\varepsilon\,\Delta t}{\frac{[OH^*]_{em}}{4\pi}\,\eta_{(\lambda=308nm)}\,\Omega_2\,\xi_2\,\varepsilon\,\Delta t}
\end{aligned} \tag{4.19}$$

where $I_{b\lambda}$ (W/(m$^2\,\mu$m sr)) and $E_{b\lambda}$ (W/(m$^2\mu$m)) are the monochromatic radiation intensity and emissive power from $\Delta A$ into surrounding hemisphere space in which $E_b = \pi I_b$ (Lambert's cosine law), $[OH^*]_{em}$ (N/m$^3 \cdot$ s) is the OH* number density in $\Delta V$ that emit photons into surrounding sphere space per second, $h\nu$ is the photon energy, $\eta$ is the Asahi bandpass filter transmission, $\Omega$ is the solid angle over which the light is collected, $\xi$ is the pixel efficiency in counts per photon, $\varepsilon$ is the efficiency of the

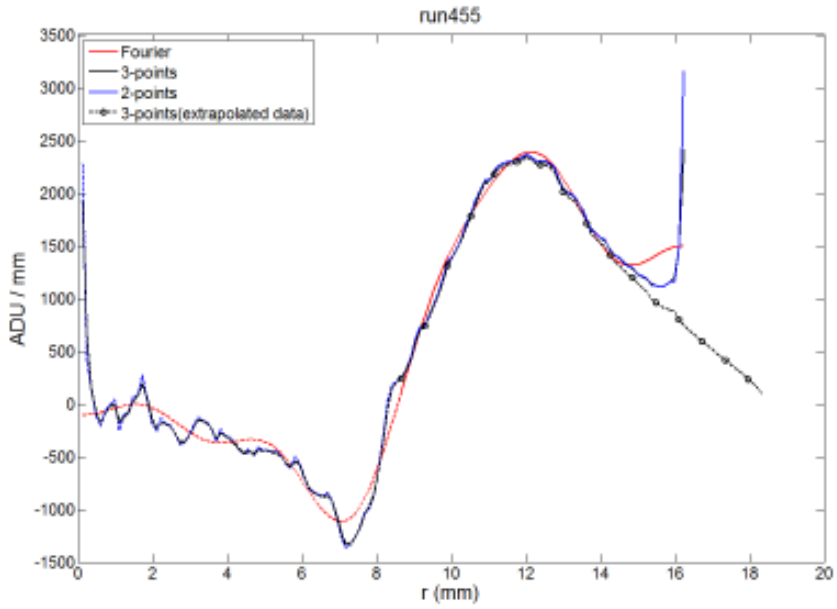


Figure 4.48: Comparison of the radial signal distributions via three Abel inversion methods.

collection optics which is treated as a constant within the bandpass range of the optical filter as discussed in Section 4.2.2, $\Delta t$ is the ICCD camera exposure time.

The difference of solid angles $\Omega_1$ and $\Omega_2$ can be neglected since the effective pixel size ($0.126 \times 0.126\,mm$) is very small when compared to the object distance (800 mm approximately). The relative sensitivity of the pixels is available as reported in Section 4.2.1. An assumption is made that a constant filter transmission at $\lambda = 308\,nm$ is applied to OH* emission spectra and this is a reasonable assumption because the spectrally resolved measurements of OH* chemiluminescence (Brieschenk et al., 2012) demonstrated that most of its emission occurs within the wavelength range of 306 nm and 310 nm. Thus the number density of excited-state OH* emitting radiation can be computed

$$[OH^*]_{em} = \frac{4\,S_{OH^*(Abel)}\,\xi_1}{S_g\,\eta_{(\lambda=308nm)}\,\xi_2} \int_{\lambda=290}^{330} \frac{E_{b\lambda}}{h\nu}\,\eta\,d\lambda \tag{4.20}$$

Figure 4.49 depicts the calculated results of OH* number density that emit photons based on three different Abel inversion methods according to Eq. 4.20. This absolute quantified results with combination of flow and boundary conditions described

previously has the potential to provide useful validation data for CFD combustion simulations.

The uncertainties in the OH* measurements using the technique proposed in this thesis arises from: (1) the uncertainty in the radiation from the calibrating light source (which is the hot graphite radiation in this case); (2) the Abel inversion method; and (3) the assumption of a constant transmission at $\lambda = 308\,nm$ for OH* emission through the ASAHI narrow-band-pass filter. The uncertainty of TCRP measurement was assessed to be $\pm\,5\%$ as discussed in Section 3.5. The uncertainties caused by the Abel inversion was evaluated to be $\pm\,2\%$ by Dasch (1992). The assumption of a constant transmission at the fixed wavelength was estimated to introduce uncertainties as high as $\pm\,30\%$. In addition to the above three effects, further uncertainties arise to due to the optical arrangement used in the present work: solid angle differences for different pixels, depth of field effects and finite field of view effects. The overall measurement uncertainty is estimated to be $\pm\,50\%$ based on the consideration of all of these affecting factors.

Note that for the most accurate application of the Abel inversion technique to ICCD imaging, the following points should be considered. 1. The depth of field should be considered when setting up the optic detection system. An optical configuration with a large depth of field is preferable in order to achieve approximately parallel rays for the line-of-sight collection. Having a large depth of field can also be of benefit in that it can reduce the blur on the ICCD due to collection of emission from parts of the flame that are not in the object plane. 2. The camera field of view should include the area of all radial object signals within the region of interest.

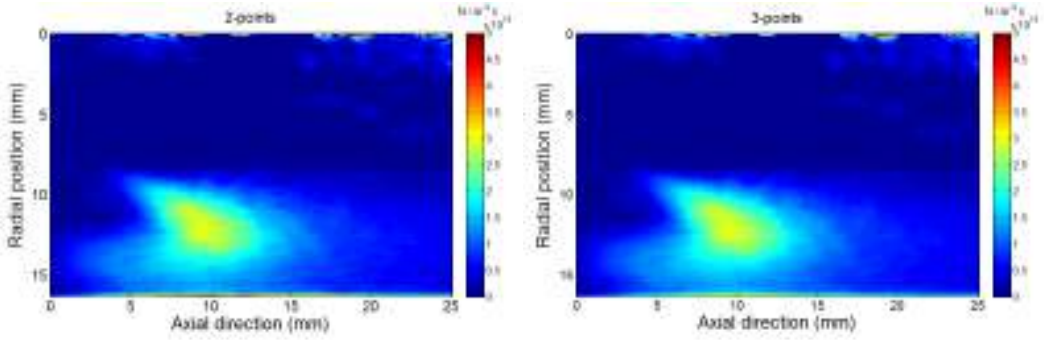


(a) 2-points (b) 3-points

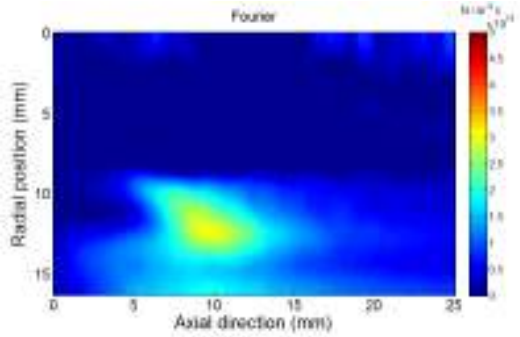


(c) Fourier

Figure 4.49: Number density of excited-state OH*.

# Chapter 5

# Computational Approach

The method of computational fluid dynamics (CFD) complements the experiments to provide insight into flow features such as the mixing process following fuel injection that are relatively hard to study experimentally. CFD also can provide an alternative method to ground-based hypersonic experiments and also flight tests, due to the lower implementation cost but simulations require validation in some manner. This chapter describes the numerical approach employed for the simulation of the heat-induced combustion experiments using the CFD suit, Eilmer3.

Initially, the CFD simulations were used to analyse the internal flow of the fuel delivery process in order to assist in the design and validation of the fueling system. Those simulation results were presented in Section 3.4. The combustion experiments were numerically analysed using the hydrogen oxidation kinetics scheme involving the OH* sub-scheme mechanism described in Section 2.4.

## 5.1 Flow Solver - Eilmer3

Eilmer3, developed at the University of Queensland (Jacobs et al., 2014), is a computational flow solver that is able to simulate transient compressible flows in two-dimensional geometries both planar and axisymmetric as well as three-dimensional geometries by solving the Navier-Stokes equations in multi-block structured grids. Eilmer3 is an ex-

plicit time-marching solver, hence simulating steady flows requires a relatively long time for initial transient effects to settle. Details of the numerical algorithm are provided in Jacobs et al. (2012).

The latest version of Wilcox's $k-\omega$ model (Wilcox et al., 1998) has been implemented by Eilmer3's developers, which is claimed to be significantly improved from the previous versions with advantages of less sensitivity to inflow turbulence conditions and improved simulation of supersonic separated flows.

### 5.1.1 Guidelines for using $k-\omega$ model in Eilmer3

The suitability of Wilcox's 2006 $k-\omega$ turbulence model used in Eilmer3 has been validated by Chan et al. (2012) against five test cases that have flowfields representative of those to be expected in scramjets. The simulated results demonstrated a generally good agreement to the experimental data. Chan et al. (2012) also recommended some guidelines for using Wilcox's $k-\omega$ model in Eilmer3.

1. Non-dimensionalised normal distance of first cell from the wall, $y^+$

The normal distance of the first cell from the wall is a critical factor that affects the CFD simulation accuracy of surface skin friction and heat flux predictions using RANS turbulence models (Wilcox et al., 1998). This distance is commonly expressed in its non-dimensionalised form $y^+$. It has been suggested that the value of $y^+$ should be less than 1, which implies at least one cell is within the viscous sublayer. Values of $y^+$ less than 0.3 are recommended for shock-separated hypersonic flows. The computational work reported in following context employed non-uniform grids with clustering toward the walls in order to satisfy the requirement for $y^+$ less than 0.3. Grid clustering was also used near the exit of the injector to capture the detailed flow structures typically associated with jets and supersonic cross flows.

2. Minimum number of cells within boundary layer

The thickness of the boundary layer is normally defined as the distance perpendicular to the wall where the flow velocity reaches 99 % of the free stream value. In order to

allow sufficient resolution of the profile across the boundary layer, a minimum number of cells between 10 and 20 is recommended. A larger number of cells, even up to 90 are recommended to resolve shock-separated boundary layers (Boyce and Hillier, 2000). For the present simulations, there are typically more than 30 cells within the boundary layer apart from regions such as the tip of the cone where the boundary layer starts with zero thickness.

3. Maximum aspect ratio of cells

It is commonly agreed that having high cell aspect ratios in CFD simulations can reduce the accuracy of CFD computation. Values of cell aspect ratio less than 600 are recommended for near-wall cells while values of cell aspect ratio less than 5 in non-boundary layer regions should be used. The maximum aspect ratio of cells was 4.5 for the present numerical simulation work.

4. Free stream turbulence properties  turbulence kinetic energy, $k$ and specific dissipation rate, $\omega$

Chan et al. (2012) has demonstrated that the free stream turbulence properties have an effect on simulated results using Wilcox's $k-\omega$ model in Eilmer3. Matching the free stream turbulence properties in the CFD in-flow boundary definition to the real nozzle flow was attempted in order to achieve a precise computation. Free stream quantities of $k$ and $\omega$ can be expressed

$$k = \frac{3}{2}\left(I_{turb}V_{\infty}\right)^2 \tag{5.1}$$

$$\omega = \rho\frac{k}{\mu_{lam}}\left(\frac{\mu_{lam}}{\mu_{turb}}\right) \tag{5.2}$$

where $I_{turb}$ refers to the turbulence intensity, and $\mu_{lam}/\mu_{turb}$ is the laminar-to-turbulent viscosity ratio (Wilcox et al., 1998). The values of 0.00001 for turbulence intensity in free flight and 0.1 for wind tunnel flow are quoted. Values from 0.00001 to 100 are recommended for the free stream laminar-to-turbulent viscosity ratio. The values of

$I_{turb}$ and $\omega$ are estimated from the relationships (Fluent, 2006)

$$I_{turb} = 0.16\,(Re_e)^{-\frac{1}{8}} \tag{5.3}$$

and

$$\omega = \frac{k^{0.5}}{C_{\mu}^{0.25}\,l} \tag{5.4}$$

where $Re_e$ is the Reynolds number at nozzle exit, $C = 0.09$ is an empirical constant specified in the turbulence model, $l$ is the turbulence length scale, a physical quantity related to the size of the large eddies that contain the energy in turbulent flows. An approximate relationship between the nozzle exit diameter $D$ and $l$ is given as $l = 0.07D$ for fully-developed duct flows.

The $k-\omega$ turbulence model is used for the current CFD simulations. According to a prior study using the $k-\omega$ turbulence model in Eilmer3 (Chan et al., 2012), grid-induced errors of less than 5% for simulated quantities such as skin friction coefficient, surface heat flux, pressures, temperatures and velocities can be obtained when the meshing satisfies the recommendations outlined above. The geometric properties of cells near non-slip walls and freestream turbulence properties of the present CFD simulation work conform to the recommendations, so grid-induced errors of less than 5% are anticipated for the present simulations.

### 5.1.2 Gas model selection

For elevated temperature air flows, the high-temperature effects on gas dynamics should be considered. The chemical reaction effects on high-temperature air is described in Figure 5.1. The thermally perfect gas model involving the excitation of vibrational energy, where the thermodynamic properties depend only on temperature, is selected for numerical simulation since the expected temperature is below 2500 K in the hydrogen-air reacting flow.

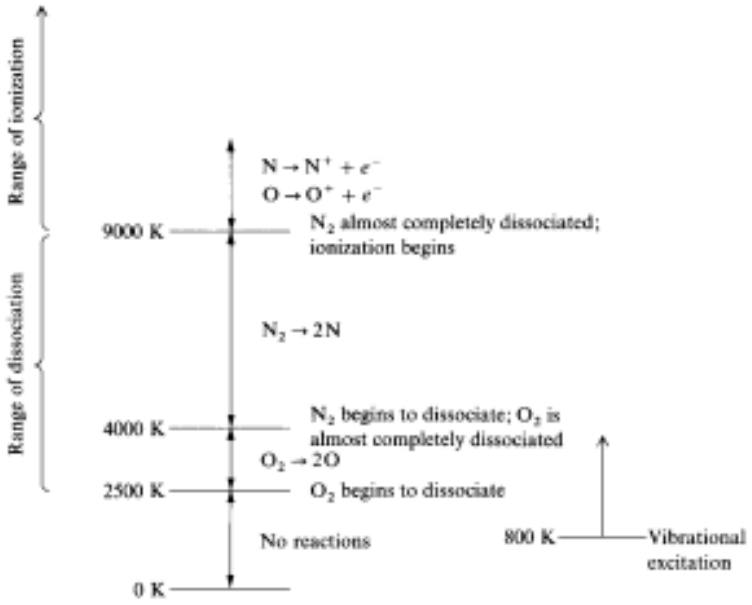


Figure 5.1: Ranges of vibrational excitation, dissociation, and ionization for air at 1 atm pressure (Anderson, 2000).

## 5.2 Static Combustion Simulations

The heat-induced combustion which occurred during the experiment for run 455 after the termination of Mach 4 nozzle flow was numerically reconstructed in a two-dimensional computational domain as shown in Figure 5.2, which represents the region above the axis of symmetry. The experimental results on the absolute number density of the radiating radical OH* from Section 4.2 are compared to the CFD simulated results in this section.

The wall temperature of the boundary representing the hot graphite surface and the cone extension surface is fitted by expression

$$\begin{aligned} T &= a_1 \cdot \frac{1 - exp(b_1 \cdot x + c_1)}{1 + exp(b_1 \cdot x + c_1)} + d_1 \qquad x < 0 \\ T &= a_2 \cdot exp\,(b_2 \cdot x) + c_2 \cdot exp\,(d_2 \cdot x) \qquad x \geq 0 \end{aligned} \tag{5.5}$$

where the fitting coefficients are

$$\begin{cases} a_1 = 550 \\ b_1 = -1.5 \times 10^3 \\ c_1 = -3.0 \\ d_1 = 1058 \end{cases} \qquad \begin{cases} a_2 = 1765 \\ b_2 = 1.299 \\ c_2 = -294.2 \\ d_2 = -255.9 \end{cases}$$

The fitted temperature distribution based on the experimental measurements is plotted in Figure 5.3. Note that the fitted results were extended upstream to cone surface. The fuel inlet boundary of the premixed hydrogen-air was specified according to experimental measurements. The boundary conditions for CFD simulation in Eilmer3 are listed in Table 5.1. The computational domain was divided into 196 sub-blocks each consisting of 400 structured mesh elements, which resulted in a total mesh count of 78400. The computational simulations were performed using the USQ High Performance Computing (HPC) facility.

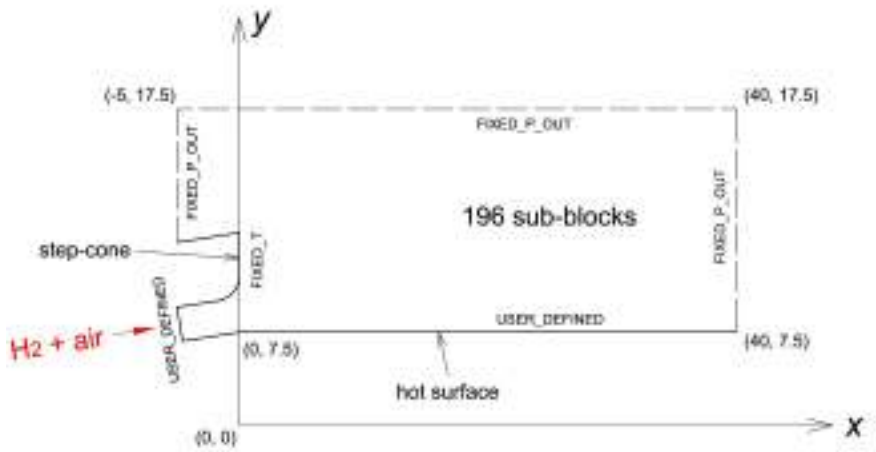


Figure 5.2: Computational domain and boundary conditions, the position of selected corners are given by (x, y) in mm.

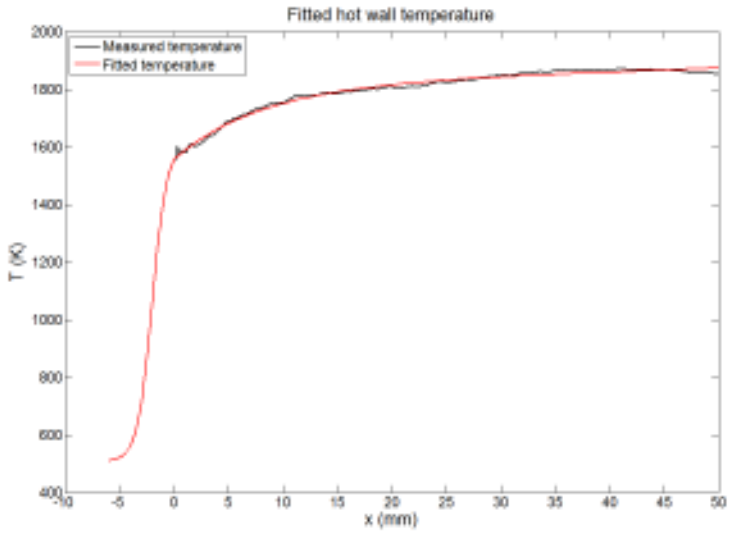


Figure 5.3: Fitted hot surface temperature distribution based on experimental measurement, x = 0 refers to the leading edge of the graphite tube.

Table 5.1: Boundary conditions specified in the static combustion simulation.

| **Fuel inlet** | **Outlet** | **Step-cone surface** | **Hot model surface** |
|---|---|---|---|
| Mass flux ($kg/s \cdot m^2$) | Fixed P (kPa) | Fixed T (K) | Fixed T (K) |
| 0.965 | 15 | 400 | UDF |

The simulation of the static heat-induced combustion resulted in strong turbulent characteristics as shown in Figure 5.4, which is an animation consisting of 150 transient results starting at a simulation time of 13 ms with an interval of 0.1 ms between frames. The exposure time of the optical combustion diagnostic is normally determined by the sensitivity of the detecting instrument, the intensity of the target signals and the signal-noise ratio (SNR). The complex LIF measurement techniques can capture the transient species status within the reacting flows with a time resolution as high as nanoseconds with the laser assisted excitation. The simplicity of the chemiluminescence optical set up makes it convenient to implement, but sensitivity is low so exposure times are relatively high. The time-averaged simulation results of the radical OH and the excited OH (OH*) were generated to compare with the experimental measurements, as shown in Figure 5.5.

OH radicals are known to be the key species in the development of hydrogen ignition and

these are often targeted as a flame location indicator in laser diagnostics methods. It is noticeable from Figure 5.5b that OH* is only generated in limited regions compared to the OH within the reaction zone. The phenomenon of populated OH* in the upstream front of reaction zone can be interpreted from the analysis of OH* mechanism presented in Section 2.2.2.

The formation of OH* in hydrogen mixtures through the three-body recombination reaction $H + O + M \rightleftharpoons OH^*$ follows the production of H and O atoms. The production of H atoms is mainly via the chain branching reactions $H_2$+O $\rightleftharpoons$ OH+H and $H_2$+OH $\rightleftharpoons$ $H_2O + H$, while the chain branching reaction $O_2 + H \rightleftharpoons OH + O$ is the major source of O atoms (Kathrotia et al., 2010). The depletion of OH* is dominated by the quenching reaction $OH^* + M \rightarrow OH + M$ with M = $H_2O$ and H.

In the present simulations, the distribution of O and H atoms concentrations which determine the OH* and OH production rates are consistent with that of the simulated results from a premixed stoichiometric hydrogen-air flame at 1 atm based on Mueller's model (Qiao, Kim and Faeth, 2005), as shown in Figure 5.6. The concentrations of O and H atoms decrease rapidly away from the combustion initiation locations, whereas OH remains at a consistently high level throughout the whole reaction zone. The same distribution trends of O, H and OH concentration can also be observed clearly from the present simulation results of the turbulent combustion in Figure 5.5.

The number density of emission-producing OH* is computed based on the simulation results and the rate coefficients of $1.45 \times 10^6$ for its decay reaction $OH^* \rightarrow OH + hv$. Absolute concentration comparison of numerical simulated and experimental measured radiating OH* is illustrated in Figure 5.7, where the numerical simulation results (top view) and experimental measurement (bottom view), which has been post-processed through the method described in Section 4.2.8 are overlapped on the ICCD image of test run 452. It can be observed that the shape of radiating OH* concentrations profiles is well predicted by the numerical simulations using the reaction mechanism described in Section 2.2.2. The calculated peak OH* concentration from the CFD simulation in the present work is 10 times higher than the measured value.

The OH* chemical mechanism is still controversial, especially for the OH* formation